Pumping and mixing of cerebrospinal fluid in the glymphatic system

by

Yiming Gan

Submitted in Partial Fulfillment of the

Requirements for the Degree

Doctor of Philosophy

Supervised by

Professor Douglas H. Kelley

Department of Mechanical Engineering

Arts, Sciences and Engineering

Edmund A. Hajim School of Engineering and Applied Sciences

University of Rochester

Rochester, New York

Contents

Bi	ograp	phical S	Sketch	V	İ
A	cknov	vledgm	ents	vii	i
A l	bstrac	et		X	i
C	ontrik	outors a	and funding source	xii	i
Li	st of	Tables		xvi	i
Li	st of]	Figures		xli	i
1	Intr	oductio	on	1	1
	1.1	Cereb	rospinal fluid and the glymphatic system	-	l
		1.1.1	Structure and pathways of the glymphatic system		l
		1.1.2	The flow of CSF is suppressed by wakefulness	2)
		1.1.3	The waste clearance cannot be explained by pure diffusion,		
			indicating a flow of ISF in the ECS	3	3
	1.2	A med	chanism for pumping cerebrospinal fluid: arterial pulsation .	۷	ļ
	1.3	The as	strocyte endfoot and the potential valve mechanism	ć	5

CONTENTS iii

2	The	hoop-stress model: A valve model based on the stretching and	
	shri	nking of the endfoot gap	11
	2.1	Background	11
	2.2	The hoop-stress model	14
		2.2.1 Description and formulation of the model	14
		2.2.2 Results	19
	2.3	The three-dimensional computational model	30
	2.4	Discussion	34
3	The	deformation and the flow resistance change of the slit-shape	
J		oot gaps under pressure oscillation	43
	3.1	Background	44
	3.2	The 2D shell model	48
	3.3	Results	51
		3.3.1 On the direction of the gap	52
		3.3.2 On the aspect ratio of the gap	54
		3.3.3 The 3D simulation	55
		3.3.4 Code validations and mesh convergence	56
	3.4	Discussion	59
4	A pe	erivascular pumping fluid-dynamic model with the valve mecha-	
	nisn	1	61
	4.1	Background	62
	12	The model	64

CONTENTS iv

	4.3	Result	s	69
		4.3.1	With the valve mechanism, cardiac pulsations drive a net	
			CSF influx	69
		4.3.2	The valve mechanism is suppressed during wakefulness	71
		4.3.3	A lumped-parameter model and the frequency analysis	74
		4.3.4	With the valve mechanism, functional hyperemia drives	
			a net CSF influx in addition to that produced by cardiac	
			pulsation	77
	4.4	Discus	ssion	80
5	Exp	erimen	tal measurements of functional hyperemia and cardiac	
	puls	ation, a	and their impacts on the CSF flow	91
	5.1	Backg	round	92
	5.2	Result	s	94
		5.2.1	Whisker stimulations induce functional hyperemia in mouse's	
			brain, causing an increased CSF influx	94
		5.2.2	Coupling between the CSF flow velocity and the vasomo-	
			tion induced by whisker stimulation	95
		5.2.3	Coupling between the PVS width and the vasomotion in-	
			duced by whisker stimulation	98
		5.2.4	Arterial diameter changes and not neural activation in-	
			creases CSF inflow	100
		5.2.5	Impedance pumping models reproduce flow characteristics	100

CONTENTS v

		5.2.6	Experimental measurements of penetrating artery motions	
			due to cardiac pulsations and functional hyperemia	104
	5.3	Discus	ssion	. 108
6	Disc	cussion	and future work	112
	6.1	Valve 2	Mechanism	113
	6.2	Valvel	ess pumping	115
		6.2.1	Peristaltic pumping	115
		6.2.2	Impedance Pumping	. 117
	6.3	The os	emotic force	. 119
	6.4	Model	ing advection and diffusion in the glymphatic network	120
		6.4.1	Estimating the amplitude of the pressure difference driven	
			by functional hyperemia	121
Bi	bliog	raphy		125
A	Mat	hemati	cal details of the perivascular pumping models	132
В	Imp	edance	pumping models	140

Biographical Sketch

The author was born in Taihe, a small town in Jiangxi Province, South China, and spent his happy childhood there. At the age of 9, he moved to Shunde, a more developed city in Guangdong province with his parents. His father teaches philosophy at a local university and his mother teaches politics at a high school. In 2015, the author attended the University of Science and Technology of China, where he developed his interest in fluid mechanics. He earned a Bachelor of Science degree in Modern Mechanics there in 2019. In the fall of 2019, the author came to the United States to pursue his Ph.D. in the Mechanical Engineering Program at the University of Rochester. In the spring of 2020, during the covid 19 pandemic, the author met his advisor, Professor Douglas H. Kelley, and joined the Mixing Lab as a Ph.D student. Served as the research assistant; he did multiple research projects on the cerebrospinal fluid and the glymphatic system, including experiments and computational modeling. He is fascinated by the driving mechanism of the cerebrospinal fluid and its great importance in curing brain deceases. Beside

researches, he has been learning classical guitar in Eastman Community School, University of Rochester, since 2020.

List of publications:

- 1. **Gan, Y.**, Thomas, J. H., & Kelley, D. H. (2024). Gaps in the wall of a perivascular space act as valves to produce a directed flow of cerebrospinal fluid: a hoop-stress model. Journal of the Royal Society Interface, 21(213), 20230659.
- 2. **Gan, Y.**, Holstein-Rønsbo, S., Nedergaard, M., Boster, K. A., Thomas, J. H., & Kelley, D. H. (2023). Perivascular pumping of cerebrospinal fluid in the brain with a valve mechanism. Journal of the Royal Society Interface, 20(206), 20230288.
- 3. Holstein-Rønsbo†, S., **Gan, Y.**†, Giannetto, M.J. et al. Glymphatic influx and clearance are accelerated by neurovascular coupling. Nat Neurosci 26, 1042–1053 (2023). https://doi.org/10.1038/s41593-023-01327-2
- 4. Kim, D., **Gan, Y.**, Nedergaard, M., Kelley, D. H., & Tithof, J. (2023). Image analysis techniques for in vivo quantification of cerebrospinal fluid flow. Experiments in Fluids, 64(11), 181.
- 5. Ladrón-de-Guevara, A., Mestre, H., **Gan, Y.**, Boster, K., Newbold, E., Hauglund, N., Sørensen, F., Song, W., Du T., Kelley, D.H., and Nedergaard., M. Arousal-induced vascular dynamics induces flow reversal of the glymphatic system. Submitted.

Acknowledgments

To start, I would like to thank my Ph.D. advisor, Professor Douglas Kelley for his continuous support throughout grad school life. Professor Kelley is an outstanding researcher, a responsible teacher, and a great individual. He helped me become an independent researcher with insightful advices and great patience. His passion in Science always inspires me to explore, and overcome challenges. More importantly, I learnt how to become a better person from him.

I want to thank all current and prior colleagues in the group: Bitong Wang, Yisen Guo, Ibrahim Mohammad, Jeff Tithof, Yasser, Vaezi, Ruy Ibanez, Aditya Raghunandan, Kimberly Boster, Kevin Wegner, Keelin Quirk, Jarod Forer, Nikola Raicevic, Helena Schreder, Jonathan Cheng, Jia Liu, Aditya Rajan, Jiatong Sun, Devin Wong, Fatima Min Rivas. It is my honor to work with these creative researchers. Aditya Raghunandan, Kimberly and Yisen, have offered me significant support as senior researchers. Though I've been overseas for years, the group makes me feel at home all the time.

ACKNOWLEDGMENTS ix

I would like to thank all my collaborators for their tremendous help. I would like to thank Professor John H. Thomas. He has been instrumental in helping me develop and complete multiple projects, showing great patience in reviewing, editing my writing, and contributing ideas. I want to thank the neuroscientists I collaborated with, including Stephanie Von Holstein-Rathlou, Antonio Ladron, Professor Ting Du, Professor Lauren Hablitz, and Professor Maiken Nedergaard. Their expertise in the field, which I am not that familiar with, makes the research output much more impactful.

I want to thank Professor Douglas Kelley, Professor Kimberly Boster, Professor Jessica Shang and Professor Lauren Hablitz for being my committee members and providing important suggestions for my research projects. My sincere appreciation also goes to my committee chair, Professor Marvin Doyley, for generously agreeing to chair my defense.

I also want to thank the current and former staff in the ME office for their assistance. Jill Morris, Cody Phillips, Kaleb Chitaphong, and Sarah Ansini have made the atmosphere in the department delightful and diverse. You have always been there when I had problems.

I want to thank my friends in Rochester: Yu Zhang, Yu Feng, Yuzhou Lu, Ziyang Ye, Yuxuan Liu, Zhaopu Xu, Yiwen E, Manfred Virgil Ambat, Kristen Churnetski, Michael Lavell and Esosa Agbongiator. I want to thank my guitar teacher Anthony Lalena and Lynn Mcgrath, and my band members: Jin Dou, Ruoyang Hu, Yihan Liu, and Xiaofei Zhou. I want to thank my gym buddies and my basketball buddies. I want to thank my old friends in China: Guande Wu,

ACKNOWLEDGMENTS x

Yucheng Zhang, Ziqing Mai, and Yigong Qin. I want to thank my undergraduate professors in the University of Science and Technology of China: Professor Dejun Sun, Professor Zhenhua Wan, and Professor Changgan Zeng. I would like to extend my sincere thanks to Yaqing Jin, Longnan Li, Professor Leonardo Chamorro, and Professor Nenad Miljkovic for their support and guidance during my summer internship at the University of Illinois Urbana-Champaign.

In the last, I want to thank my parents and my grandparents. I want to thank my cousin sister, Jingran Xiao, my uncles Zengnian Xiao and Zuomin Xiao. I want to thank my girl friend, Yongyi Cai, for supporting me through the journey. Your love and supports send away my loneliness, giving me the courage to keep moving forward.

Abstract

The flow of cerebrospinal fluid (CSF) along perivascular spaces (PVSs) and interstitial fluid (ISF) in the extracellular spaces (ECS) is an important part of the brain's metabolic waste clearance system. The brain-wide circulation of these fluids is often called the glymphatic system. Experiments reveal that arterial motions from cardiac pulsations and functional hyperemia (neurovascular coupling) drive CSF in the same direction, on average, as the blood flow, but since no valve has been found in the PVS, the mechanism ensuring this direction is unclear.

Astrocyte endfeet bound the PVSs of penetrating arteries, separating them from brain ECS. Gaps between astrocyte endfeet may provide a pathway for fluid transport across the wall. Recent studies suggest that the astrocyte endfeet may function as valves that rectify the CSF flow, producing the net flow observed in experiments.

In this thesis, we show that the valve mechanism can exist based on simple features of the PVSs. Oscillatory pressure in the PVS causes expansion and

ABSTRACT xii

shrinking of the outer wall and the gaps on it. As CSF passes through the gaps from the PVS into the surrounding interstitium, this expansion and shrinking act as a rectifying valve because the fluid flows more easily when the gaps are larger. We provide analytical and numerical models that verify and quantify the mechanism.

We couple the endfoot valve mechanism with fluid dynamics simulations of the CSF flow in the PVS and find an axial net flow of CSF in the PVS that is coupled with the net flow across the endfoot gaps due to the mass conservation law, which matches the experiments. We find that cardiac pulsations drive a net CSF flow consistent with prior experimental observations. Functional hyperemia, acting with cardiac pulsation, increases the net flow. We also find, in agreement with experiments, a reduced net flow during wakefulness due to the known decrease in ECS permeability compared to the sleep state.

We present experimental work that reveals the importance of functional hyperemia in accelerating the CSF flow. We measured the diameter change waveform of functional hyperemia in the pial artery and the CSF flow velocity in the surrounding PVS, revealing a direct coupling between them. We present in vivo imaging of penetrating arteries in mice, which we use to measure the amplitude of the diameter change.

Contributors and funding source

This work was supervised by a dissertation committee consisting of Professor Douglas H. Kelley (advisor) of the Department of Mechanical Engineering, Professor Jessica Shang of the Department of Mechanical Engineering, Professor Kimberly Boster of the Department of Mechanical Engineering, Professor Lauren M. Hablitz of the Department of Neurology, and Marvin Doyley (chair) from the Department of Electrical and Computer Engineering.

Financial support for this thesis was received from the U.S. Army under award no. MURI W911NF1910280, the U.S. National Center for Complementary and Integrative Health under award no. R01AT012312, and the BRAIN Initiative of the U.S. National Institutes of Health under award no. U19NS128613.

Chapter 2 is based on "Gaps in the wall of a perivascular space act as valves to produce a directed flow of cerebrospinal fluid: a hoop-stress model" which was printed in the Journal of the Royal Society Interface and has been modified to fit in this thesis (Gan, John H Thomas, and Douglas H Kelley 2024). The thesis author

is the primary author and was responsible for deriving and simplfying equations of the hoop stress model, writing the MATLAB code to demonstrate the results, running three-dimensional fluid-solid interaction simulations and writing the paper. The thesis author prepared all the figures except figure 2.2, which was prepared by co-author Prof. Douglas Kelley. Co-author Prof. Douglas Kelley came up with the idea of the hoop stress model, provided guidance on deriving the equations, on figure formation, and edited the paper. Co-author Prof. John Thomas came up with the idea of adding the sleep/wake analysis to the hoop-stress model and edited the paper. Conversations with Prof. Hesam Askari offered valuable insights.

Chapter 3 is based on unpublished work aiming to study how the aspect ratio and the orientation of the endfoot gap affect the potential valve action. The thesis author is the primary contributor to this unpublished work. Prof. Douglas Kelley, Prof. Kimberly Boster and Prof. John Thomas provided help in completing the project.

Chapter 4 is based on "Perivascular pumping of cerebrospinal fluid in the brain with a valve mechanism" which was printed in the Journal of the Royal Society Interface and has been modified to fit in this thesis (Gan, Holstein-Rønsbo, et al. 2023). The thesis author is the primary author and was responsible for developing the theoretical ideas, carrying out the simulations, analyzing the experimental data, and writing the manuscript. Coauthor Prof. Douglas Kelley came up with the idea of the lumped parameter model and edited the paper. Coauthor Prof. John Thomas came up with the idea of coupling the pressure response in the extracellular space into the model and edited the paper. Coauthor Dr. Stephanie Holstein-Rønsbo

and coauthor Prof. Maiken Nedergaard carried out the experiments and edited the paper. Coauthors Prof. Kimberly Boster developed the image processing tool to analyze the experimental data. The experimental part of the paper is presented in Chapter 5. Prof. Francesco Romanò shared the numerical solver for the CSF flow.

Chapter 5 is based on "Glymphatic influx and clearance are accelerated by neurovascular coupling", which was published in Nature Neuroscience (Holstein-Rønsbo et al. 2023), and some materials from "Perivascular pumping of cerebrospinal fluid in the brain with a valve mechanism", which was printed in the Journal of the Royal Society Interface (Gan, Holstein-Rønsbo, et al. 2023). Both have been modified to fit in this thesis. The thesis author was the second prime author of Holstein-Rønsbo et al. 2023. The thesis author analyzed data from the particle tracking experiments and other two-photon imaging experiments, carried out numerical simulations of the impedance pumping model and edited the paper. Coauthors Dr. Stephanie Holstein-Rønsbo and Prof. Maiken Nedergaard conceived of the study and wrote the manuscript. Stephanie Holstein-Rønsbo planned and carried out the experiments, analyzed and interpreted data. Coauthor Douglas Kelley analyzed data, developed the idea of the impedance pumping model and edited the paper. Coauthors Michael Giannetto, Martin Kaag Rasmussen and Verena Untiet planned and executed experiments. Coauthor Felix Ralf Michael Beinlich planned experiments and analyzed data. Coauthor Lauren Hablitz analyzed data. Coauthor Björn Sigurdsson and coauthor Laura Rose developed analyses and analyzed data. The thesis author was the prime author of Gan, Holstein-Rønsbo, et al. 2023. Coauthor Dr. Stephanie Holstein-Rønsbo and coauthor Prof. Maiken Nedergaard carried out the experiments and edited the paper. Coauthors Prof. Kimberly Boster developed the image processing tool to analyze the experimental data.

List of Tables

2.1	Parameter values of the hoop-stress model	20
2.2	Derived quantities of the hoop-stress model	21
4.1	Dimensional Parameters of the perivascular pumping model	69
A 1	Dimensionless Parameters of the perivascular numping model	136

List of Figures

1.1	The anatomy of cerebrospinal and interstitial fluid circulation (the
	glymphatic system) in the central nervous system. Panel adapted
	from Douglas H. Kelley and John H. Thomas 2023, copyright 2023
	the authors. Large chambers, such as the ventricles and subarach-
	noid space, are contiguous with small chambers that penetrate brain
	tissue, such as perivascular spaces, allowing for global circulation
	and solute transport.

LIST OF FIGURES xix

3

LIST OF FIGURES xx

1.3	The arterial pulsation waveform of the cardiac pulsation and func-	
	tional hyperemia, measured from the penetrating arteries of mice.	
	Panel adapted from Gan, Holstein-Rønsbo, et al. 2023, copyright	
	2023 the authors. (a) The arterial pulsation waveform of the car-	
	diac pulsation, which has a typical time scale of $\sim 0.3\ s,$ and a	
	pulsation amplitude of $\sim 2\%$. (b) The arterial pulsation waveform	
	of functional hyperemia (neuralvascular-coupling), which has a	
	typical time scale of ~ 10 s, and a pulsation amplitude of $\sim 10\%.$	
	Whisker stimulations were applied at $t = 30$ s to induced functional	
	hyperemia. The measurement was performed below the cortical	
	surface (at 0 $\mu m)$ and 100 μm deeper. The waveform includes a fast	
	dilation and a slow constriction (relaxation from the dilated state).	5
1.4	Astrocyte endfeet form the outer boundary the PVSs of penetrating	
	arteries. Panel adapted from M. X. Wang et al. 2021, copyright	
	2021 the authors. The astrocyte endfeet separate the PVSs of the	
	penetrating arteries from the ECS. Gaps between endfeet allow	
	fluid communications between the CSF in the PVS and the ISF in	
	the ECS	7

LIST OF FIGURES xxi

2.1 Asymmetry may make endfoot gaps function as valves that favour inwards over outwards fluid flow. Panel adapted from Bork et al. 2023, copyright 2023 the authors (a) An astrocyte (green) near an artery will extend processes with endfeet to form the outer boundary of the periarterial space (PVS) around the artery. (b) The endfoot bends only little under reasonable pressure differences. (b(i)) When the surrounding ECS pressure is greater than the pressure in the PVS, fluid will be driven out into the PVS and endfeet will be pushed together towards closing. (b(ii)) When pressures are equal, there will be no bending and no flow. (b(iii)) When the PVS pressure exceeds the ECS pressure, fluid will be driven into tissue in the ECS and endfeet will be pushed together towards opening. . 13 2.2 (a) A perivascular space lies between an arteriole and the tiled endfeet that form its outer wall, which we idealize as a cylinder of length L. (b) Pressure in the perivascular space causes the wall radius to expand from r_0 to r, the width of the gaps between endfeet to grow from g_0 to g, and the wall thickness to change from T_0 to T. At equilibrium, forces due to stresses σ_{φ} and σ_{z} within the wall

must balance forces due to the pressure p on its inner surface. . . .

15

LIST OF FIGURES xxii

2.3	Modeled flow in response to an alternating pressure. With pressure	
	p alternating over time (a), the volume flow rate Q also alternates,	
	but with greater volume flow in the positive direction (from perivas-	
	cular space to extracellular space) than in reverse (b). The pumping	
	efficiency η increases linearly with increasing characteristic strain	
	ε_0 (c)	21
2.4	Modeled flow in response to a sinusoidal pressure variation. With	
	pressure p varying sinusoidally with time (a), the volume flow rate	
	Q also varies, but with greater volume flow in the positive direction	
	(from perivascular space to extracellular space) than in the reverse	
	direction (b). The pumping efficiency η increases monotonically	
	with increasing characteristic strain ε_0 (c)	22
2.5	Modeled flow in response to an asymmetric pressure variation.	
	With brief, high positive pressure followed by longer-lived, gentler	
	negative pressure (a) , the volume flow rate Q also varies, but with	
	greater volume flow in the positive direction (from perivascular	
	space to extracellular space) than in the reverse direction (b). The	
	pumping efficiency η increases monotonically with increasing	
	characteristic strain ε_0 . (c)	24

LIST OF FIGURES xxiii

2.6 (a) Modeled flow in response to a sinusoidal pressure variation, accounting for resistance in the extracellular space (R_{ecs0}). (**b**) Increasing R_{ecs0}/R_0 reduces the amount by which forward flow exceeds reverse flow. (c) Increasing R_{ecs0}/R_0 reduces the rate of increase of pumping efficiency with increasing characteristic strain. (d) For the case where $R_{ecs0}/R_0 = 0.1$ during sleep, the mean flow rate during wakefulness (the red dot, $R_{ecs0}/R_0 = 0.5$) is 75% of the mean flow rate during sleep (the blue dot). In the regime $R_{ecs0}/R_0 < 1$, increasing R_{ecs0}/R_0 decreases the normalized mean volume flow rate. (e) For the case where $R_{ecs0}/R_0 = 1$ during sleep, the mean flow rate during wakefulness (the red diamond, $R_{ecs0}/R_0 = 5$) is 39% of the mean flow rate during sleep (the blue diamond). In the regime $R_{ecs0}/R_0 \ge 1$, increasing R_{ecs0}/R_0 decreases the normalized mean volume flow rate. (f) For both regimes, $R_{ecs0}/R_0 < 1$ and $R_{ecs0}/R_0 \ge 1$, the pumping efficiency decreases monotonically with increasing R_{ecs0}/R_0 . The pumping efficiency is smaller during wakefulness than during sleep for the cases considered in panels d and e (the dots and the diamonds).

28

LIST OF FIGURES xxiv

2.7 (a) Axial view of the numerical model of a segment of the perivascular space. The solid endfoot wall is immersed in the fluid domain, separating the outer extracellular space (ECS, radius 25 μm) from the inner perivascular space (PVS, radius 15 µm). The axial length of the tube is 30 µm. (b), Lateral view of the numerical model. The blue wire frame shows part of the internal mesh for the fluid domain. The endfoot gaps are modeled as two square holes (width 2 µm) on the endfoot wall surface. The thickness of the endfoot wall is 2 μm. (c) A positive pressure boundary condition (p = 100 Pa) applied to both end of the PVS causes a dilation of the endfoot wall and the gaps in it. (d) A negative pressure boundary condition (p = -100 Pa) applied to both ends of the PVS causes a constriction of the endfoot wall and the gaps in it. (e) Strain varies similarly with pressure in simulations and in the analytical hoop-stress prediction. (f) Pumping efficiency varies similarly with strain in the simulations and in the analytical hoop-stress prediction. (g) For the slit-shaped gaps, positive pressure (p = 100 Pa) causes nonuniform deformation and more expansion of the gaps compared to the square gaps in panel c. (h) For the slit-shaped gaps, negative pressure (p = -100 Pa) causes more shrinkage of the gaps compared to the square gaps in panel d. (i) Strain varies similarly with pressure in simulations and in the analytical hoop-stress prediction. We observed higher pumping efficiency in the slit-shaped gaps compared to the square gaps, indicating the stronger rectification due to the extra, uneven deformation. Simulations with pressure amplitudes of p_0 =[1,10,100] Pa are plotted. LIST OF FIGURES xxv

2.8	(a) The constriction of a slit-shaped gap (1 μ m \times 3 μ m), aligned
	with the PVS axis, when negative pressure ($p = -100 \mathrm{Pa}$) is applied
	to both ends of the PVS. (b) The constriction of a slit-shaped gap
	(3 $\mu m \times 1 \ \mu m$), perpendicular to the PVS axis, when negative
	pressure ($p = -100 \text{ Pa}$) is applied to both ends of the PVS. An axial
	slit constricts and deforms more. In each case, the lower image is
	an enlargement of the upper image. (c) Strain varies similarly with
	pressure in simulations and in the analytical hoop-stress prediction,
	and agreement is closer for slits perpendicular to the PVS axis.
	Simulations with pressure amplitudes of p_0 =[1,10,100] Pa are
	plotted

LIST OF FIGURES xxvi

3.1	The stress boundary conditions for the endfoot tissues (on four
	edges of the square shell) around the elliptical gap, oriented with
	its long axis along the axial direction of the PVS (z-direction).
	(a) When the pressure in the PVS is positive, the axial stress and
	the azimuthal stress far away from the gaps stretch the endfoot
	tissue and the gap in both directions. The black curve at the center
	represents the original gap shape. The blue curve represents the
	stretched gap. (b) When the pressure in the PVS is negative, the
	axial stress and the azimuthal stress far away from the gaps constrict
	the endfoot tissue and the gap. The black curve at the center
	represents the original gap shape. The blue curve represents the
	constricted gap shape

LIST OF FIGURES xxvii

 LIST OF FIGURES xxviii

3.3 The relative flow resistance change between a stretched gap and a constricted gap across different gap directions. The amplitude of the positive and negative pressure in the PVS is 100 Pa. (a) For a gap direction of $\beta = \pi/3$, deformation of the stretched gap and the constricted gaps is less dramatic compared to the lateral gap in figure 3.2a. (b) The relative flow resistance change and area change across different angles between the lateral axial stress and the direction of the gap (β in the range of $[0 \pi/2]$). Both decrease as beta increases, showing that the flow resistance and the area change are maximum when the $\beta = 0$ (the lateral gap), and they are minimum are $\beta = \pi/2$, the perpendicular gap. (c) The pumping efficiency across different angles between the lateral axial stress and the direction of the gap. The dashed line represents the case of ideal rectification, where the constricted gap resists any backflow 53 LIST OF FIGURES xxix

3.4 The relative flow resistance change ratio and area change between a stretched gap and a constricted gap across different aspect ratios. The amplitude of the positive and negative pressure in the PVS is 100 Pa. (a) For a gap aspect ratio of nearly 1 (essentially a circular gap), deformation of the stretched gap and the constricted gaps is less dramatic compared to the more elliptical gap in figure 3.2a. (b) The relative flow resistance change across different aspect ratios of the gap (l/t), where t is the length of the short axis of the gap, 1 is the length of the long axis of the gap (l/t), where t is the length of the short axis of the gap. The dashed line represents the ideal rectification, where the constricted gap prevents any backflow from reentering the PVS.

LIST OF FIGURES XXX

3.5 Direct 3D simulations that validate the 2D shell model. (a) The setup of the 3D simulations includes a cylindrical shell, which represents the endfoot wall, with an elliptical gap (F2) on it, where stress-free conditions apply. One end of the shell is clamped and open (F1), while the other end is free and closed to simulate the capillary end (F3). Positive pressure or negative pressure is uniformly applied to the inner surface of the shell to model the pressure oscillation in the PVS. The amplitude of the positive and negative pressure is 100 Pa (b) The mesh used for the finite element analysis of the endfoot wall is shown, with a denser distribution of mesh points around the gap. c With a positive pressure of 100 Pa applied in the PVS, the stretched gap shape is calculated using the 2D analytical shell model and the 3D FEM simulations using a larger and a smaller gap. The smaller gap configuration has an area four times smaller than the larger gap. With the area of the gap at rest state (p = 0) normalized to unity, the stretched shapes derived from these methods are plotted. (d) The relative area change across different gap directions β is presented and compared between the 2D analytical shell model and the 3D FEM simulations using larger and smaller gaps. The smaller gap configuration has an area four times smaller than the larger gap for the same value of β . (e) The relative flow resistance change across different gap directions is presented and compared between the 2D analytical shell model and the 3D simulations. **f** The pumping efficiency across different gap directions is presented and compared between the 2D analytical shell model and the 3D simulations. The dashed line represents the case of ideal rectification, where the constricted gap prevents any backflow from reentering the PVS. (g) The relative area change

LIST OF FIGURES xxxi

3.6 Validation of the analytical solution and mesh convergence. (a) A numerical 2D finite element analysis is performed to validate the analytical solution of the 2D shell model. The mesh used for the numerical analysis is shown, with an elliptical gap at the center of a square shell. With stress applied on one edge of the shell (σ_z , σ_{ω}), a zero normal displacement boundary condition is applied on the opposite edges ($u_z = 0$, $u_{\varphi} = 0$), so that the numerical model is stable equivalent to the 2D analytical shell model. To ensure that the stress is applied far away from the shell, the width of the square shell is set 50 times larger than the short axis of the gap. (b) The 2D numerical solution validates the 2D analytical solution for relative flow resistance and area changes across various gap aspect ratios. (c) With a positive pressure of 100 Pa applied in the PVS, the stretched gap shape is calculated using the 2D numerical model and the 2D analytical model. With the area of the gap at rest state (p = 0) normalized to unity, the stretched shapes derived from these methods are plotted. (d) A mesh convergence test is performed for the Strokes flow simulation by comparing the flow resistance of a stretched and constricted gap using different meshes. The mesh size is normalized to the width of the gap's short axis. (e,f) A mesh convergence test is performed for the 3D simulations by comparing the area and flow resistance of the stretched and constricted gap on the cylindrical endfoot shell using different meshes. The maximum mesh size (around the gap) is normalized to the width of the gap's short axis.

LIST OF FIGURES xxxii

 LIST OF FIGURES xxxiii

Flow and pressure driven by ten cycles of cardiac pulsation (f = 34.2 Hz). (a), As the artery dilates and constricts, the volume flow rate at the inlet of the penetrating perivascular space oscillates symmetrically around zero if no valve mechanism is implemented $(k_1/k_0 = 1)$, but favors inflow when the valve mechanism is active $(k_1/k_0 = 5)$. (b), Net volume of fluid pumped into the penetrating perivascular space, starting at the beginning of the fifth cycle to avoid transients. The volume fluctuates but increases, on average, at a rate depending on the permeability ratio k_1/k_0 . (c), Pressure fluctuations in the penetrating perivascular space, varying with endfoot wall elasticity $E_{\rm endft}$. In all cases, $k_1/k_0 = 5$. Softer walls deform more, reducing pressure fluctuations. (d), Mean fluid velocity in the perivascular space, over the last five cardiac cycles, shows net inflow. (e), The mean flow rate at the inlet increases with permeability ratio and wall elasticity. (f), The mean pressure gradient at the pial PVS inlet (over five cycles) likewise increases

70

LIST OF FIGURES xxxiv

4.3	Modeling sleep-wake differences by varying the permeability of
	the extracellular space (ECS). (a), The mean flow rate at the pial
	entrance increases with ECS permeability. (b), The maximum
	pressure in the perivascular space decreases ECS permeability.
	(c), Instantaneous ECS pressure and PVS velocity, during artery
	dilation by 5%, with ECS permeability $k_{\rm ecs} = 1 \times 10^{-16} \text{ m}^2$, corre-
	sponding to points marked with circles in a-b. (d), Instantaneous
	ECS pressure and PVS velocity, during artery dilation by 5%, with
	ECS permeability $k_{\rm ecs} = 2 \times 10^{-17} \text{ m}^2$, corresponding to points
	marked with squares in a-b. Greater permeability, as expected
	during sleep, leads to much lower pressure gradients in the ECS,
	even for stronger artery dilation 7'

LIST OF FIGURES XXXV

4.4

The lumped parameter model simplified from the fluid dynamic model and the frequency analysis. (a) Sketch of the lumpedparameter model. The volume change due to arterial pulsation is modeled as a flow source. Pathways to the pial PVS and the ECS each have a hydraulic resistance, and the endfoot wall is compliant. (b) In the absence of valve action, the fluid dynamical and lumpedparameter models predict similar pial PVS inflow rates in response to cardiac pulsations. (c) In the absence of valve action, the two models predict similar phase difference between wall velocity and q_{pial}. In panels c-d, simulation results are plotted as circles, and predictions from the lumped-parameter model are plotted as curves. In panels c-f, vertical dashed lines mark the characteristic frequencies $(R_{\rm eff}C_{\rm endft})^{-1}$. (d) In the absence of valve action, the two models predict similar maximum pressure p_{max} , which is proportional to fwhen f is small and approaches a constant value when f is large. (e) With valve action, the lumped parameter model (dots) and the fluid dynamical model (solid lines) predict that the mean flow rate varies with f in much the same way as p_{max} does in the absence of valve action. (f) With valve action, the lumped parameter model (dots) and the fluid dynamical model (solid lines) predict that the net inflow per cycle is maximum at low frequencies and decreases rapidly as f exceeds $(R_{\text{eff}}C_{\text{endft}})^{-1}$ LIST OF FIGURES xxxvi

4.5 Modeling valve action during functional hyperemia. (a), the arterial waveform that couples the cardiac pulsation and functional hyperemia. (b), We observed an increased net inflow volume over time for the coupled waveform compared to cardiac pulsation or functional hyperemia acting alone. (c), Comparison between the mean inflow rate driven by cardiac pulsation, functional hyperemia, the coupled waveform, and the superposition of the first two mean flow rates (d) The mean flow rate driven by the coupled waveform increases as with the dilation percentage, $h_{\rm fh}/r_1$, and the increase is more significant for $E_{\rm endft}=10^4$ Pa (e) The mean flow rate driven by functional hyperemia acting alone increases with $h_{\rm fh}/r_1$ (f) Asymmetric variation includes a quick dilation that greatly increases pressure.

78

LIST OF FIGURES xxxvii

5.1 Functional hyperemia increases neural activity, cerebral blood flow, and CSF tracer influx in the stimulated hemisphere (a) Adult wild-type mice were stimulated by whisker puffing (30 s each). (b) The whisker stimulations (5 Hz, 10 ms, which means a 5Hz stimulation protocol with 10 ms pulses (190 ms interval)) increase neural activity (marked by Ca²⁺) and cerebral blood flow (marked by hemodynamic signals (IOS)) in the stimulated hemisphere. (c) Representative image of tracer influx around the middle cerebral artery (MCA) (d) Fluorescence signal (MPI) of the tracer influx (n=10 mice). Gray bars show 30 s whisker stimulation. The intensity of the CSF tracers in the stimulated hemisphere increases faster than in the unstimulated hemisphere.

LIST OF FIGURES xxxviii

5.2	Partile tracking velocimetry (PTV) experiments reveal that func-	
	tional hyperemia causes changes in artery diameter and CSF ve-	
	locity. (a) Artery diameter changes were measured and averaged	
	across five lines spanning the artery lumen. The artery boundaries	
	were automatically registered based on fluorescence intensity (b)	
	Percentage artery diameter change (red) and vessel wall velocity	
	(brown) during functional hyperemia (n=7). (c) The time-averaged	
	velocity direction field (green arrows) shows net transport in the	
	downstream direction (d) Percentage change of downstream veloc-	
	ity (V_d) during functional hyperemia (n=7). (e) The time-averaged	
	velocity direction field (green arrows) shows the net transport in	
	the cross-stream direction. (f) Percentage change of cross-stream	
	velocity (V_c) during functional hyperemia (n=7)	97
5.3	Vasodilation cycles cause dynamical change in the width of perivas-	
	cular space (PVS). (a) CSF tracer (3 kDa dextran) was injected	
	into the cisterna magna to visualize the PVS before exposure to	
	unilateral whisker stimulation. Two-photon imaging was used to	
	map width changes of artery and perivascular space. The width	
	changes were averaged across five lines. (b) Kymograph of artery	
	and PVS during a 90 s protocol with 30 s stimulation. (c) Change	
	of arterial radius and perivascular space width during functional	
	hyperemia (n=6) (d), Movement of the outer PVS wall	99

LIST OF FIGURES XXXIX

5.4 Optogenetic stimulations on smooth muscle cells can cause changes in artery diameter (vasoconstriction cycle) in the brains of optogenetic mice without inducing neural activity. (a) Light stimulation increases intra-cellular Ca²⁺ in the smooth muscle cells causing depolarization and vasoconstriction. (b) Representative images of CSF tracer intensity during 30 min circulation. Optogenetic stimulations were given on one hemisphere (30 s stimulation periods with 60 s interval, following a 5Hz stimulation protocol with 10 ms pulses (190 ms interval)). The tracer accumulates faster in the stimulated hemisphere compared to the unstimulated, indicating a higher CSF inflow rate. (c) Representative images of CSF tracer influx during 30 min circulation. (d) Average CSF flow velocity of microspheres in response to optogenetic stimulation (n=5 mice). . 101

LIST OF FIGURES xl

5.5 Impedance pumping models reproduce characteristics of flows driven by functional hyperemia and optogenetic stimulation. (a) The first model is based on arterial dilation, which we experimentally induced by unilateral whisker stimulation. (b) In the first model, an arteriolar wall (red, shown in cross-section) actively dilates and relaxes in a small region (shaded red), with wall motion spreading in both directions along the artery, causing the flow of CSF (arrows) in the surrounding perivascular spaces. (c) Local wall motion across one dilatory cycle (enlargement of red shaded area in b). (d) The volume flow rate through one cross-section of the perivascular space (dashed line in b) varies over each dilation cycle. Flow is decreased during local dilation, with a slight lag, and increases during local relaxation. (e) Over many cycles, the flow carries passive tracers to the right along the perivascular space (enlargement of region marked in b). (f) The net flux (cumulative volume of fluid moving rightward through the cross-section shown in b) oscillates and increases steadily over time. Gray bars, whisker stimulations. (g) The second model is based on local vasoconstriction, which experimentally is obtained by optogenetic stimulation of mice expressing ChR2 in smooth muscle cells. (h,i) In our second model, the artery constricts instead of dilating, driving a flow with different spatial structures and different volume flow rates. (j-l), In the constriction model, as in the dilation model, tracer moves to the right and net flux increases over time. The direction of the tracer (to the right, not left) is determined by the location of the active arterial diameter change, not by whether it is dilation or LIST OF FIGURES xli

5.6 Measurements of cardiac pulsation and functional hyperemia in the penetrating arteries. (a) A penetrating artery of a mouse, from depths 0 μm to 100 μm, as imaged *in vivo*. (b) Artery diameter variation, measured from area changes. (c) Average normalized artery diameter variation in the cardiac frequency band, at depths $0 \mu m$ and $100 \mu m$, in N = 8 mice. Boxes show median and interquartile range. (d) Cross-section of a penetrating artery of a mouse. The shaded yellow mask represents the result of the segmentation algorithm. (e) Artery diameter variation, measured from area changes during functional hyperemia, averaged over N=7mice. (f) Average normalized artery diameter variation during cardiac pulsation, in N = 8 mice, and functional hyperemia, at depths $0 \mu m$ and $100 \mu m$, in N = 7 mice. Functional hyperemia causes greater diameter variations than cardiac pulsation ($p < 10^{-4}$ for an unpaired t-test), and with both mechanisms, there is a trend toward LIST OF FIGURES xlii

6.1	When rectified by ideal valves, asymmetric pressure waveforms
	with a longer duration of positive pressure (T ⁺), result in a higher
	pumping efficiency compared to the symmetric pressure waveform.
	T represents the period of the waveform. (a) A symmetric binary al-
	ternating pressure waveform and an asymmetric binary alternating
	pressure waveform normalized to the maximum pressure ampli-
	tude. In the asymmetric waveform, the positive pressure amplitude
	is smaller than the negative pressure amplitude to maintain a zero
	average pressure. (b) As T^+/T increases, the maximum pumping
	efficiency increases
6.2	Solute transport in the brain. Panel (a),(b) adapted from Holstein-
	Rønsbo et al. 2023, copyright the authors. Panel (c) adapted from
	Jeffrey Tithof et al. 2022, copyright the authors. CSF tracers in-
	jected into the mouse brain (a) are transported in the glymphatic
	network by a combination of advection and diffusion (b). (c) The
	CSF flow of the glymphatic network, including PVSs with bifurca-
	tions and the parenchyma has been modeled numerically (K. A. S.
	Boster et al. 2022), based on which we are building a solver to
	model time-dependent solute transport. By setting a concentration
	value of 100 at the inlet pial artery's PVS and a concentration
	value of 0 at the outlets of the network, we calculate and present
	spatially-resolved tracer concentration at three instants (d) 121

1. Introduction

1.1 Cerebrospinal fluid and the glymphatic system

The flow of cerebrospinal fluid (CSF) and interstitial fluid (ISF) in the brain is important for the removal of metabolic waste products, which are relevant to cognitive diseases, including Alzheimer's disease (Maiken Nedergaard and Goldman 2020). The circulation of CSF and ISF in the brain is called the glymphatic system (figure 1.1,Douglas H. Kelley and John H. Thomas 2023).

1.1.1 Structure and pathways of the glymphatic system

During sleep, the rapid inflow of CSF enters the brain through the perivascular spaces (PVSs) surrounding the pial arteries Mestre, J. Tithof, et al. 2018. It permeates deeper brain tissues through the PVSs of the penetrating arteries. The outer boundary of the PVSs of the penetrating arteries is formed by astrocyte endfeet, also decorated densely by aquaporin-4 (AQP4), a type of water channel

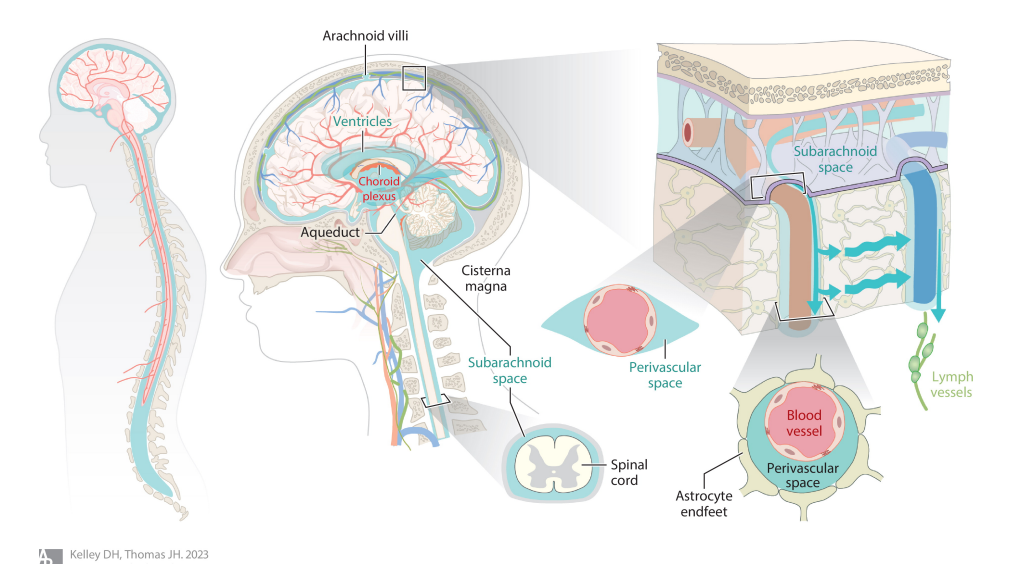


Figure 1.1: The anatomy of cerebrospinal and interstitial fluid circulation (the glymphatic system) in the central nervous system. Panel adapted from Douglas H. Kelley and John H. Thomas 2023, copyright 2023 the authors. Large chambers, such as the ventricles and subarachnoid space, are contiguous with small chambers that penetrate brain tissue, such as perivascular spaces, allowing for global circulation and solute transport.

protein. Gaps between endfeet allow flow exchange between the CSF in the PVSs and the ISF in the extracellular space (ECS), where metabolic wastes produced by the neural cells are cleared through the diffusion and speculated advection (see subsection 1.1.3), and collected to the efflux pathway of the glymphatic system (the perivenous spaces and the lymphatic vessels).

1.1.2 The flow of CSF is suppressed by wakefulness

As mentioned, the circulation of CSF/ISF happens predominantly during sleep and anesthesia. Xie et al. 2013 showed that during sleep/anesthetic states, the inflow of CSF tracer increased significantly, compared to wakefulness. Consequently, the clearance rate of metabolic waste is also higher during sleep compared to wakefulness. The study also showed that, during sleep, the brain ECS volume

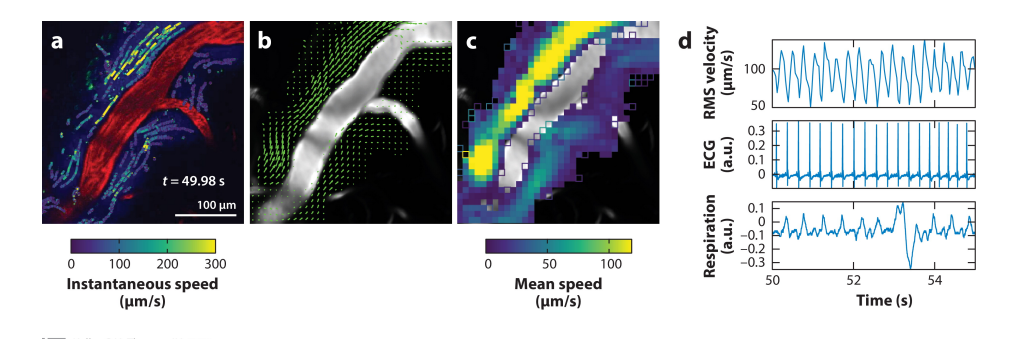


Figure 1.2: CSF flows in the surface perivascular space in the same direction as the blood, as measured from in-vivo particle tracking experiments. Panel adapted from Douglas H. Kelley and John H. Thomas 2023, copyright 2023 the authors. **(a)** Micron-scale fluorescent tracer particles (green) injected at the back of the skull are swept along by flowing cerebrospinal fluid (CSF) (blue) and pass through the perivascular space surrounding a surface artery (red). Particle-tracking measurements of tracer particles' positions and velocities make it possible to overlay pathlines colored according to the instantaneous velocity of each. **(b,c)** The time-averaged measurements show a mean flow field, which has the same direction as the blood flow. **(d)** The instantaneous root-mean-square CSF velocity pulses in synchrony with the cardiac cycle and shows little correlation with the respiratory cycle.

(porosity) increased by 60%, which leads to increased permeability in the ECS by a factor of 5 compared to wakefulness. The increased ECS volume during sleep provides a lower resistance pathway for the CSF/ISF circulation, which explains why the rapid flow of CSF is only observed in sleep or sleep-like state. The glymphatic flow reveals the importance of sleep in brain waste clearance, providing new insights into the function of sleep.

1.1.3 The waste clearance cannot be explained by pure diffusion, indicating a flow of ISF in the ECS

There are debates about the existence of the flow of ISF in the extracellular space (ECS). Unlike the CSF flow in the PVSs of the pial arteries, which has been observed and measured using particle tracking velocimetry in many studies, the flow in the ECS and the flow in the PVSs of the penetrating arteries are hard to

visualize and measure directly because of technical difficulties. For non-diffusive particles, the particle size is too large to follow the flow along those spaces. On the other hand, multiple studies have demonstrated that smaller, diffusive tracers do spread and propagate along those spaces, but people debate whether it is caused by the combination of advection and diffusion, or diffusion alone. Previously, the removal of metabolic waste was attributed solely to diffusion. However, both experimental evidence and theoretical analysis showed that the clearance would be much slower if there were only diffusion in the extracellular space. Computational modeling by V. Vinje et al. 2020 also showed a better fit to MRI tracer data when such a flow is included than when it is not (pure diffusion). There is also a theoretical argument for ISF flow in the ECS based on the observed wake/sleep variation in solute clearance. The clearance rate is faster during sleep (Xie et al. 2013), but with increased ECS volume during sleep, the clearance efficiency due to only diffusion would slightly decrease while the clearance due to advection would increase significantly (since the flow resistance decreases). These evidences suggest that there exists a flow of ISF in the ECS which plays an important role in clearing metabolic waste.

1.2 A mechanism for pumping cerebrospinal fluid: arterial pulsation

Experiments reveal that CSF in surface pial arterial PVSs flows in the same direction as the blood flows, pulsing at the cardiac frequency, but the driving mechanism

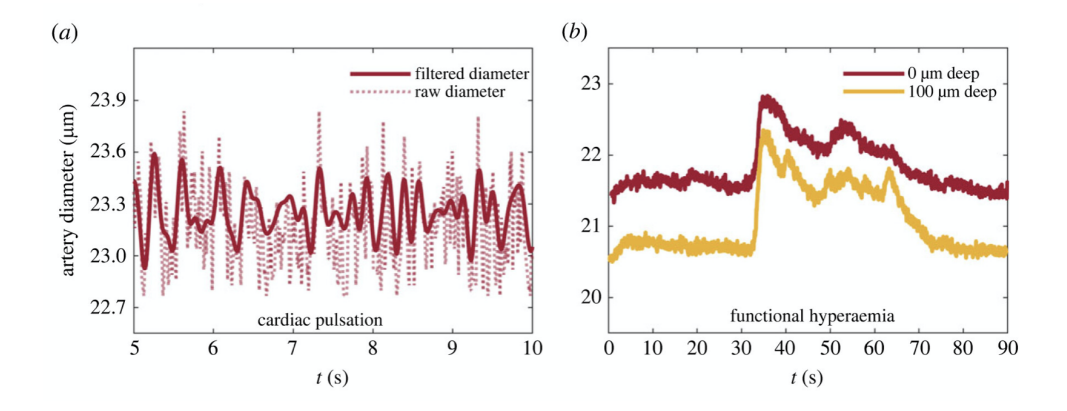


Figure 1.3: The arterial pulsation waveform of the cardiac pulsation and functional hyperemia, measured from the penetrating arteries of mice. Panel adapted from Gan, Holstein-Rønsbo, et al. 2023, copyright 2023 the authors. (a) The arterial pulsation waveform of the cardiac pulsation, which has a typical time scale of ~ 0.3 s, and a pulsation amplitude of $\sim 2\%$. (b) The arterial pulsation waveform of functional hyperemia (neuralvascular-coupling), which has a typical time scale of ~ 10 s, and a pulsation amplitude of $\sim 10\%$. Whisker stimulations were applied at t=30 s to induced functional hyperemia. The measurement was performed below the cortical surface (at 0 μ m) and 100 μ m deeper. The waveform includes a fast dilation and a slow constriction (relaxation from the dilated state).

is unknown (Bedussi et al. 2017; Mestre, J. Tithof, et al. 2018; Raghunandan et al. 2018). The pulsatile, directional flow has been attributed to *peristaltic pumping* by arterial cardiac pulsations (Hadaczek et al. 2006), in which the peristalsis drives the net flow in the same direction as the pulsation wave on the artery wall (P. Wang and Olbricht 2011; Carr et al. 2021). However, the wavelength of the cardiac arterial pulsations is ~ 1 m (for mice), much greater than the length of any PVS segment in a mouse's brain (~ 1 mm, Jeffrey Tithof et al. 2022). In such a sub-wavelength domain, the peristaltic pumping mechanism alone likely does not drive CSF flow at the speeds observed in experiments, ~ 20 µm/s in pial PVSs of mice (R. T. Kedarasetti, Drew P., and Costanzo 2020; Daversin-Catty et al. 2020).

Functional hyperemia (neurovascular coupling), the increase of blood flow due

to neural activity in the brain, has also been shown to accelerate CSF flow (Veluw et al. 2020; Holstein-Rønsbo et al. 2023). Functional hyperemia is associated with artery dilations of longer time scale and larger amplitude (figure 1.3a, \sim 10 s, \sim 10%) compared to cardiac pulsations (figure 1.3b, \sim 0.3 s, \sim 2%). How functional hyperemia promotes CSF inflow is not well understood, either. R. T. Kedarasetti, Drew, and Costanzo 2022 considered a poroelastic model that couples the axial flow along the PVS of a penetrating cortical artery and a radial flow between the PVS and the ECS. Their model suggests that functional hyperemia with a temporally asymmetric waveform of arterial pulsation can drive a net radial flow from the PVS into the ECS.

1.3 The astrocyte endfoot and the potential valve mechanism

The presence of valves or valve-like structures could be a possible mechanism for producing the bulk flow of CSF. While no valves have been found inside the PVSs, the astrocyte endfeet, which form the outer boundary of the PVS of a penetrating artery, are a possible candidate. Several studies using tracers indicate that fluid exchange between PVSs and the ECS occurs mostly through the gaps between endfeet (figure 1.4, M. X. Wang et al. 2021; Bohr et al. 2022). Bork et al. 2023 has shown that if the endfoot gaps are slightly asymmetric, narrower at the interstitial side than at the perivascular side, then the oscillating pressure in the PVS causes endfoot deformation, and size/shape change of the gaps, which hence changes

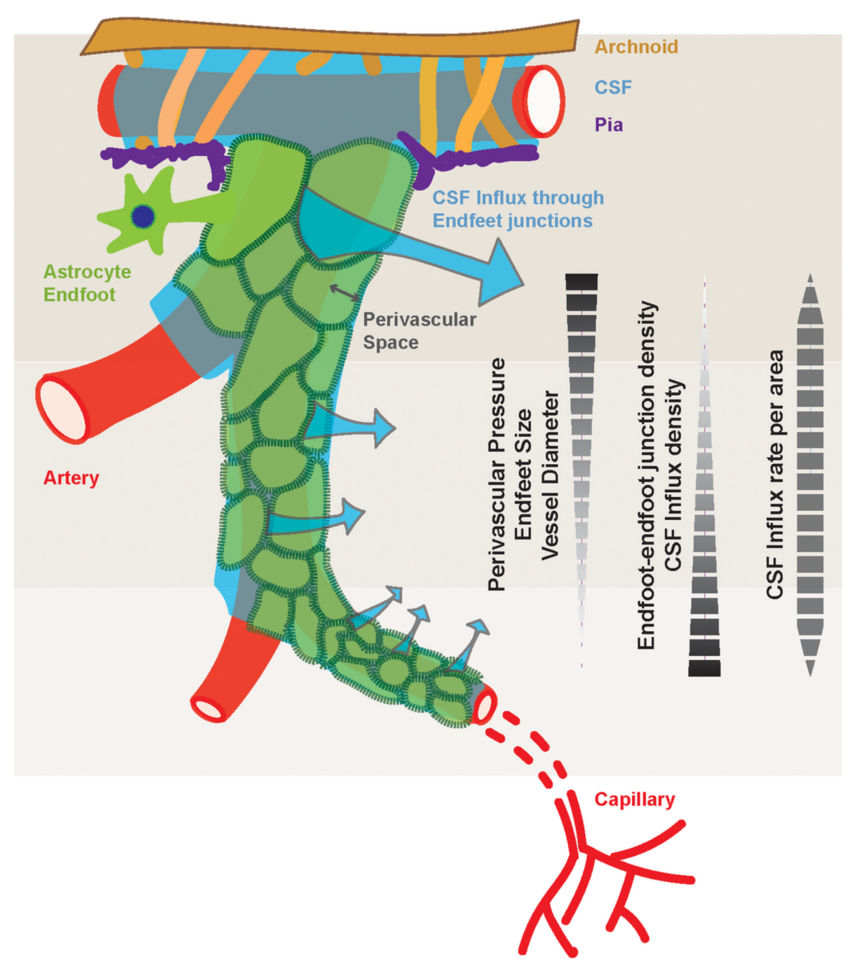


Figure 1.4: Astrocyte endfeet form the outer boundary the PVSs of penetrating arteries. Panel adapted from M. X. Wang et al. 2021, copyright 2021 the authors. The astrocyte endfeet separate the PVSs of the penetrating arteries from the ECS. Gaps between endfeet allow fluid communications between the CSF in the PVS and the ISF in the ECS.

the flow resistance. The flow resistance change of the gaps can rectify the flow and drive a bulk flow of CSF, similar to the action of a bicuspid valve. However, in vivo gap shape measurements are difficult. Determining whether the gaps are asymmetric requires ongoing work. Additionally, determining how the radial net flow across the endfoot gaps relates to the axial flow observed in the pial PVSs requires further studies.

In this thesis, we study the potential valve-like function of the astrocyte endfoot in the pumping mechanism of the glymphatic flow. In the first chapter, we show that an endfoot valve mechanism can exist even without a geometric asymmetry of the gaps. We consider the PVS as an axisymmetric, circular tube encircled by the endfoot wall, assumed to act as a linear elastic solid. Oscillatory pressure in the PVS causes expansion and shrinking of the outer wall. Increased pressure in the PVS causes the outer wall to expand, enlarging the gaps, while decreased pressure shrinks the gaps. As CSF passes through the gaps from the PVS into the surrounding interstitium, this expansion and shrinking acts as a rectifying valve because the fluid flows more easily when the gaps are larger. We present an analytical hoop-stress model to estimate how much shrinking and expansion can be expected in realistic conditions and how effective the rectification would be without any prescribed asymmetry of the gaps. We include the flow resistance change of the ECS to model the sleep/wake state, and find the flow suppressed by wakefulness, which is consistent with previous experiments (Xie et al. 2013).

In the second chapter, we present work regarding the hoop-stress model. When performing full three-dimensional fluid-solid interaction simulations to corroborate the hoop-stress analytical model, we find good agreement when the endfoot gap shape is square. However, the long slit (the rectangular shape with an extreme aspect ratio) is the more realistic shape of endfoot gaps. Choosing extreme aspect ratios of the gap to match the realistic geometry for the 3D simulation introduces extra, uneven deformation and results in much better rectification, which cannot be explained by the hoop-stress model alone. Hence, we develop a more complex ana-

lytical model to describe the extra deformation and quantify the extra rectification due to the realistic endfoot geometry.

In the third chapter, we couple the endfoot valve mechanism with fluid dynamics simulations of CSF flow in the PVS and find a resulting axial net flow of CSF in the PVS that is coupled with the net flow across the endfoot gaps due to the mass conservation law, which matches the experiments. We find that cardiac pulsations drive a net CSF flow consistent with prior experimental observations. Functional hyperemia, acting together with cardiac pulsation, increases the net flow. During artery dilation, the PVS shrinks, requiring fluid to be expelled, and the increased permeability of the endfoot wall allows fluid to pass into the ECS. During artery constriction, the PVS expands, requiring fluid intake, and reduced permeability of the endfoot wall inhibits a reflux of fluid from the ECS, so the fluid must come instead from the pial PVS connected to the penetrating PVS.

In the fourth chapter, we present experimental work that reveals the importance of functional hyperemia (neuro-vascular coupling) in driving the CSF flow. Using whisker stimulation to induce functional hyperemia in the mouse brain, we observed an increased influx of CSF tracer in the stimulated hemisphere through two-photon imaging. Using image processing tools and particle tracking velocimetry (Mestre, J. Tithof, et al. 2018), we simultaneously measured the diameter change waveform of functional hyperemia in the pial artery and the CSF flow velocity in the surrounding PVS, revealing a dynamical coupling between them. Furthermore, through optogenetic stimulation to induce vasoconstriction cycles, we find that vasomotion in the absence of neural activities increases CSF inflow,

which indicates that it is the vasomotion rather than the neural activities that drives the CSF inflow, in addition to the cardiac pulsation. Compared to the pial arteries, the diameter change of the penetrating arteries has not been well measured. We develop a robust segmentation tool to segment and measure the cross-sectional area of the penetrating arteries over time, based on which the diameter measurement is obtained. We measure the diameter change of both cardiac pulsation and functional hyperemia at various depths and find larger diameter change amplitudes in deeper cross-sections of penetrating arteries compared to those at the brain surface.

2. The hoop-stress model: A valve model based on the stretching and shrinking of the endfoot gap

In this chapter, we discuss a rectification mechanism based on the stretching and shrinkage of the endfoot gap. The results listed in this chapter have been published in Gan, John H Thomas, and Douglas H Kelley 2024. It has been reformatted and edited to fit within the thesis. The thesis author was the primary author on this work.

2.1 Background

Valveless pumping mechanisms, such as peristaltic pumping, cannot explain the CSF flow of the observed net flow rate by itself, which leads to the search of

potential valves. While no valve has been found inside the perivascular spaces, the astrocyte endfeet on the outer boundaries of PVSs may function as valves that rectify the flow and drive a bulk flow of CSF.

Endfoot gaps allow flow exchange between the CSF in the PVS and the ISF in the ECS. Endfeet deform as pressure oscillates, which may cause a shape and size change of the gaps, which therefore causes a flow resistance change, and a rectification. Bork et al. 2023 has shown that if the endfoot gaps are slightly asymmetric, narrower at the interstitial side than at the perivascular side (figure 2.1a), then the negative pressure in the PVS pushes the gaps towards closing (figure 2.1b(i)) compared to the relaxed state (figure 2.1b(ii)), and the positive pressure in the PVS pushes the gaps towards opening (figure 2.1b(iii)). These closing and opening actions act like valves that drive a net flow of CSF. Although it is hard to precisely measure shape of the endfoot gaps in vivo, the study indicated that models of brain fluid flow should explore the possibility that astrocyte endfoot gaps act as valves to convert an oscillatory flow into a directed flow.

In this chapter, we show that an endfoot valve mechanism can exist without assuming any geometric asymmetry of the gaps. We consider the PVS as an axisymmetric, circular tube encircled by the endfoot wall, assumed to act as a linear elastic solid. Oscillatory pressure in the PVS causes expansion and shrinking of the outer wall. Increased pressure in the PVS causes the outer wall to expand, enlarging the gaps, while decreased pressure shrinks the gaps. As CSF passes through the gaps from the PVS into the surrounding ECS, this expansion and shrinking acts as a rectifying valve because the fluid flows more easily when

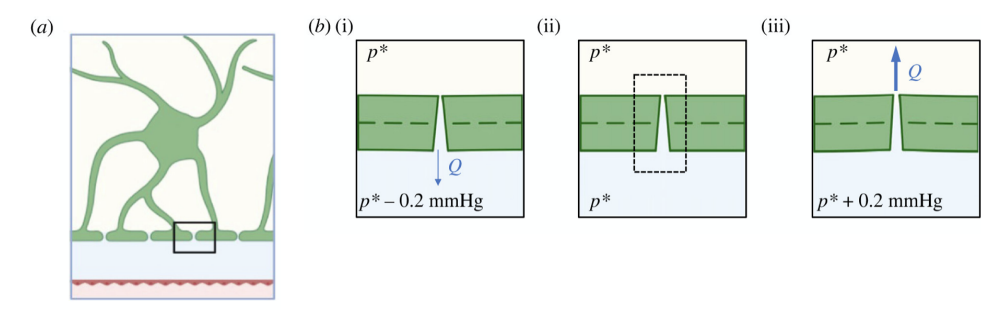


Figure 2.1: Asymmetry may make endfoot gaps function as valves that favour inwards over outwards fluid flow. Panel adapted from Bork et al. 2023, copyright 2023 the authors (a) An astrocyte (green) near an artery will extend processes with endfeet to form the outer boundary of the periarterial space (PVS) around the artery. (b) The endfoot bends only little under reasonable pressure differences. (b(i)) When the surrounding ECS pressure is greater than the pressure in the PVS, fluid will be driven out into the PVS and endfeet will be pushed together towards closing. (b(ii)) When pressures are equal, there will be no bending and no flow. (b(iii)) When the PVS pressure exceeds the ECS pressure, fluid will be driven into tissue in the ECS and endfeet will be pushed together towards opening.

the gaps are larger. We present an analytical hoop-stress model, using realistic estimates of parameter values to estimate how much expansion and shrinking can be expected, and how effective the rectification would be without any prescribed asymmetry of the gaps.

When we include the flow resistance of the ECS in the model, we find an increased net flow during sleep, in agreement with experiments (Xie et al. 2013; Holstein-Rønsbo et al. 2023), due to the known increase in porosity of the ECS (decreased flow resistance) compared to the awake state. We also perform full three-dimensional fluid-solid interaction simulations to corroborate the simpler hoop-stress model and to examine the role of gap geometry and gap direction.

2.2 The hoop-stress model

2.2.1 Description and formulation of the model

We model the PVS as a cylinder of relaxed radius r_0 and length L, as sketched in figure 2.2. The PVS outer wall is a cylindrical shell, composed of a linear elastic solid having Young's modulus E, Poisson ratio v, and thickness T. The pressure imposed upon the inner surface of the PVS wall by the CSF filling the PVS, measured with respect to the pressure in the surrounding ECS, is p. In the equilibrium case, the force due to pressure on the inside surface of the top half of the PVS must be balanced by the force due to azimuthal stress σ_{φ} in the PVS wall (figure 2.2b). Assuming the wall is thin ($T \ll r_0$), the stress is approximately uniform within the wall, so $2r_0pL = 2\sigma_{\varphi}TL$ and

$$\sigma_{\varphi} = \frac{pr_0}{T}.\tag{2.1}$$

Similarly, the pressure force on the right half of the PVS must be balanced by the axial stress σ_z in the PVS wall (figure 2.2c). Again using the thin-wall approximation leads to $p\pi r_0^2 = \sigma_z 2\pi r_0 T$ and

$$\sigma_z = \frac{pr_0}{2T}.\tag{2.2}$$

This expression is valid regardless of the shape of the ends of the PVS; in particular, they need not be flat. However, the right end is assumed to be closed, not open (to model the high resistance capillary side of the glymphatic pathway). Finally, the radial stress is $\sigma_r = p$.

Using Hooke's law, we can determine the azimuthal strain from the stress, which describes how much the PVS outer wall and its gaps expand and shrink

$$\varepsilon_{\varphi} = \frac{\sigma_{\varphi}}{E} - \frac{v}{E}(\sigma_{z} + \sigma_{r}) = \frac{p}{E} \left(\frac{r_{0}}{T} - \frac{vr_{0}}{2T} - v \right) \approx \frac{pr_{0}}{ET} \left(1 - \frac{v}{2} \right), \quad (2.3)$$

where the rightmost expression arises because $T \ll r_0$ (Roylance 2001). The radius of the PVS is

$$r = r_0(1 + \varepsilon_{\boldsymbol{\varphi}}). \tag{2.4}$$

As an elastic material (the endfoot tissue) expands and constricts, gaps in the material do the same. Assuming that the expansion and the constriction are the same for gaps as for tissue, a gap in the endfoot wall that is oriented in the axial direction has width

$$g = g_0(1 + \varepsilon_{\varphi}), \tag{2.5}$$

where g_0 is the gap width when p = 0.

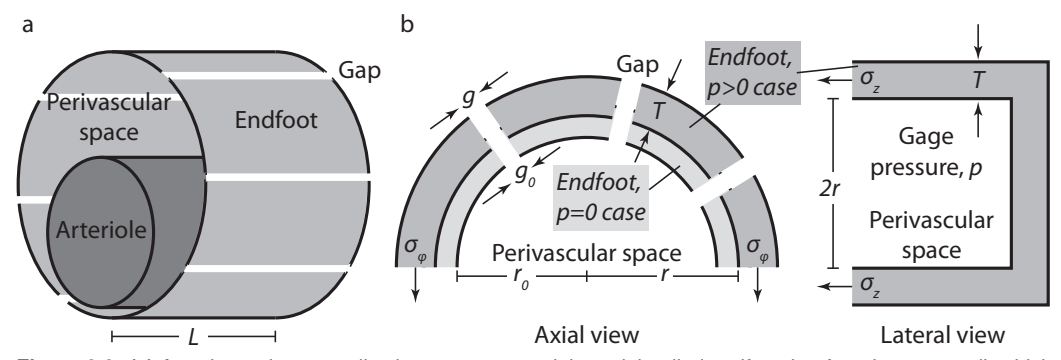


Figure 2.2: (a) A perivascular space lies between an arteriole and the tiled endfeet that form its outer wall, which we idealize as a cylinder of length L. (b) Pressure in the perivascular space causes the wall radius to expand from r_0 to r, the width of the gaps between endfeet to grow from g_0 to g_1 , and the wall thickness to change from g_1 to g_2 . At equilibrium, forces due to stresses g_2 and g_3 within the wall must balance forces due to the pressure g_2 on its inner surface.

Since the total volume of the endfoot wall is constant (for v = 0.5), we have

$$2\pi rTL = 2\pi r_0 T_0 L, \tag{2.6}$$

where T_0 is the thickness of the endfoot wall when p = 0. Combining Eqs. 2.4, 2.5, and 2.6, the thickness can be expressed as

$$T = T_0 \frac{g_0}{g},\tag{2.7}$$

Knowing how the gap size relates to the strain, and therefore the pressure, we can determine how the size of the gap affects the flow through it. The volumetric rate at which fluid passes through a wall gap from PVS to the ECS (parenchyma) is

$$Q = \frac{p}{R},\tag{2.8}$$

where *R* is the hydraulic resistance of the gap. Neglecting small effects at the ends of the gap, and entrance effects, the hydraulic resistance is that of fully developed Poiseuille flow between infinite parallel flat walls, given by White 2006; Jeffrey Tithof et al. 2022:

$$R = \frac{12\mu T}{g^3 L} = \left(\frac{g_0}{g}\right)^4 R_0,\tag{2.9}$$

where $R_0 = 12\mu T_0/g_0^3 L$ is the flow resistance when p = 0 and μ is the fluid viscosity. A quantity closely related to the hydraulic resistance and considered in prior studies is the wall permeability k, which is the inverse of the product of the

resistance and the surface area of the PVS wall:

$$k = \frac{1}{2\pi r_0 LR}.\tag{2.10}$$

Combining Eqs. 2.8, 2.9, 2.5, and 2.3 gives

$$Q(t) = \frac{p(t)}{R_0} \left[\frac{p(t) r_0}{ET} \left(1 - \frac{v}{2} \right) + 1 \right]^4, \tag{2.11}$$

where the dependence on time t has been written explicitly, for emphasis. We can rewrite equation 2.11 in terms of the strain,

$$Q(t) = Q_0 \varepsilon_{\varphi} \left(1 + \varepsilon_{\varphi} \right)^4, \tag{2.12}$$

where $Q_0 = ETR_0^{-1}r_0^{-1}(1-\frac{v}{2})^{-1}$ is a constant coefficient, or a characteristic flow rate. For small deformations, $\varepsilon_{\varphi} \ll 1$, we can simplify equation 2.12 by neglecting terms of third and higher order in ε_{φ} , giving

$$Q(t) = Q_0 \left(\varepsilon_{\varphi} + 4\varepsilon_{\varphi}^2 \right). \tag{2.13}$$

The first term in equation 2.13 is oscillatory, corresponding to a fluctuating flow of zero mean, and the second term is never negative, corresponding to a net flow. It is worth noting that to ensure the accuracy of equation 2.13, the amplitude of the azimuthal strain $|\varepsilon_{\varphi}|$ has to be small. In particular, when $\varepsilon_{\varphi} = -0.25$, Q(t) = 0, which means that the shrunk gap becomes an ideal valve, preventing

any backflow into the PVS. For $\varepsilon_{\varphi} < -0.25$, we will observe that the shrunk gap changes the original flow direction, which is not realistic, because the premise of small azimuthal strain magnitude is not satisfied.

Having determined how the flow resistance and flow rate depend on pressure, the final step is to determine how well this mechanism would produce net flow if driven by pressure variations that are purely oscillatory. A perfect rectifier, driven with a periodic and zero-mean pressure p(t), would eliminate all fluctuation and produce a steady flow. A more realistic rectifier produces a flow that has both a mean flow and a fluctuating component. For a pressure that fluctuates with fundamental frequency f, the mean flow is

$$\overline{Q} = f \int_{t_0}^{t_0 + f^{-1}} Q(t) dt,$$
 (2.14)

where t_0 is an arbitrary time. The amplitude of the fluctuating component can be defined as

$$Q' = \left(2f \int_{t_0}^{t_0 + f^{-1}} (Q(t) - \overline{Q})^2 dt\right)^{1/2}$$
(2.15)

by scaling the root-mean-square amplitude. Then, the effectiveness of rectification can be quantified with the *pumping efficiency* $\eta = \overline{Q}/Q'$, whose value is large when the net, directed flow is large compared to the fluctuations. (The inverse of η was described as a fluctuation ratio and considered in Ladrón-de-Guevara et al. 2022.)

All of the parameters in the model and their assumed numerical values are listed in Table 2.2.

2.2.2 Results

Binary alternating pressure

As a first example, consider an alternating PVS pressure that is positive and constant for the first half of each cycle and negative and constant for the second half:

$$p(t) = \begin{cases} p_0, & 0 \le t \le f^{-1}/2, \\ -p_0, & f^{-1}/2 \le t \le f^{-1}, \end{cases}$$
 (2.16)

where $p_0 > 0$ is a constant. The mean volume flow rate is

$$\overline{Q} = 4\frac{p_0}{R_0}\varepsilon_0 = 4Q_0\varepsilon_0^2, \tag{2.17}$$

where $\varepsilon_0 = p_0 r_0 (1 - v/2) E^{-1} T^{-1}$ is a characteristic strain. The amplitude of the fluctuating component is

$$Q' = \sqrt{2}Q_0\varepsilon_0,\tag{2.18}$$

and the pumping efficiency is

$$\eta = 2\sqrt{2}\varepsilon_0. \tag{2.19}$$

Now consider the parameter values listed in Table 2.1, which follow Jeffrey Tithof et al. 2022 and Gan, Holstein-Rønsbo, et al. 2023 and are believed to be reasonably realistic. With these parameter values, the pressure and volume flow rate vary over time as shown in figure 2.3a,b. The characteristic strain is $\varepsilon_0 = 0.15$. The pumping efficiency, which depends only on the strain (equation 2.19), is $\eta = 0.4$

Parameter	Value
Young's modulus E	* $[10^3 5 \times 10^4]$ Pa
Poisson's ratio <i>v</i>	0.5
pressure fluctuation amplitude p_0	133 Pa (1 mmHg)
PVS outer radius r_0	15 μm
PVS outer wall thickness T_0	*[0.5 µm 2 µm]
viscosity μ	$7 \times 10^{-4} \text{ Pa} \cdot \text{s}$
reference endfoot gap width g_0	20 nm
arteriole length L	1 mm

Table 2.1: Parameter values of the hoop-stress model.

(figure 2.3c). That is, this simple valve mechanism produces a mean volume flow rate about 40% as great as that of the fluctuating flow, when the applied pressure p(t) is purely an alternation.

The characteristic resistance is $R_0 = 2.10 \times 10^{18} \, \text{Pa} \cdot \text{s/m}^3$. With the alternating pressure, the endfoot gap width g alternates between 23 nm and 17 nm (we used $g_0 = 20 \, \text{nm}$), and the PVS radius r alternates between 17.3 μ m and 12.3 μ m (we used $r_0 = 15 \, \mu$ m, for the PVS radius change, we refer to figure 3c in Bojarskaite et al. 2023). The hydraulic resistance R therefore alternates between $8.4 \times 10^{17} \, \text{Pa} \cdot \text{s/m}^3$ and $3.35 \times 10^{18} \, \text{Pa} \cdot \text{s/m}^3$. The mean flow is $\overline{Q} = 3.79 \times 10^{-17} \, \text{m}^3/\text{s}$. The amplitude of the fluctuating component is $Q' = 8.96 \times 10^{-17} \, \text{m}^3/\text{s}$.

Some of these predictions can be compared directly to prior studies. In one study, neurons in the parenchyma, near the outer wall of a PVS surrounding a penetrating arteriole with diameter $\sim 10~\mu m$, were observed to move by $\sim 1.5~\mu m$ during functional hyperemia Ravi Teja Kedarasetti et al. 2020. Another study observed the PVS wall to move by $\sim 1~\mu m$, also during functional hyperemia Holstein-Rønsbo et al. 2023. A study of natural sleep-wake variation found the PVS wall moving

Derived quantities	Expression	Unit
azimuthal strain $arepsilon_{oldsymbol{\phi}}$	$pr_0(1-v/2)/ET$	
characteristic strain ε_0	$p_0 r_0 (1 - v/2) / ET$	
PVS outer radius <i>r</i>	$(1+\boldsymbol{\varepsilon_{\phi}})\mathbf{r}_{0}$	m
endfoot gap width g	$(1+\boldsymbol{\varepsilon_{\phi}})\mathbf{g}_{0}$	m
PVS outer wall thickness T	$T_0/(1+arepsilon_{oldsymbol{\phi}})$	m
reference flow resistance R_0	$12\mu T_0/g_0^3 L$	Pa/m ³ /s
flow resistance R	$R_0/(1+4arepsilon_{oldsymbol{arphi}})$	Pa/m ³ /s
permeability k	$1/2\pi r_0 LR$	m/Pa/s
flow rate $Q(t)$	p/R	m ³ /s
mean flow rate \overline{Q}	$\int_{t_0}^{t_0+f^{-1}} Q(t) dt$	m^3/s
fluctuating rate Q'	$(2f \int_{t_0}^{t_0+f^{-1}} (Q(t)-\overline{Q})^2 dt)^{1/2}$	m ³ /s
characteristic flow rate Q_0	$ET/R_0r_0(1-v/2)$	m ³ /s
pumping efficiency η	\overline{Q}/Q'	

Table 2.2: Derived quantities of the hoop-stress model.

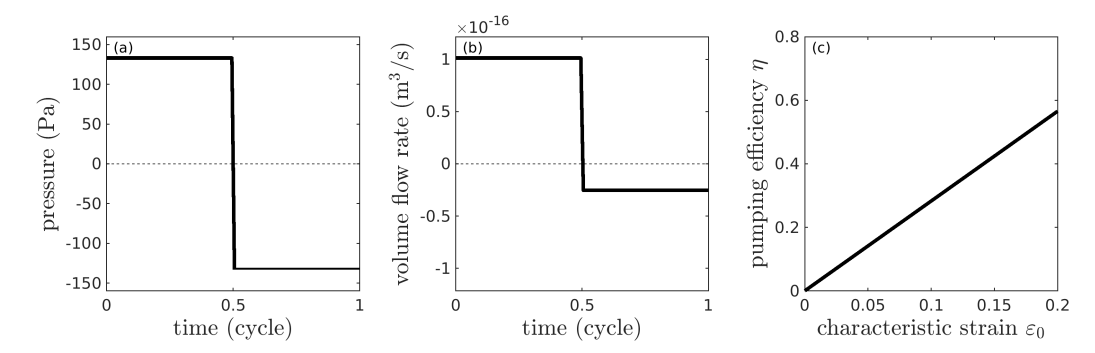


Figure 2.3: Modeled flow in response to an alternating pressure. With pressure p alternating over time (**a**), the volume flow rate Q also alternates, but with greater volume flow in the positive direction (from perivascular space to extracellular space) than in reverse (**b**). The pumping efficiency η increases linearly with increasing characteristic strain ε_0 (**c**).

 \sim 2 µm (Bojarskaite et al. 2023). The typical permeability of the PVS wall was estimated to be in the range 2×10^{-11} m/Pa/s to 3×10^{-10} m/Pa/s (Koch, Vegard Vinje, and Mardal 2023), based on geometrical factors known from prior electron microscopy (Mathiisen et al. 2010). The calculations above use quite different

reasoning but result in a similar value of 5.05×10^{-12} m/Pa/s using equation 2.10 (Our result is about four times smaller than their lower limit as we only consider a single gap). With the alternating pressure, the permeability k alternates between 3.72×10^{-12} Pa·s/m³ and 1.10×10^{-11} Pa·s/m³. Gan, Holstein-Rønsbo, et al. 2023, without elucidating a mechanism in greater detail, modeled pressure-dependent permeability fluctuations as a possible rectification mechanism, finding realistic flows when the permeability was chosen to vary by a factor of 2–5 through each alternation of pressure. The above example of alternating pressure results in permeability varying by a factor of 2.93, within that range. Experimental measurements find $\eta = 2$ (Ladrón-de-Guevara et al. 2022; Mestre, J. Tithof, et al. 2018), which implies rectification that is better than predicted in the above example $(\eta = 0.4)$ by a factor of five, suggesting that this mechanism could contribute but could not single-handedly achieve the observed rectification.

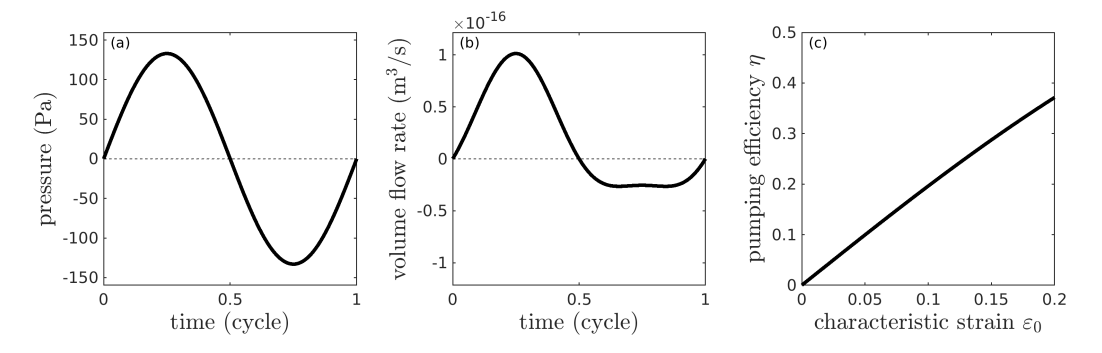


Figure 2.4: Modeled flow in response to a sinusoidal pressure variation. With pressure p varying sinusoidally with time (**a**), the volume flow rate Q also varies, but with greater volume flow in the positive direction (from perivascular space to extracellular space) than in the reverse direction (**b**). The pumping efficiency η increases monotonically with increasing characteristic strain ε_0 (**c**).

Sinusoidal alternating pressure

As a second example, we consider PVS pressure varying sinusoidally and having amplitude p_0 : $p(t) = p_0 \sin 2\pi f t$. The sinusoidal waveform better represents the pressure waveform driven by the cardiac pulsation. Using equation 2.11 leads to

$$Q(t) = Q_0 \left(4\varepsilon_0^2 \sin^2 2\pi f t + \varepsilon_0 \sin 2\pi f t \right), \tag{2.20}$$

The mean flow is

$$\overline{Q} = 2Q_0 \varepsilon_0^2. \tag{2.21}$$

The amplitude of the fluctuating component is

$$Q' = Q_0 \sqrt{\varepsilon_0^2 + 4\varepsilon_0^4} \,. \tag{2.22}$$

Now it becomes clear that the factor of 2 appearing in equation 2.15 ensures that Q' is the peak amplitude if p(t) varies sinusoidally. The pumping efficiency is

$$\eta = 1/\sqrt{1 + \frac{1}{4\varepsilon_0^2}}. (2.23)$$

Again using the parameter values listed in Table 2.1, the pressure and volume flow rate vary over time as shown in figure 2.4a,b. The characteristic resistance and strain remain unchanged. Accordingly, the gap size, PVS radius, resistance, and permeability each also vary with the same amplitude as in the previous example, but now sinusoidally. The mean flow is $\overline{Q} = 1.90 \times 10^{-17}$ m³/s. The amplitude

of the fluctuating component is $Q' = 6.62 \times 10^{-17}$ m³/s. The pumping efficiency is $\eta = 0.3$. In this case, then, the simple valve mechanism produces a mean flow about one-third as fast as the fluctuating flow, though the applied pressure p(t) is purely a fluctuation. Again, the predicted typical permeability and range of variation of permeability are similar to prior estimates, but the rectification is not as good as observed in vivo, suggesting this mechanism could contribute but others may be at play as well.

According to equation 2.23, for sinusoidally-varying pressure, as for alternating pressure, the pumping efficiency η depends only on the characteristic strain ε_0 . Its variation is shown in figure 2.4c and is similar to the alternating case.

Asymmetrically alternating pressure

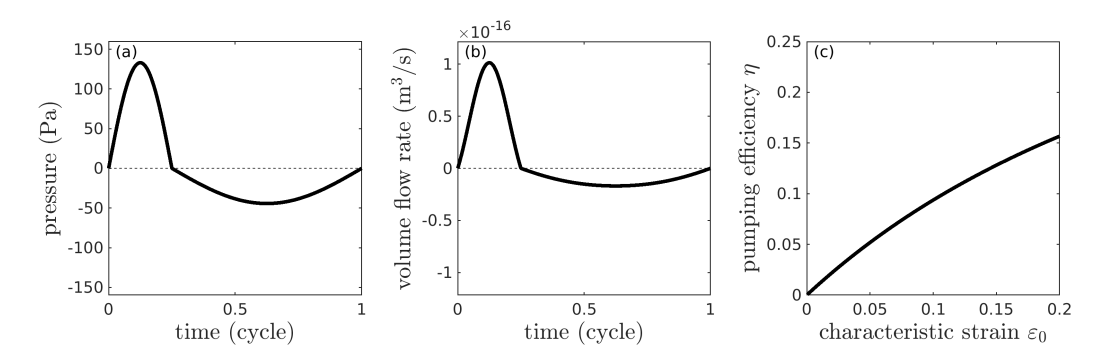


Figure 2.5: Modeled flow in response to an asymmetric pressure variation. With brief, high positive pressure followed by longer-lived, gentler negative pressure (a), the volume flow rate Q also varies, but with greater volume flow in the positive direction (from perivascular space to extracellular space) than in the reverse direction (b). The pumping efficiency η increases monotonically with increasing characteristic strain ε_0 . (c)

While a sinusoidally-varying pressure waveform can well represent the arterial pulsation driven by the cardiac cycle, it is not a robust model to describe the

waveform of functional hyperemia, which is asymmetric. Functional hyperemia, induced by neural activity, includes a fast arterial dilation and a slow artery constriction. Hence, as a third and final example, consider PVS pressure that varies asymmetrically in time, a characteristic that has been proposed to aid in rectification (Ravi Teja Kedarasetti et al. 2020). One simple asymmetric waveform, similar to one proposed previously by Gan, Holstein-Rønsbo, et al. 2023 is

$$p(t) = \begin{cases} p_0 \sin(4\pi f t), & 0 \le t < f^{-1}/4\\ \frac{p_0}{3} \sin\left(\frac{4}{3}\pi f (t - f^{-1})\right), & f^{-1}/4 \le t < f^{-1}. \end{cases}$$
 (2.24)

The volume flow rate is

$$Q(t) = \begin{cases} Q_0(\varepsilon_0 \sin(4\pi f t) + 4\varepsilon_0^2 \sin(4\pi f t)^2), & 0 \le t < f^{-1}/4 \\ Q_0(\frac{1}{3}\varepsilon_0 \sin(\frac{4}{3}\pi f (t - f^{-1})) + \frac{4}{9}\varepsilon_0^2 \sin(\frac{4}{3}\pi f (t - f^{-1}))^2), & f^{-1}/4 \le t < f^{-1} \end{cases}$$

$$(2.25)$$

The mean flow is

$$\overline{Q} = Q_0 \left(\frac{2}{3} \varepsilon_0^2 \right). \tag{2.26}$$

In this case, the fluctuating flow rate is in a more complicated analytical form. Here we show only the numerical solution. The amplitude of the fluctuating component and the pumping efficiency are calculated numerically figure 2.5. The pumping efficiency reaches 0.15 in the range of strains considered, putting it in the same order of magnitude as in the two earlier examples, though a bit less. At least with the mechanism considered here, this asymmetric pressure profile does not produce

superior rectification.

Flow resistance in the extracellular space and wake/sleep variations

If fluid passes from the PVS to the ECS through valve-like endfoot gaps, then the pumping efficiency of the system will depend, in part, on the hydraulic resistance of the ECS. An oscillatory pressure variation will also drive a pressure response in the ECS. To model these phenomena, we consider the case in which the ECS has a nonzero but constant resistance and the pressure is allowed to vary across the ECS but held constant at the outer boundary (which models the PVS of the nearest vein). Equation 2.8 is then replaced by

$$Q = \frac{p}{R + R_{ecc0}},\tag{2.27}$$

where R_{ecs0} is the flow resistance of the ECS between the outer wall of the arterial PVS and the outer boundary. According to equation 2.12, the total flow resistance can be written as

$$R + R_{ecs0} = R_0 \left[\left(\frac{g_0}{g} \right)^4 + \frac{R_{ecs0}}{R_0} \right]. \tag{2.28}$$

The pressure drop across the endfoot wall is then

$$p' = \frac{R_0}{R_0 + R_{ecs0}} p(t). (2.29)$$

This pressure drop causes an azimuthal strain, which can be rewritten as

$$\varepsilon_{\varphi} = \frac{\frac{R_0}{R_0 + R_{ecs0}} p(t) r_0}{ET} (1 - \frac{v}{2}). \tag{2.30}$$

Combining equations 2.27, 2.29, and 2.28 gives the following expression for the total flow rate:

$$Q(t) = \frac{p(t)\left(\frac{R_0}{R_0 + R_{ecs0}} \frac{p(t)r_0}{ET} (1 - \frac{v}{2}) + 1\right)^4}{R_0\left(1 + \left(\frac{R_0}{R_0 + R_{ecs0}} \frac{p(t)r_0}{ET} (1 - \frac{v}{2}) + 1\right)^4 \frac{R_{ecs0}}{R_0}\right)}.$$
 (2.31)

Again, we can rewrite equation 2.31 in terms of ε_{φ} and neglect terms of third and higher order in ε_{φ} , giving

$$Q(t) = Q_0 \frac{\left(\varepsilon_{\varphi} + 4\varepsilon_{\varphi}^2\right)}{1 + 4\varepsilon_{\varphi}\left(\frac{R_{ecs0}}{R_0 + R_{ecs0}}\right)}.$$
(2.32)

The denominator in this expression describes an improved estimate of flow rate, taking into account the flow resistance of the ECS. For this model, we consider the same sinusoidal pressure waveform as before (figure 2.6a). For different values of R_{ecs0}/R_0 , we still observe a greater volume flow in the positive direction than in the reverse direction, and a pumping efficiency that increases monotonically with increasing characteristic strain (figure 2.6b,c). However, as R_{ecs0}/R_0 increases, the net flow volume and the pumping efficiency decrease (figure 2.6b,c,d,e,f). If the flow resistance of the ECS is much smaller than the flow resistance of the endfoot wall ($R_{ecs0}/R_0 \ll 1$), the model is equivalent to that in the previous model,

where the pressure in the ECS is considered to be constant (the black lines in figure 2.6b,c). If the flow resistance of the ECS is much larger than the flow resistance of the endfoot wall ($R_{ecs0}/R_0 \gg 1$), the pumping efficiency is small and the valve mechanism is ineffective (figure 2.6f).

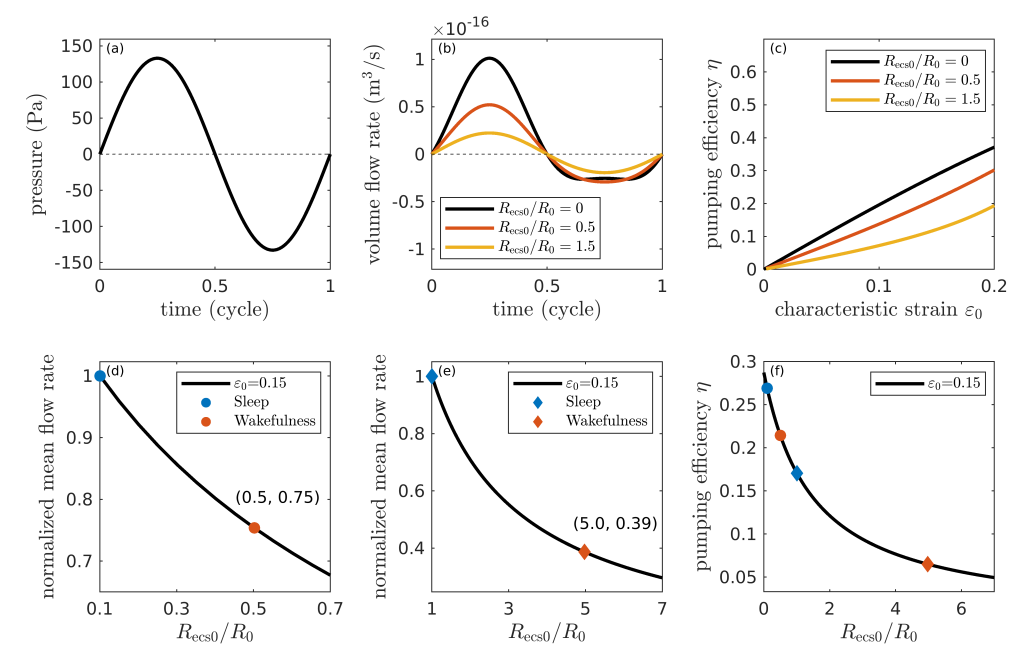


Figure 2.6: (a) Modeled flow in response to a sinusoidal pressure variation, accounting for resistance in the extracellular space (R_{ecs0}) . (b) Increasing R_{ecs0}/R_0 reduces the amount by which forward flow exceeds reverse flow. (c) Increasing R_{ecs0}/R_0 reduces the rate of increase of pumping efficiency with increasing characteristic strain. (d) For the case where $R_{ecs0}/R_0 = 0.1$ during sleep, the mean flow rate during wakefulness (the red dot, $R_{ecs0}/R_0 = 0.5$) is 75% of the mean flow rate during sleep (the blue dot). In the regime $R_{ecs0}/R_0 < 1$, increasing R_{ecs0}/R_0 decreases the normalized mean volume flow rate. (e) For the case where $R_{ecs0}/R_0 = 1$ during sleep, the mean flow rate during wakefulness (the red diamond, $R_{ecs0}/R_0 = 5$) is 39% of the mean flow rate during sleep (the blue diamond). In the regime $R_{ecs0}/R_0 \ge 1$, increasing R_{ecs0}/R_0 decreases the normalized mean volume flow rate. (f) For both regimes, $R_{ecs0}/R_0 < 1$ and $R_{ecs0}/R_0 \ge 1$, the pumping efficiency decreases monotonically with increasing R_{ecs0}/R_0 . The pumping efficiency is smaller during wakefulness than during sleep for the cases considered in panels d and e (the dots and the diamonds).

Less CSF flow is observed during wakefulness than during sleep. The permeability of the ECS decreases by about a factor of five during wakefulness compared to sleep (Xie et al. 2013; Nicholson and Hrabětová 2017; Jeffrey Tithof et al.

2022; J. H. Thomas 2019b). Hence, the flow resistance of the ECS, which is inversely proportional to the permeability (equation 2.10), is about five times larger during wakefulness than during sleep. We can apply our present model to compare the performance of the valve mechanism during wakefulness to its performance during sleep. We consider two representative values of R_{ecs0}/R_0 during sleep, $R_{ecs0}/R_0 = 0.1$ (figure 2.6d) and $R_{ecs0}/R_0 = 1$ (figure 2.6e), and in each case the value of R_{ecs0}/R_0 is five times greater during wakefulness. For these two cases, we find that the mean flow rate during wakefulness is either 75% or 39% of the flow rate during sleep, for the same value of ε_0 . Note that for the case of $R_{ecs0}/R_0 = 1$, a threefold larger pressure in the PVS is needed to cause the same characteristic strain (ε_0) during wakefulness, according to equation 2.30. The pumping efficiency decreases monotonically as R_{ecs0}/R_0 increases (figure 2.6f), and hence, is always smaller during wakefulness than during sleep.

We can estimate the possible range of values of R_{ecs0}/R_0 from previous studies. The flow resistance of the ECS derived by Holter et al. 2017 (see also Jeffrey Tithof et al. 2022) is:

$$R_{ecs0} = \frac{\mu \ln \left(\left[\left(1 - \frac{l_{\text{a-v}}}{r_{\text{artery}}} \right) \right]^2 \right)}{2\pi k_{\text{ecs}} l},$$
(2.33)

where $l_{\rm a-v}\approx 200~\mu{\rm m}$ is the median distance between an artery and the nearest venule, $r_{\rm artery}\approx 8~\mu{\rm m}$ is the radius of the artery, and $k_{\rm ecs}$ is the permeability of the ECS, which falls in the range from $1.2\times 10^{-17}~{\rm m}^2$ (Holter et al. 2017) to $4.5\times 10^{-15}~{\rm m}^2$ (Basser 1992). Therefore, R_{ecs0} is in the range from $3.5\times 10^{16}~{\rm Pa\cdot s/m}^3$ to $1.6\times 10^{14}~{\rm Pa\cdot s/m}^3$. A previous study estimates the endfoot permeability in

the range 2×10^{-11} m/Pa/s to 3×10^{-10} m/Pa/s (Koch, Vegard Vinje, and Mardal 2023). According to equation 2.10, which relates the permeability and the flow resistance, the endfoot flow resistance R_0 is in the range 3.5×10^{16} Pa·s/m³ to 5.3×10^{17} Pa·s/m³. Combining the ranges of both parameters, R_{ecs0}/R_0 falls in the range 2.8×10^{-4} to 1. If $R_{ecs0}/R_0 \ll 1$, the ECS resistance is negligible and the model is equivalent to the previous model. Therefore, the two cases $R_{ecs0}/R_0 = 0.1$ and 1 during sleep (figure 2.6d,e,f), should adequately supplement the previous model.

2.3 The three-dimensional computational model

In order to corroborate the findings of our analytical hoop-stress model, we created a corresponding three-dimensional (3D) computational model of the fluid-solid interactions involved in the flow rectification (figure 2.7). The model employs the software packages preCICE, OpenFOAM, and Fenics (Chourdakis et al. 2022; Weller et al. 1998; Scroggs, Dokken, et al. 2022; Scroggs, Baratta, et al. 2022; Alnaes et al. 2015). The preCICE package is used for the partitioned fluid-structure interaction, coupling OpenFOAM, the fluid-domain solver, and Fenics, the solid-domain solver. OpenFOAM solves for the laminar flow with a moving mesh, and Fenics solves the solid mechanics of the wall using a finite element method. A segment of the PVS with a length of 30 μ m is considered. The endfoot wall, immersed in the computational mesh, separates the outer ECS (at radius 25 μ m) from the inner PVS (at radius 15 μ m) (figure 2.7a,d). The endfoot gaps are modeled

as two square holes of side length 2 μm in the endfoot wall (figure 2.7a,b,c,d; only one hole is shown, and the other is placed symmetrically, on the back of the PVS). The thickness of the endfoot wall is 2 μm . The elastic modulus of the endfoot wall is 30 kPa, and the Poisson ratio is 0.49. The density of the endfoot wall (solid phase) is 100 kg/m^3 . The CSF density is 1000 kg/m^3 , and the dynamic viscosity of the CSF is $10^{-3} \text{ Pa} \cdot \text{s}$.

In figure 2.7c, a positive pressure ($p=100\,\mathrm{Pa}$) is applied to both end boundaries of the PVS, where the ends of the endfoot wall are clamped. Positive pressure in the PVS causes a dilation of the endfoot wall and the gaps, pushing CSF from the PVS into the ECS. In figure 2.7e, a negative pressure ($p=-100\,\mathrm{Pa}$) is applied to both end boundaries of the PVS, causing constriction of the endfoot wall and the gaps while pulling CSF from the ECS into the PVS. We vary the pressure and measure the maximum azimuthal strain by calculating the maximum radial strain $\varepsilon=r/r_0-1$ from the simulations (according to equation 2.4), and we get results similar to those in the hoop-stress model, as shown in figure 2.7c. In figure 2.7f, we calculate the pumping efficiency η using the steady-state solutions from each group of simulations with pressure of the same amplitude but the opposite sign, and compare it with the binary alternating hoop-stress model in figure 2.4c. We find that the results compare favorably. The 3D simulations thus corroborate the hoop-stress model and the basic flow rectification mechanism.

In figures 2.7g,h, we show how slit-shaped gaps (1 μ m \times 4 μ m) deform under the same conditions considered for square holes. Compared to the square cases (figure 2.7c,d), we observe a more dramatic change in gap size due to

bending in addition to uniform stretching, and therefore a higher pumping efficiency (figure 2.7i).

The slit shape is a better model of the realistic geometry of the gaps, which are long and narrow, so the pumping efficiency could be higher than that predicted by the hoop-stress model (figure 2.7f). However, gaps do not always align with the PVS axis. In figure 2.8, we compare the case where the gaps are placed axially (figure 2.8a) and the case where the gaps are placed perpendicular to the axis (figure 2.8b). With the same pressure applied (p = -100 Pa), we find that the perpendicular gaps (figure 2.8b) deform less than the axial gaps (figure 2.8a). That observation is consistent with the fact that simulations of perpendicular gaps more closely match our analytical model (figure 2.8c), which does not account for the extra deformation.

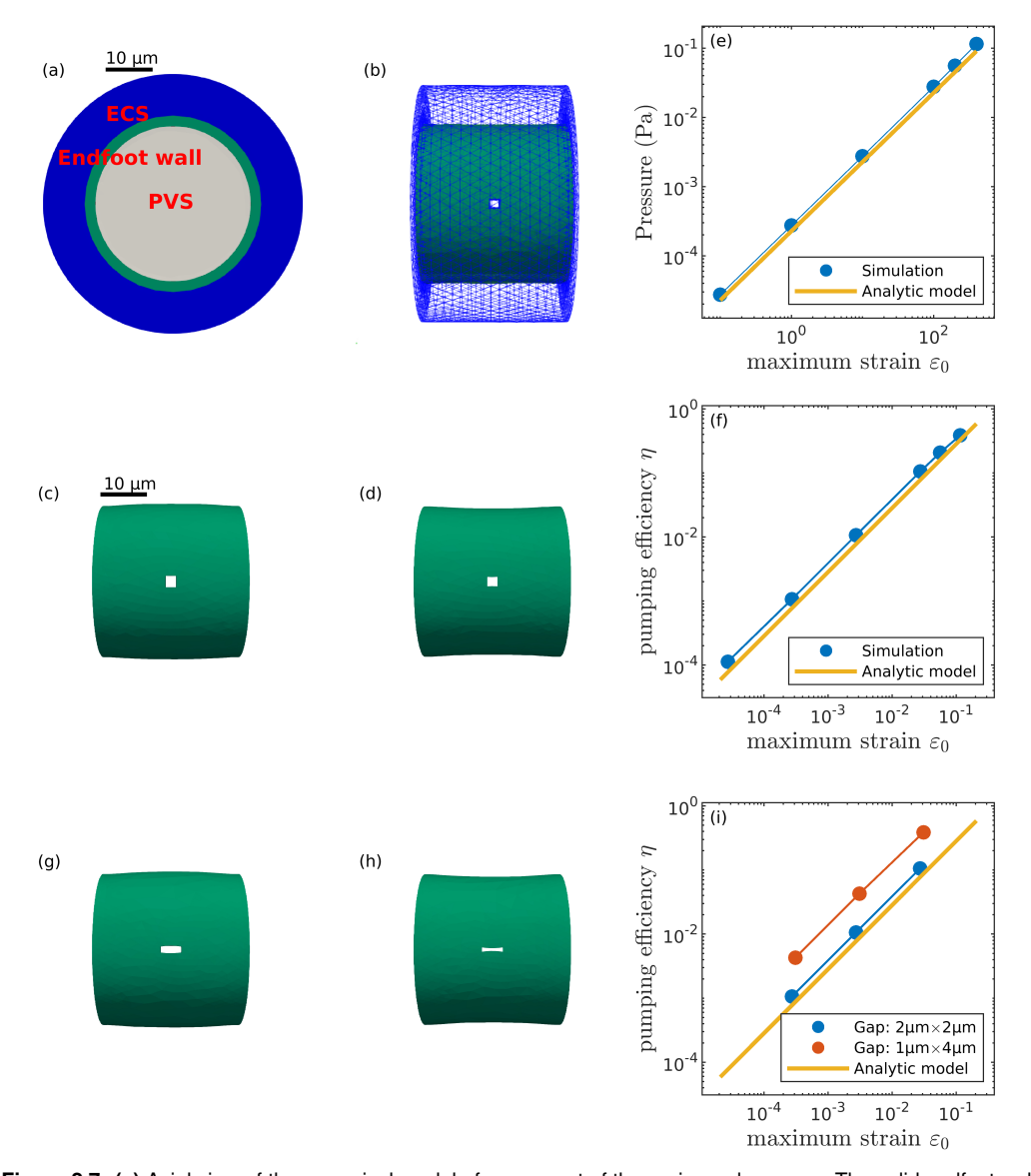


Figure 2.7: (a) Axial view of the numerical model of a segment of the perivascular space. The solid endfoot wall is immersed in the fluid domain, separating the outer extracellular space (ECS, radius 25 μm) from the inner perivascular space (PVS, radius 15 μm). The axial length of the tube is 30 μm. (b), Lateral view of the numerical model. The blue wire frame shows part of the internal mesh for the fluid domain. The endfoot gaps are modeled as two square holes (width 2 µm) on the endfoot wall surface. The thickness of the endfoot wall is 2 µm. (c) A positive pressure boundary condition (p = 100 Pa) applied to both end of the PVS causes a dilation of the endfoot wall and the gaps in it. (d) A negative pressure boundary condition (p = -100 Pa) applied to both ends of the PVS causes a constriction of the endfoot wall and the gaps in it. (e) Strain varies similarly with pressure in simulations and in the analytical hoop-stress prediction. (f) Pumping efficiency varies similarly with strain in the simulations and in the analytical hoop-stress prediction. (g) For the slit-shaped gaps, positive pressure (p = 100 Pa) causes nonuniform deformation and more expansion of the gaps compared to the square gaps in panel c. (h) For the slit-shaped gaps, negative pressure (p = -100 Pa) causes more shrinkage of the gaps compared to the square gaps in panel d. (i) Strain varies similarly with pressure in simulations and in the analytical hoop-stress prediction. We observed higher pumping efficiency in the slit-shaped gaps compared to the square gaps, indicating the stronger rectification due to the extra, uneven deformation. Simulations with pressure amplitudes of p_0 =[1,10,100] Pa are plotted.

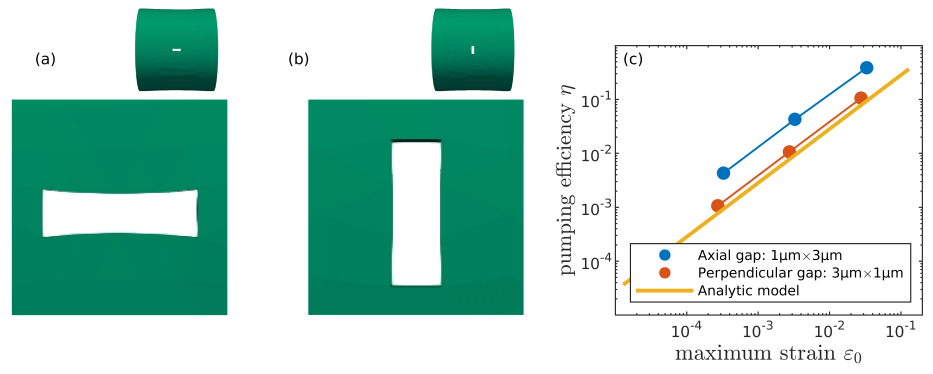


Figure 2.8: (a) The constriction of a slit-shaped gap (1 μ m \times 3 μ m), aligned with the PVS axis, when negative pressure (p=-100 Pa) is applied to both ends of the PVS. (b) The constriction of a slit-shaped gap (3 μ m \times 1 μ m), perpendicular to the PVS axis, when negative pressure (p=-100 Pa) is applied to both ends of the PVS. An axial slit constricts and deforms more. In each case, the lower image is an enlargement of the upper image. (c) Strain varies similarly with pressure in simulations and in the analytical hoop-stress prediction, and agreement is closer for slits perpendicular to the PVS axis. Simulations with pressure amplitudes of p_0 =[1,10,100] Pa are plotted.

2.4 Discussion

In this chapter, we provided a model of a PVS, with a simple annular configuration, in which the endfoot gaps in the outer wall rectify the oscillatory flow of CSF to produce a directed flow. The mechanism is based on the stretching and the constriction of the endfoot wall, and it does not requires any geometric asymmetry of the gaps, unlike a previous study by Bork et al. 2023. The rectification we discuss here can be explained using simple scaling. The artery diameter change drives pressure oscillation in the PVS, and causes radial displacement of the endfoot in the same order of magnitude ($\approx 1 \mu m$, Bojarskaite et al. 2023). With a varying radius, the surface area of the outer wall A is,

$$A = 2\pi r L, \tag{2.34}$$

and the flow resistance of the outer wall reads:

$$R = \frac{1}{kA} = \frac{1}{2\pi r L k} \propto \frac{1}{r},\tag{2.35}$$

where *k* is the permeability of the endfoot wall, which we consider a constant here.

Based on the simple scaling equation 2.35, which does not require permeability k to vary, we know that the flow resistance decreases as the radius r increases (when positive pressure in the PVS causes an inward movement of the endfeet wall), and it increases as r decreases (when negative pressure causes a outward movement of the endfeet wall). How the flow resistance changes with respect to the radius of the endfoot, which is well measured, indicates the gap size change, which is not yet measured, and leads to the development of the valve mechanism. As long as flow is passing through the gaps as they expand and constrict, the flow is rectified. We therefore developed the hoop-stress model to quantify how much the rectification could be, which is a more robust model, as it takes more factors into account, such as the characteristics of the viscous flow through gaps, and the thickness change of the endfoot wall.

Experiments have shown that functional hyperemia (neurovascular-coupled artery motion) drives a radial displacement of the endfeet of $\approx 1.5~\mu m$ for a penetrating artery PVS with a radius of $\approx 10~\mu m$ (Ravi Teja Kedarasetti et al. 2020; Bojarskaite et al. 2023). Based on the hoop-stress model, we can estimate an azimuthal strain of $\varepsilon \approx 0.15$ and a pumping efficiency of ≈ 0.4 for the case of binary alternating pressure, or ≈ 0.3 for the case of sinusoidally varying pressure.

That said, this simple mechanism can produce a mean flow about 30% to 40% as fast as the oscillatory flow, even though the pressure variation is a purely symmetric alternation.

In contrast to functional hyperemia, the radial displacement of endfoot wall due to cardiac pulsation is highly uncertain, and seems to be smaller than current in vivo imaging can register. Due to smaller amplitude of the cardiac pulsation, the pressure oscillation it drives, and hence the endfoot radial displacement (and the azimuthal strain), should be smaller than that driven by functional hyperemia. With that being said, we expect a smaller pumping efficiency from the hoop-stress model. However, the extra deformation we observed from the slit-shape gaps in the 3D simulation indicates that the pumping efficiency could still be significant, even though the radial displacement is small, which we will discuss in the next chapter.

With realistic pressure pulsation amplitudes, for either functional hyperemia or cardiac pulsation, our model predicts pumping efficiency smaller than what is measured in vivo. In fact, even in the case of an ideal valve, which blocks any backflow from any symmetric pressure oscillation (when $\varepsilon_{\phi}=0.25$ according to equation 2.13), the pumping efficiency cannot exceed unity. For the symmetric binary alternating pressure waveform, the maximum pumping efficiency for an ideal valve is $\eta=1/\sqrt{2}$ (when $\varepsilon_{\phi}=0.25$ according to equation 2.19, it is also calculated numerically in the next chapter). That said, this mechanism might work in concert with others, such as the osmotic force, peristalsis pumping, and impedance pumping (Holstein-Rønsbo et al. 2023). Modeling the flow that occurs when other mechanisms are combined is important for future work.

In additional to the radial displacement of the endfoot, the extent to which the deformation changes the flow resistance of a layer of poroelastic tissue (the endfoot wall, in this case) depends on several other factors, none of which are known to high accuracy. Future experiments reducing the uncertainty in the size of the gaps between endfeet, the thickness of the endfeet, their material properties E and V, and the pressure fluctuations in PVSs would make models like ours more precise. Many features of the endfoot geometry are too small to be resolved in vivo but are likely to be altered during the fixation processes necessary for postmortem electron microscopy, so inference from system dynamics may be necessary. Similarly, the pressure can be estimated from observed stretching if the material properties are well known.

Another important factor is the ECS resistance, which connects in series with the flow resistance of the endfoot wall. The ECS resistance suppresses the valve mechanism, but as long as the resistance of the ECS does not exceed that of the endfoot wall by more than an order of magnitude, it does not greatly change the results. That range of ECS resistances is reasonable, according to prior publications. The astrocyte endfoot wall is two orders of magnitude less permeable than a similarly thick layer of ECS (Koch, Vegard Vinje, and Mardal 2023), whereas the ECS is two orders of magnitude thicker than the endfoot wall in our model (we consider the distance between the arterial PVS and the nearest venule, an efflux path in the glymphatic model, taking that distance to be 200 µm, following Holter et al. 2017). Therefore, it is likely that the ECS and endfoot wall have resistances of similar magnitude. However, values of both of these parameters have large

uncertainty and require more precise measurements. During wakefulness, when the resistance of the ECS increases five fold, our model predicts significantly less net flow (61% less for $R_{ecs0}/R_0=1$ if ε_0 is left unchanged; see figure 2.6e) and lower pumping efficiency. These predictions are consistent with in vivo observations, which find little net CSF flow in PVSs during wakefulness (Xie et al. 2013). Note that three times as much pressure is needed to cause the same characteristic strain ε_0 during wakefulness as during sleep, according to our model.

With ECS resistance included, the result matches the experimental observations of suppressed CSF net flow during wakefulness due to increased ECS flow resistance compared to sleep (Xie et al. 2013), indicating that the ECS is an important flow pathway that connects with the PVS. It is necessary to point out that the ECS flow resistance change suppresses the valve mechanism more strongly compared to other driving mechanisms, such as a steady pressure difference. For a flow that is only driven by a steady pressure gradient, the total flow resistance change ratio (including the endfoot and the ECS) is $(R_{\text{ecs,wake}} + R_0)/(R_{\text{ecs,sleep}} + R_0) = 3$, where $R_{\text{ecs,sleep}} = R_0$ represents the ECS flow resistance during sleep, and the $R_{\text{ecs,sleep}} = 5R_0$ represents the ECS flow resistance during wakefulness. Since the pressure difference is steady, the flow should be suppressed threefold, but not more. However, for the valve mechanism, the pressure difference needed for to drive the same amount of flow during wakefulness compared that during sleep is three times larger (figure 2.6e). That is because the increased ECS resistance during wakefulness not only hinders CSF flow, but also strongly suppress the efficiency of the rectification, according to equation 2.32. Therefore, the fact that wakefulness

nearly blocks any CSF flow indicates that valve mechanism may be one of the main drivers of the flow (Xie et al. 2013).

An equation that relates the deformation and the axial flow resistance has been used in previous work (Aldea et al. 2019; Markert 2005). Our model expresses how the deformation changes the radial flow resistance based on the simplified, linear hoop-stress relation and corroborates this dependence with 3D numerical simulations. The model assumes linear elastic behavior of the endfoot wall, based on experimental observations of small deformations (less than 20%): for larger deformations, nonlinearity should be considered for better accuracy. Future experiments are needed in order to validate various aspects of the model.

The mechanism we have considered always favors an outward radial flow, because high pressure in the PVS simultaneously expands the gaps in the endfoot wall and pushes CSF outward through those gaps. Fluid is known to flow outward from arterial PVSs. It is believed, however, that in venous PVSs or nerve sheaths, fluid flows inward through their walls on its way out of the brain. Our mechanism would not favor that inward radial flow, but also would do little to oppose it, because veins and nerves do not pulse appreciably. This sort of valve action, then, would be limited to arterial PVSs.

In the model of sinusoidal alternating pressure, which involves dynamical wall motions, the wall velocity is neglected for simplicity. When the wall is moving, the velocity driven by the pressure difference across the wall is actually the fluid velocity relative to the wall velocity, yet the model remains valid. In experiments, the wall velocity due to cardiac pulsation is $\approx 10 \, \mu m/s$, and that due

to slow neurovascular coupling is ≈ 1 µm/s. The CSF flow velocity relative to the endfoot wall (which represents the net flow transport) is expected to be less than ≈ 1 µm/s (Holter et al. 2017). Since the wall velocity could be an order of magnitude greater than the CSF relative velocity, it would be difficult to measure the latter.

We consider the flow through the endfoot gap as fully developed Poiseuille flow through a channel, neglecting any entrance effect. The flow cannot be considered fully developed if the length of the gap (that is, the thickness of the endfoot wall) is smaller than the entrance length (White 2006). For laminar flow, the entrance length L_e is

$$L_e \approx 0.06 \times \text{Re} \times d$$
 (2.36)

, where Re $\leq 10^{-4}$ is the Reynolds' number, and $d \leq 1~\mu m$ is the diameter of the channel (that is, the gap width). The flow velocity through the endfoot gap has not been directly measured from experiments, but is expected to be much smaller than the flow velocity in the PVSs of the pial artery. Given that Re ≈ 0.01 in those PVSs, it is reasonable to estimate that Re $\leq 10^{-3}$ for the flow through the endfoot gap. Using equation 2.36, we can estimate an entrance length of $L_e \leq 6 \times 10^{-5}~\mu m$, which is much smaller than the typical length of the endfoot gap channel ($\approx 1~\mu m$). Hence, we conclude that neglecting the entrance effect will not severely reduce the accuracy of the model.

In our 3D simulation, we model the gaps as two holes in the endfoot wall, with a hole width of ≈ 2 µm. In reality, there are numerous gaps along the endfoot wall,

and the gap width in vivo could be as small as 20 nm, while the radius of the wall is on the scale of microns (M. X. Wang et al. 2021; Koch, Vegard Vinje, and Mardal 2023). Thus, although the pumping efficiency in our models is meant to estimate the efficiency in vivo, the volume flow rates are not.

Though following the same trend, the hoop-stress model and the 3D simulations differ noticeably in terms of pumping efficiency (figure 2.7f,i). In the hoop-stress model, the flow resistance of the gaps is proportional to Tg^3 , according to equation 2.9, which is based on the realistic slit shape of the gaps Jeffrey Tithof et al. 2022. Yet in the 3D simulation, where the gaps are modeled as square or rectangular holes, the flow resistance is proportional to Tg^4 , according to the solution of Stokes flow passing through a tube of rectangular cross-section (White 2006). Therefore, the flow resistance for the 3D simulation is more sensitive to the value of the gap width g. The pumping efficiency calculated from 3D simulations is always higher than that predicted by the hoop-stress model. Therefore, we do not expect the 3D simulation to match the hoop-stress model exactly.

In reality, gaps are slit-shaped (M. X. Wang et al. 2021). Choosing extreme aspect ratios of the gap to match the realistic geometry for the 3D simulation introduces extra deformation, as discussed in section 3 (figure 2.7i). For the same pressure oscillation waveform, slit-shaped gaps stretch and constrict more dramatically compared to square gaps, causing a better rectification and a higher pumping efficiency. The 3D simulations reveal that the direction of the gaps, like aspect ratio, also plays a role. A lateral gap (the gap with its long edge aligned with the axial direction of the PVS) stretches and constricts more compared to a

perpendicular gap (the gap with its long edge perpendicular to the axial direction of the the PVS). Since the hoop-stress model is limited to uniform deformations, a more complex model is needed to describe and explain these phenomena, which we will discuss in the next chapter.

3. The deformation and the flow resistance change of the slit-shape endfoot gaps under pressure oscillation

The hoop-stress model, which discusses a rectification mechanism based on the stretching and shrinkage of the endfoot gap, is corroborated by three-dimensional fluid-solid interaction simulations. These simulations also provide new insights into the valve mechanism regarding the shape and direction of the gaps. For slit-shaped gaps, a more dramatic change in size and shape is observed compared to the uniform stretching and constriction described in the hoop-stress model, resulting in higher pumping efficiency than square gaps. The lateral gap, with its long edge oriented along the axial direction of the PVS, deforms more compared to the perpendicular gap, where the long edge is perpendicular to the axial direction of the PVS. Since the slit shape is more realistic endfoot gap shape, and the extra

deformation cannot be explained by the hoop-stress model alone, we propose a new model to describe, explain, and quantify the uneven deformation and changes in flow resistance.

The thesis author was the primary contributor of this work.

3.1 Background

Astrocyte endfoot encircles the outer boundary of the penetrating arteries' perivascular spaces (PVSs). Pressure fluctuation inside the PVS causes stretching and constriction of endfoot wall, altering the size and shape of gaps on its surface. These changes in the size and shape of the gaps cause a flow resistance change, which potentially rectify the flow through it (described in chapter 2, Bork et al. 2023; Gan, John H Thomas, and Douglas H Kelley 2024). We provided a hoop-stress model in the previous chapter to quantify rectification, assuming that the gaps stretch and constrict uniformly, in the same way as the elastic tissue on the endfoot wall, which is modeled as a cylindrical one. The 3D numerical simulations, used to validate the hoop-stress model, revealed two additional observations. Firstly, the change in gap size and the resulting alteration in flow resistance are more pronounced for slit-shaped gaps compared to square gaps. Secondly, gaps oriented with their long edge aligned along the axial direction of the PVS (lateral gaps) deform more than those oriented with their long edge perpendicular to the axial direction of the PVS (perpendicular gaps). Microscopic imaging shows that the gaps between the endfeets are of long slit shape, which are long and narrow (M. X. Wang et al. 2021). The orientation of the long axis of these gaps appears to vary rather than align uniformly in a single direction. Hence, it is important to understand how the shape (the aspect ratio) and the direction of the gap influence its potential valve-like action, including its deformation and changes in flow resistance.

A new mathematical model is needed to investigate the observations mentioned above. The method of perturbation is commonly used to determined the stress and deformation of a cylindrical shell with gaps (cutouts) on it (Van Dyke 1965). That is, the gap only influences the stress state in its vicinity. Hence, the stress state far away from the gap can be estimated from the hoop-stress model, while the stress state near it is determined by the boundary condition along the rim of the gap, which can be considered as free of stress (the shear stress applied by the CSF flow is neglected for simplicity). Since there exists no stress on the boundary of the gap to resist the gap from deformation, it stretches and constricts more compared to the endfoot tissues, which is not accounted in the hoop-stress model. Consequently, the long edge of the gap deforms more compared to the short edge, which explains why slit-shaped gaps demonstrate increased and higher pumping efficiency than square gaps.

The model can also explain the effects of gap direction. For a lateral gap, the long edge is stretched and constricted by the azimuthal stress (equation 2.1) whereas the long edge of a perpendicular gap is stretched and constricted by the axial stress (equation 2.2). Since the axial stress is two times smaller than the azimuthal stress, the lateral gap deforms more compared to the perpendicular gap, resulting in higher pumping efficiency.

Using the method of perturbation, Van Dyke 1965 solved the stress and the displacement field of a cylindrical shell with a circular gap on it subjected to various loading conditions, including axial tension, torsion, and internal pressure. The solution, expressed as an infinite series of Hankel functions, is accurate within a wide range of curvature parameters, which evaluates how the curved surface influences the deformation of the circular gap. In subsequent work, Savin, Kosmodamianskii, and Guz 1967 employed conformal mapping techniques to analyze the deformation and stress distribution in gaps of arbitrary shapes, including square gaps, rectangular gaps (of specific aspect ratios), and elliptical gaps. While the rectangular gap can model the slit-shaped endfoot gap with a long edge, it is confined to certain aspect ratios and the accuracy is constrained by the limitation of conformal mapping. In contrast, Murthy 1969 provides exact solutions for an elliptical gap of any eccentricity (i.e. aspect ratio between the long and short axis) using the elliptical coordinates instead of approximating solutions with conformal mapping. We can vary the aspect ratio and the direction of an elliptical gap, making it ideal for studying problems related to slit-shaped endfoot gaps, as discussed above. In addition, using elliptical gaps instead of rectangular gaps avoids sharp corners, making the model more biologically realistic.

Having decided to use the elliptical gap to study the deformation of the endfoot gap, we further employ some simplifications. While Murthy 1969 provides solutions for the elliptical gap on a cylindrical shell under axial tension and torsion, it questions the existence of a closed perturbation solution for the case of internal pressure loading, except for an axial crack (an elliptical gap with length but zero

width). Furthermore, the general solutions, regardless of the loading condition, consist of infinite series and hence may not be as intuitive. Given that the width of the endfoot gap (≈ 20 nm to 1 μ m) is relatively small compared to the radius of the cylindrical endfoot wall ($\approx 10~\mu m$), we neglect the effect of surface curvature and simplify the problem to that of a two-dimensional planar shell with an elliptical gap. The boundary stress conditions far away from the gap are estimated using the hoop-stress model Gan, John H Thomas, and Douglas H Kelley 2024. The lateral stress far away from the gap is estimated by the axial stress (equation 3.2), while the stress in the perpendicular direction far away from the gap is estimated by the azimuthal stress (equation 3.3). The boundary (rim) of the elliptical gap is considered free of any stress. Now that the problem is simplified to a bi-stretching planar shell with an elliptical gap under positive internal PVS pressure and a bi-constricting shell under negative internal PVS pressure, a straightforward and elegant general solution is provided Pollard 1973 in two-dimensional complex plane.

In this chapter, we employ the elliptical gap model on a planar shell to study the slit-shaped endfoot gaps of varying aspect ratios and directions. Using the analytical solutions from Pollard 1973, we quantify the deformation of the elliptical gap of any aspect ratio and any direction. We extract the deformed shape of the gap and calculate the flow resistance change using two-dimensional Strokes flow simulations. Our findings align with previous conclusions that slit-shaped gaps with more extreme aspect ratios exhibit stronger rectification compared to square gaps, and that lateral gaps demonstrate stronger rectification than gaps oriented

in other directions. In addition to changes in gap size, we observe that stretched elliptical gaps exhibit decreased eccentricity, while constricted elliptical gaps show increased eccentricity. Since a less eccentric (more circular) gap has a smaller flow resistance (White 2006), this shape change strengthens the rectification. Lastly, we perform three-dimensional simulations to corroborate the two-dimensional model.

3.2 The 2D shell model

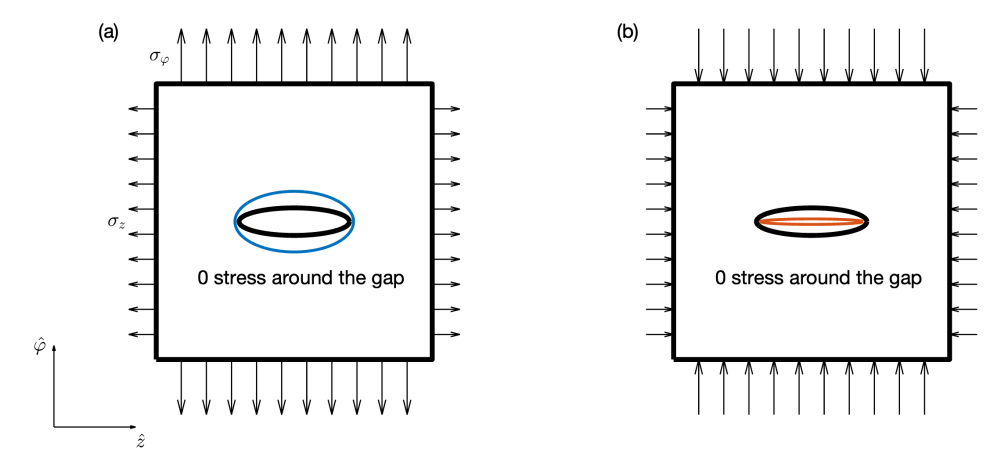


Figure 3.1: The stress boundary conditions for the endfoot tissues (on four edges of the square shell) around the elliptical gap, oriented with its long axis along the axial direction of the PVS (z-direction). (a) When the pressure in the PVS is positive, the axial stress and the azimuthal stress far away from the gaps stretch the endfoot tissue and the gap in both directions. The black curve at the center represents the original gap shape. The blue curve represents the stretched gap. (b) When the pressure in the PVS is negative, the axial stress and the azimuthal stress far away from the gaps constrict the endfoot tissue and the gap. The black curve at the center represents the original gap shape. The blue curve represents the constricted gap shape.

The analytical hoop-stress model approximates that the gaps deform uniformly as the endfoot tissue, neglecting the boundary effect of the gaps, which leads to deviation from the 3D simulation.

Since the gap size is ≈ 20 nm, much smaller than the radius of the endfoot wall

 $(\approx 15~\mu m)$, we can consider the vicinity of the gap as a flat plane (0 curvature). The governing equation for the problem is:

$$\nabla^4 \phi(z, \varphi) = 0 \tag{3.1}$$

, where ϕ is the stress function, z represents the axial coordinate and ϕ represents the azimuthal coordinate.

Since the existence of the gap primarily affects the stress state in its vicinity, it has negligible impact on the stress state far away (at infinity), which can be estimated by the hoop-stress model (Gan, John H Thomas, and Douglas H Kelley 2024). The azimuthal stress reads:

$$\sigma_{\varphi} = \frac{pr_0}{ET} (1 - \frac{v}{2}) \tag{3.2}$$

where p is the internal pressure in the PVS, E is the young modulus, T is the thickness of the endfoot wall, v is the poisson ratio, and r_0 is the radius. The axial stress reads:

$$\sigma_z = \frac{pr_0}{2ET}(1 - \frac{v}{2})\tag{3.3}$$

The boundary (rim) of the gap is free of stress, which reads:

$$\sigma_{\varphi} = 0, \, \sigma_z = 0, \, \tau_{\varphi z} = \tau_{z\varphi} = 0 \tag{3.4}$$

, where $au_{\phi z}$ and $au_{z\phi}$ represent the shear stress. Since the boundary of the gap is free

of stress, it's easier to deform compared to the tissue far away from the gap.

We use the elliptical gaps to represent the slit-shape endfoot gaps, with its long axis representing the long-edge direction of the gap (figure 3.1a,b). The in-plane stress state of the subregion for the case of positive PVS pressure (endfoot expansion) and negative PVS pressure (endfoot shrinkage) are plotted respectively in figure 3.1a,b. The stretched shape and the contricted shape of the gap are plotted in blue color respectively in figure 3.1a,b, using the analytical solutions detailed below.

With the governing equation (equation 3.1) and the boundary conditions (equation 3.2,3.3,3.4), the analytical solution for the circular gap that is bi-directional stretched or constricted is solved, based on which the solution for the rectangular gap is estimated using the method of conformal mapping (Lei, Ng, and Rigby 2001). For the elliptical gap being bi-directional stretched or constricted, the analytical solution is given by Pollard 1973. Which reads:

$$\phi(z, \varphi) = \phi(Z) = \text{Re}(\bar{Z}\psi(Z) + \chi(Z))$$
(3.5)

, where $Z = z + i\varphi$ is the spatial coordinate in the complex domain, ψ and χ are harmonic functions, provided by Pollard 1973. The displacement field reads:

$$u_z + iu_{\varphi} = u(Z) = \frac{\frac{3-4v}{1+v}\psi - Z\frac{d\overline{\psi}}{d\overline{Z}} - \frac{d\overline{\chi}}{d\overline{Z}}}{2G}$$
(3.6)

, where G = E/2(1 + v), is the shear modulus. The analytical results are validated

using the two-dimensional finite-element simulations in Matlab.

Based on the displacement field, we calculate the resistance per unit length for flow through straight channels with cross sections corresponding to the geometry of the deformed gap using numerical simulations (J. Tithof et al. 2019).

3.3 Results

For simplicity, the hoop-stress model assumes that the gap deforms uniformly, and the relative flow resistance change between a constricted gap and a stretched gap for a given pressure amplitude reads:

$$\frac{\Delta R}{R_0} \approx 8\varepsilon_0 = 8\frac{p_0 r_0}{ET} (1 - \frac{v}{2}) \tag{3.7}$$

, where R_0 is the flow resistance at relaxed state, and ΔR represents the flow resistance difference between a constricted gap and a stretched gap (the former is larger than the latter in most of situations), $\varepsilon_0 = p_0 r_0 (1 - v/2)/ET$ is the characteristic strain.

In our 2D shell model, the gap stretches/constricts more dramatically in a nonuniform way, which includes a size change and a shape change, and hence causes a significant flow resistance change. In figure 3.1a, the stretched gap has a larger area and a less eccentric shape, both contributing to a decreased flow resistance. In contrast, the constricted gap exhibits a reduced cross-sectional area and an increased eccentricity, both of which contribute to increased flow

resistance. Therefore, for the 2D shell model, the flow resistance is significantly higher compared to the hoop-stress model, for the same characteristic azimuthal strain, which is proportional to the applied pressure, and the radial displacement of the endfoot wall (figure 3.1b).

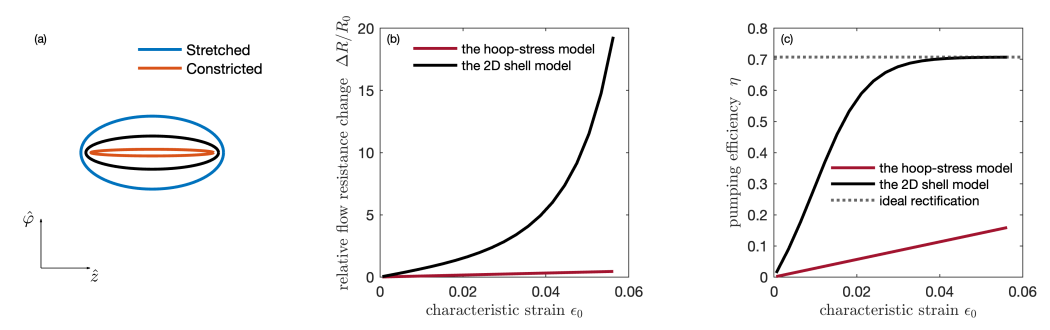


Figure 3.2: The deformation and the flow resistance change of a stretched gap and a constricted gap (a) Deformation of the stretched gap (in blue) and the constricted gaps (in orange). The deformation involves changes in size and shape, causing the flow resistance change. (b) The flow resistance change relative to the original is plotted for various values of the azimuthal strain, which is proportional to the pressure amplitude. For the 2D shell model (the black curve), the flow resistance change is much larger than that compared to the hoop-stress model (the red curve). (c) The pumping efficiency is plotted for various values of the azimuthal strain and compared with the hoop-stress model. The dashed line represents the case of ideal rectification, where the constricted gap prevents any backflow from reentering the PVS.

3.3.1 On the direction of the gap

According to the hoop-stress model, the stress (σ_z) in the lateral direction is smaller than that in the perpendicular direction (σ_{φ}) . The direction of the endfoot gaps (the long axis of the elliptical gap) could be arbitrary (M. X. Wang et al. 2021), and the inhomogeneous stress state suggests an optimal angle β between the long axis direction of the gap and the axis of the PVS. In figure 3.3a, where the gap direction is $\beta = \pi/3$, the deformation of the stretched and constricted gaps is less pronounced compared to the lateral gap shown in figure 3.2a. In figure 3.3b, the

change in flow resistance and the change in area are plotted at different angles between the lateral stress and the direction of the gap. Unlike the flow resistance change, the area change is defined as the difference between a stretched gap and a constricted gap, as the former is larger than the latter. In figure 3.3c, the pumping efficiency decreases as β increases. It reaches maximum values when beta equals 0 (corresponding to the direction of the lateral gap), and it is minimum when beta equals $\beta = \pi/2$ (the perpendicular gap). Therefore, the lateral gaps are optimal for rectifying fluid flow compared to gaps oriented in any other direction. When β is small, the value of pumping efficiency is close to that of an ideal valve (dashed line), which prevents any backflow from reentering the PVS.

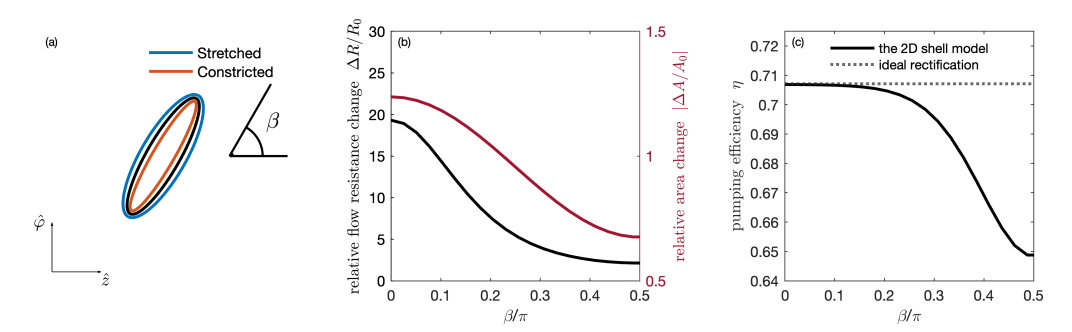


Figure 3.3: The relative flow resistance change between a stretched gap and a constricted gap across different gap directions. The amplitude of the positive and negative pressure in the PVS is 100 Pa. (a) For a gap direction of $\beta=\pi/3$, deformation of the stretched gap and the constricted gaps is less dramatic compared to the lateral gap in figure 3.2a. (b) The relative flow resistance change and area change across different angles between the lateral axial stress and the direction of the gap (β in the range of $[0,\pi/2]$). Both decrease as beta increases, showing that the flow resistance and the area change are maximum when the $\beta=0$ (the lateral gap), and they are minimum are $\beta=\pi/2$, the perpendicular gap. (c) The pumping efficiency across different angles between the lateral axial stress and the direction of the gap. The dashed line represents the case of ideal rectification, where the constricted gap resists any backflow from reentering the PVS.

3.3.2 On the aspect ratio of the gap

In this section, we study how varying the aspect ratio of the elliptical gap affects the change in flow resistance. In figure 3.4a, we find that the deformation of the nearly circular gap is smaller than that of a more elliptical gap (figure 3.2a). In figure 3.4b, the flow resistance change increases as the aspect ratio increases (l/t), where t is the length of the axis in the perpendicular direction, l is the length of the axis in the lateral direction). In figure 3.3c, the pumping efficiency increases as the aspect ratio increases. When l/t is large, the value of pumping efficiency is close to that of an ideal valve (dashed line). Therefore, we conclude that the more eccentric gaps, with the long axis in the lateral (axial) direction, are optimal for rectifying fluid through it compared to gaps that are not as eccentric.

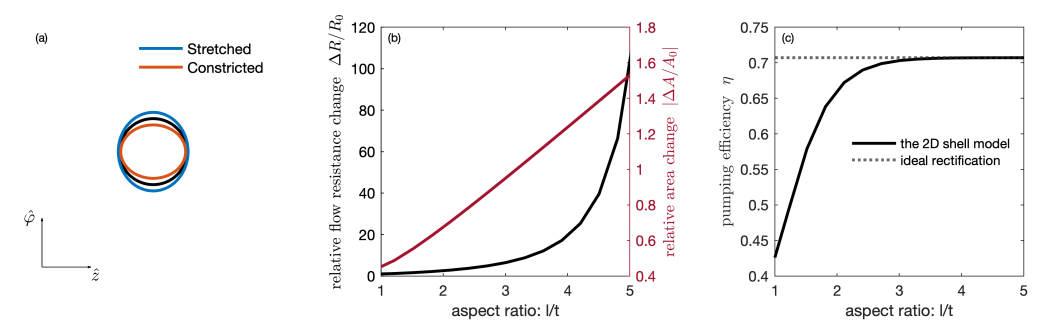


Figure 3.4: The relative flow resistance change ratio and area change between a stretched gap and a constricted gap across different aspect ratios. The amplitude of the positive and negative pressure in the PVS is 100 Pa. **(a)** For a gap aspect ratio of nearly 1 (essentially a circular gap), deformation of the stretched gap and the constricted gaps is less dramatic compared to the more elliptical gap in figure 3.2a. **(b)** The relative flow resistance change across different aspect ratios of the gap (I/t), where t is the length of the short axis of the gap, I is the length of the long axis of the gap. **(c)** The pumping efficiency across different aspect ratios of the gap (I/t), where t is the length of the short axis of the gap, I is the length of the long axis of the gap. The dashed line represents the ideal rectification, where the constricted gap prevents any backflow from reentering the PVS.

3.3.3 The 3D simulation

To validate the 2D model, we conducted 3D finite element method (FEM) simulations comparing the deformation and flow resistance change. The endfoot wall was modeled as a cylindrical shell with a thickness of 2 μm, a radius of 15 μm, and a length of 100 µm (figure 3.5a). In figure 3.5a, the elliptical gap has a long axis (1) of 2 µm and a short axis (t) of 0.5 µm. One end of the cylindrical shell is clamped and open, representing the inlet of the PVS, while the other end is free to deform but closed to represent the capillary end of the PVS. The geometry is meshed using the FEM toolbox of Matlab (figure 3.5b). We directly compare the results of the 2D analytical model and 3D simulations. Since the 2D shell model does not depend on the size of the gap compared to the endfoot wall (which was modeled as an infinite flat plane), we performed two sets of 3D simulations, with one of them using larger gaps and the other using smaller gaps (a four-time smaller area compared to the larger gap). By varying the angle and the aspect ratio of the gap respectively, we find good agreement regarding the area change of the gap between them (figure 3.5d,g), which suggests that the 2D shell model is robust in calculating the deformation of the gaps although it is a simplified model. In terms of flow resistance, which is sensitive to the length change of the gap to the fourth power, the agreement between the 2D model and the 3D simulations is generally good but less satisfactory when dealing with significant deformations, such as the deformation of lateral gaps with extreme aspect ratios (figure 3.5e,g). When the flow resistance change is large, the value of pumping efficiency converges to the pumping efficiency of an ideal valve (dashed line in figure 3.5f,i). Therefore, the

agreement of pumping efficiency between the 2D model and the 3D simulations is good even when dealing with extreme aspect ratios (figure 3.5f,i). Instead, the discrepancy between the analytical model and the simulations is larger when the long axis of the gap is in the perpendicular direction ($\beta = \pi/2$, figure 3.5f), because the flat-plane approximation for the analytical model is less accurate in that curved direction.

3.3.4 Code validations and mesh convergence

A numerical 2D finite element analysis is performed to directly validate the analytical solution of the 2D shell model. The mesh used for the numerical analysis and boundary conditions are illustrated in figure 3.6a. The 2D numerical solution validates the 2D analytical solution for relative flow resistance and area changes across various gap aspect ratios figure 3.6b. The stretched gap shapes calculated using the 2D numerical model and the 2D analytical model also matches each other figure 3.6c.

A mesh convergence test is performed for the Strokes flow simulation by comparing the flow resistance of a stretched and constricted gap using different meshes (figure 3.6d). The mesh size is normalized to the width of the gap's short axis. A mesh convergence test is performed for the 3D simulations by comparing the area and flow resistance of the stretched and constricted gap on the cylindrical endfoot shell using different meshes (figure 3.6e,f).

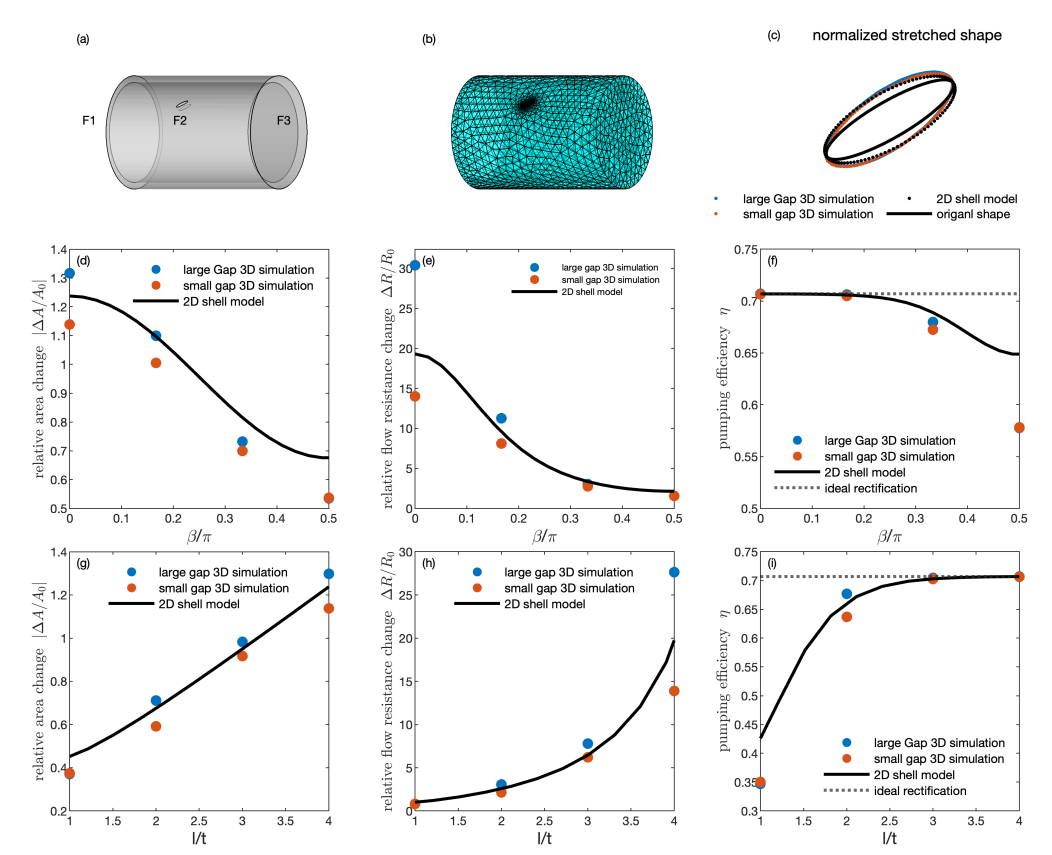


Figure 3.5: Direct 3D simulations that validate the 2D shell model. (a) The setup of the 3D simulations includes a cylindrical shell, which represents the endfoot wall, with an elliptical gap (F2) on it, where stress-free conditions apply. One end of the shell is clamped and open (F1), while the other end is free and closed to simulate the capillary end (F3). Positive pressure or negative pressure is uniformly applied to the inner surface of the shell to model the pressure oscillation in the PVS. The amplitude of the positive and negative pressure is 100 Pa (b) The mesh used for the finite element analysis of the endfoot wall is shown, with a denser distribution of mesh points around the gap. c With a positive pressure of 100 Pa applied in the PVS, the stretched gap shape is calculated using the 2D analytical shell model and the 3D FEM simulations using a larger and a smaller gap. The smaller gap configuration has an area four times smaller than the larger gap. With the area of the gap at rest state (p=0) normalized to unity, the stretched shapes derived from these methods are plotted. (d) The relative area change across different gap directions β is presented and compared between the 2D analytical shell model and the 3D FEM simulations using larger and smaller gaps. The smaller gap configuration has an area four times smaller than the larger gap for the same value of β . (e) The relative flow resistance change across different gap directions is presented and compared between the 2D analytical shell model and the 3D simulations. f The pumping efficiency across different gap directions is presented and compared between the 2D analytical shell model and the 3D simulations. The dashed line represents the case of ideal rectification, where the constricted gap prevents any backflow from reentering the PVS. (g) The relative area change across different aspect ratios is presented and compared between the 2D analytical shell, the 3D FEM simulations model using larger gaps and smaller gaps. The smaller gap configuration has an area four times smaller than the larger gap for the same value of I/t (h) The relative flow resistance change across different aspect ratios is presented and compared between the 2D analytical shell model and the 3D simulations. (I) The pumping efficiency across different aspect ratios is presented and compared between the 2D analytical shell model and the 3D simulations. The dashed line represents the case of ideal rectification, where the constricted gap prevents any backflow from reentering the PVS.

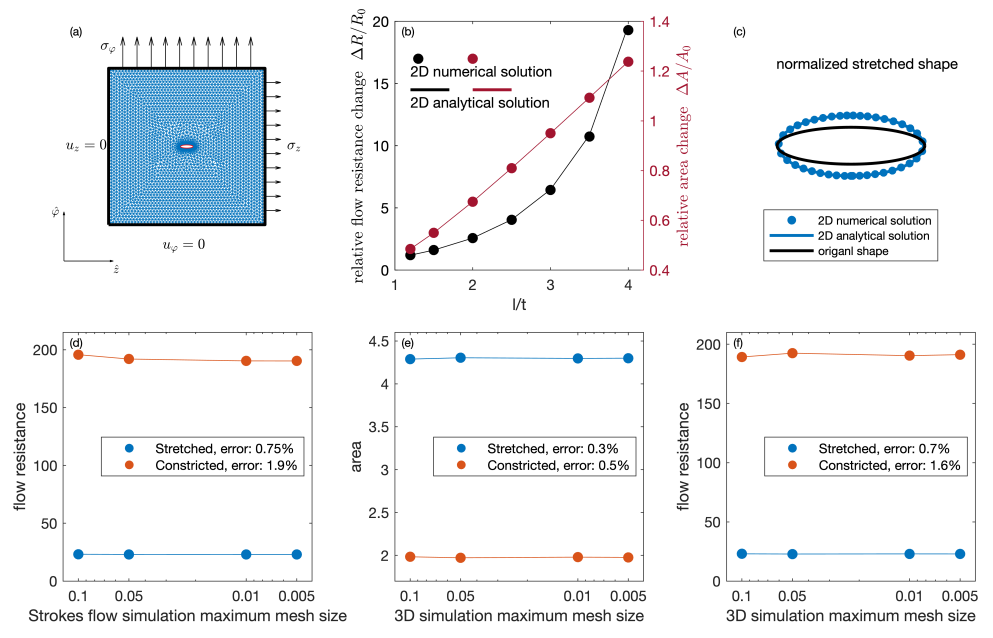


Figure 3.6: Validation of the analytical solution and mesh convergence. (a) A numerical 2D finite element analysis is performed to validate the analytical solution of the 2D shell model. The mesh used for the numerical analysis is shown, with an elliptical gap at the center of a square shell. With stress applied on one edge of the shell $(\sigma_z, \sigma_{\varphi})$, a zero normal displacement boundary condition is applied on the opposite edges $(u_z = 0, u_{\varphi} = 0)$, so that the numerical model is stable equivalent to the 2D analytical shell model. To ensure that the stress is applied far away from the shell, the width of the square shell is set 50 times larger than the short axis of the gap. (b) The 2D numerical solution validates the 2D analytical solution for relative flow resistance and area changes across various gap aspect ratios. (c) With a positive pressure of 100 Pa applied in the PVS, the stretched gap shape is calculated using the 2D numerical model and the 2D analytical model. With the area of the gap at rest state (p=0) normalized to unity, the stretched shapes derived from these methods are plotted. (d) A mesh convergence test is performed for the Strokes flow simulation by comparing the flow resistance of a stretched and constricted gap using different meshes. The mesh size is normalized to the width of the gap's short axis. (e,f) A mesh convergence test is performed for the 3D simulations by comparing the area and flow resistance of the stretched and constricted gap on the cylindrical endfoot shell using different meshes. The maximum mesh size (around the gap) is normalized to the width of the gap's short axis.

3.4 Discussion

In this chapter, we introduce a two-dimensional shell model that fully solved the deformation of the elliptical gap under various aspect ratios and directions during stretching or constriction. In the context of the endfoot gap and the CSF flow, the stretching and constriction are caused by the internal pressure oscillation in the PVS due to the artery pulsations. The model provides precise descriptions of how the gap changes its size, shape, and the flow resistance. It elucidates why gaps with more extreme aspect ratios or gaps aligned with the PVS axis exhibit stronger valve-like properties for rectifying CSF flow when the pressure oscillates, as previously discussed in three-dimensional simulations in the preceding chapter. For the slit-shape gap, the extra deformation and the change in eccentricity of the gap synergistically enhance the rectification and the pumping efficiency.

The extent of the extra deformation of the slit shape gap is much larger than the uniform deformation described by the hoop-stress model, which is proportional to the radial displacement of the endfeet and the azimuthal strain. Hence, the rectification induced by the extra deformation of the slit-shaped gap is significant even with small radial displacement. Functional hyperemia typically induces radial displacements on the order of 1 μ m, whereas the cardiac pulsation drives smaller radial displacements. Consequently, the valve mechanism considered by the hoop-stress model does not rectify the flow pumped by cardiac pulsation efficiently (Gan, John H Thomas, and Douglas H Kelley 2024).

However, our study regarding the extra deformation of the elliptical gaps

demonstrates rectification occurs even with small radial displacements of the endfeet. For example, an azimuthal strain (which can be expressed as the ratio between the radial displacement and the radius of the endfoot at rest) as small as 0.05 causes a relative flow resistance change of 20 (2000%) and a pumping efficiency close to that of an ideal valve that resists any backflow, as shown in figure 3.2b,c. The valve mechanism works efficiently with cardiac pulsation, which is crucial as cardiac pulsation consistently pumps CSF flow forward (Mestre, J. Tithof, et al. 2018). In contrast, functional hyperemia and the slow vasomotion happen only intermittently, during neural activation. In other words, the directional CSF flow persists in the absence of functional hyperemia, but is consistently pumped by cardiac pulsation.

We have theoretically demonstrated that the presence of gaps in the endfoot wall can function as efficient valves through deformation, controlling net flow across the gaps during both functional hyperemia and cardiac pulsations. However, we have not yet explained how the flow across these gaps relates to the axial cerebrospinal fluid (CSF) flow observed in experiments (Mestre, J. Tithof, et al. 2018; Raghunandan et al. 2018), which is parallel to the direction of the blood flow. Our model does not directly couple the artery motion with the flow, but instead uses pressure waveforms to represent them.

In the next chapter, we propose a fluid-solid interaction model that integrates the valve mechanism, the arterial pulsation, the CSF flow in the PVS and the ISF flow in the ECS. This model aims to demonstrate that net flow through the gaps can be directly related to net flow in the axial direction observed in experiments.

4. A perivascular pumping fluiddynamic model with the valve mechanism

In the preceding chapters, we demonstrated that deformable gaps on the endfoot wall could theoretically function as valves, rectifying the directional flow of cerebrospinal fluid (CSF) across these gaps, which is in the radial direction of the annular perivascular spaces (PVS). However, experiments reveal that CSF flows along the axial direction relative to pial arteries. This chapter introduces a perivascular pumping model that connects the rectified radial flow and the observed axial CSF flow. This model integrates artery pulsations and CSF flow using lubrication theory, providing a comprehensive understanding of the fluid dynamics in this system. The results listed in this chapter have been published in Gan, Holstein-Rønsbo, et al. 2023. It has been reformatted and edited to fit within the thesis. The thesis author was the primary author on this work.

4.1 Background

Gaps between astrocyte endfeet, which form the outer boundary of the PVSs of the penetrating arteries, can theoretically act as valves that rectify the flow through them (Bork et al. 2023; Gan, Holstein-Rønsbo, et al. 2023; Gan, John H Thomas, and Douglas H Kelley 2024). However, the mechanism by which the net flow generated by the valve action could be linked with the experimentally observed flow remains unclear.

Particle tracking velocimetry (PTV) experiments, which directly measure CSF flow velocities, are currently constrained to the PVSs surrounding surface pial arteries due to technical challenges. Within these surface PVSs, the CSF flow is usually in the axial direction, moving in the same direction as the blood flow (anterograde).

In this chapter, we propose a perivascular pumping model demonstrating that the flow across the gaps and the axial flow observed in experiments could be directly coupled. Unlike the hoop-stress model (Gan, John H Thomas, and Douglas H Kelley 2024), which uses prescribed pressure waveforms to represent the effects of artery motions, our model incorporates actual pulsations of the arteries into the valve mechanism. During artery dilation, the PVS shrinks, requiring fluid to be expelled, and increased permeability (decreased flow resistance) of the endfoot wall due to the valve mechanism allows fluid to pass into the ECS. During artery constriction, the PVS expands, requiring fluid intake, and reduced permeability (increased flow resistance) of the endfoot wall inhibits a backflow of fluid from

the ECS, so the fluid must instead come from the pial PVS connected to the penetrating PVS. Therefore, the flow in the axial direction is driven in the upstream PVS of the pial artery. In our study, we adopt the lubrication approximation to simulate cerebrospinal fluid (CSF) flow within the perivascular space (PVS) surrounding a penetrating artery, influenced by arterial motions, similar to the approach described in Romanò et al. 2020. The PVS is considered to be an open, unobstructed space, and the outer wall of the PVS (the endfoot wall) is permeable to CSF and deformable. We set the permeability of the outer wall to be a step function of the pressure to model the valve function (Gan, Holstein-Rønsbo, et al. 2023; Bork et al. 2023). We couple the CSF flow in the PVS with the pressure response in the ECS, which is modeled as a porous medium. We find that cardiac pulsations drive a net CSF flow from the upstream pial PVS into the penetrating PVS. Functional hyperemia, acting in addition to the cardiac pulsation, enhances the net flow. We further simplify our model by employing lumped parameters to gain a comprehensive understanding of the pumping mechanism, considering the varied arterial-pulsation frequencies and the elasticities of the endfoot wall.

Again, the perivascular pumping model with our proposed valve mechanism provides insight into how wakefulness suppresses CSF inflow. During wakefulness, the permeability of the ECS is lower by a factor of five than compared to sleep and sleep-like states (Xie et al. 2013). Although cardiac pulsations and functional hyperemia occur in both states, CSF inflow in the PVSs is rarely observed during wakefulness. Solute measurements show that perivascular CSF tracer influx and interstitial solute efflux, including the clearance of amyloid beta, are more rapid

in the sleeping brain compared to the awake brain (Xie et al. 2013). During wakefulness, our model finds a higher ECS pressure response and suppression of CSF inflow in PVSs, consistent with experiments. Few theories of perivascular pumping consider how wakefulness can suppress CSF inflow as they do not include fluid exchange between the PVS and the ECS. Because the astrocytic valves we model here control the net CSF flow transported into the ECS, it is natural to expect that the decreased permeability of the ECS during wakefulness will suppress the valve mechanism.

4.2 The model

Here we describe the idealized computational model of our proposed valve mechanism. Details of the governing equations and numerical methods, based on those of (Romanò et al. 2020), are described in Appendix A. We model the flow of CSF in two connected, axisymmetric domains, as shown in figure 4.1a. The PVS of a penetrating artery is modeled as a circular annular tube of length l and width b, lying between the impermeable, deformable artery and the permeable, deformable endfoot wall. The width of the PVS is taken to be $b = 10 \, \mu m$, the radius of the artery is taken to be $r_1 = 10 \, \mu m$, and the length is taken to be $l = 1000 \, \mu m$, typical values for a penetrating artery in the mouse brain. (Values of all of the dimensional parameters of the model are listed in Table 4.1.) The PVS is an open space (Min Rivas et al. 2020; Jeffrey Tithof et al. 2022), and the flow there obeys the Navier-Stokes equation, in its approximate form for low Reynolds number flow in

Figure 4.1: Sketch of the model. **(a)** The model includes the exchange of cerebrospinal fluid (CSF) between the perivascular space (PVS) of the artery, modeled as an open space, and the extracellular space (ECS), modeled as a porous medium. The upstream PVS of the pial artery and the downstream PVS of a capillary are modeled as flow resistances. **(b)** During artery dilation, hypothesized astrocytic valves along the PVS outer boundary open, facilitating flow into the ECS, which increases the ECS pressure. **(c)** During artery constriction, astrocytic valves close. The constriction drives CSF flow in the PVS and decreases ECS pressure. **(d)** The arterial radius varies during cardiac pulsation according to equation (4.2). **(e)** The asymmetric (n = 2) and symmetric (n = 1) arterial waveforms of functional hyperemia generated by equation (4.3).

a thin tube (the lubrication approximation) and quasi-steady flow (low Womersley number). The aspect ratio of the PVS, $\varepsilon = b/l$, is of order 0.01, justifying the use of the lubrication approximation.

At the inlet (the upstream pial PVS) and the outlet (a precapillary PVS) we specify a hydraulic resistance to model the inflow and outflow and require conserved flow rates across each interface. The inner boundary of the PVS (the artery wall) is assumed to be impermeable, and we apply a no-slip boundary condition there. The

outer boundary of the PVS (formed by the astrocyte endfeet) is modeled as a thin, deformable, elastic layer of permeable tissue, with a no-slip boundary condition. The Young's modulus of this elastic layer, E_{endft} , lies in the range [10^4 10^6] Pa Romanò et al. 2020. To represent the proposed valve mechanism, the permeability k_{endft} of the outer boundary of the PVS is modeled as a step function of the pressure difference:

$$k_{\text{endft}} = \begin{cases} k_1 & \text{if} \quad p(z,t) > p_{\text{ecs}} \\ k_0 & \text{if} \quad p(z,t) \le p_{\text{ecs}} \end{cases}$$

$$(4.1)$$

where $k_1 > k_0$ and $k_0 = 10^{-10}$ m/Pa/s (Koch, Vegard Vinje, and Mardal 2023). Thus, during artery dilation, the increased pressure in the PVS increases the permeability, effectively opening a valve and allowing fluid to enter the ECS (figure 4.1b). During artery constriction, the pressure in the PVS drops, permeability is decreased, the valve closes, and CSF flow is confined to the PVS (figure 4.1c). According to the hoop-stress model, the permeability change is $k_1/k_0 \approx 2.93$, for a pressure amplitude of p = 133 Pa. Therefore, we will examine the permeability change, k_1/k_0 within the range of 1 to 5.

The ECS surrounding the PVS is modeled as a large porous, circular annular tube of length l and width $b_{\rm ecs}$, filled with a porous medium composed of a deformable but incompressible solid phase and an incompressible fluid phase (interstitial fluid) that flows according to Darcy's law. The annular width of the ECS, $b_{\rm ecs}$, is taken to be a typical distance to the nearest venule, which is 100 µm for the mouse brain (Schreder et al. 2022; Jeffrey Tithof et al. 2022). The permeability

of the ECS during wakefulness has been measured as $[2 \times 10^{-17} \text{m}^2 \quad 1 \times 10^{-16} \text{m}^2]$ (Holter et al. 2017; Neeves et al. 2006; Smith and Humphrey 2007). To model sleep, we set the permeability to its maximum value, $k_{\text{ecs}} = 1 \times 10^{-16} \text{ m}^2$, about five times greater than the value we use to model wakefulness (Xie et al. 2013). The flow velocity is kept continuous across the outer boundary of the PVS, where it meets the endfoot wall and the ECS. The pressure difference across this boundary depends on both the elasticity of the thin membrane and the flow rate through it, as described in Appendix A. The fluid pressure is set to zero at the outer boundary of the ECS. The fluid axial pressure gradient is set to zero at the distal and proximal ends of the ECS in z direction,

The motion of the impermeable artery wall is specified as an input, representing cardiac pulsations or functional hyperemia. Given that the wave speed of arterial pulsations is of order $c\approx 1\,\mathrm{m/s}$, the cardiac frequency is $f\approx 3\,\mathrm{Hz}$, and the length of the domain is $l=1000\,\mathrm{\mu m}$, we have $lf/c\approx 0.003$, and hence we can neglect the phase difference in the pulsations along length of the tube. (This phase difference is also negligible for the slower arterial motions associate with functional hyperemia). Thus we model the cardiac pulsations as

$$h(t) = h_{\rm cp} \sin(2\pi f t), \tag{4.2}$$

(figure 4.1d), independent of the axial coordinate z. h_{cp} is the pulsation amplitude. For functional hyperemia, we model an individual pulsation as a quick dilation

followed by a slow constriction and relaxation, in the form

$$h(t) = \begin{cases} \frac{h_{\text{fh}}}{2} \left(1 - \cos(2n\pi f t) \right) & \text{if } t \leq \frac{1}{2nf} \\ \frac{h_{\text{fh}}}{2} \left(1 - \cos(2\left(\frac{1}{2 - \frac{1}{n}}\right)\pi (f t - 1)) \right) & \text{if } \frac{1}{2nf} < t \leq \frac{1}{f} \\ 0 & \text{if } t > \frac{1}{f} \end{cases}$$
(4.3)

with $f \approx 0.1$ Hz, where $h_{\rm fh}$ is the dilation amplitude, and n determines the fraction of dilation time and constriction time. We use n=1 to model temporally symmetric vasomotion and n=2 to model temporally asymmetric vasomotion. In both cases, the waveform is smooth, with a continuous wall velocity (figure 4.1e).

и	axial CSF velocity	
w	radial CSF velocity	
r	radial coordinate	
z	axial coordinate	
t	time	
p	pressure in the PVS	
\overline{q}	axial flow rate in the PVS	
f	the arterial pulsation frequency	
μ	dynamic viscosity of CSF	$9 \times 10^{-4} \text{ Pa} \cdot \text{s}$
r_1	artery radius	10 μm
l	length of the penetrating artery	1000 μm
$h_{\rm cp}$	artery pulsation amplitude of the cardiac pulsation	$*[0.01r_1, 0.025r_1]$
$h_{ m fh}$	artery dilation amplitude of functional hyperemia	$*[0.1r_1, 0.2r_1]$
h	arterial waveform of cardiac pulsation or functional hyperemia	
b	width of the PVS	10 μm
a_{pvs}	equilibrium cross-sectional area of the PVS	940 μm ²
$E_{ m endft}$	elasticity of the PVS outer boundary	*[10 ⁴ ,10 ⁶] Pa
kendft	permeability of the PVS outer boundary	10 ⁻¹⁰ m/Pa/s
$k_{\rm pial}$	conductivity of the pial PVS	$1000k_{\rm endft}a_{\rm pvs}$
$k_{\rm cap}$	conductivity of the capillary PVS	$k_{\rm endft}a_{\rm pvs}$
$k_{\rm ecs}$	permeability of the ECS	$*[10^{-16},2\times10^{-17}] \text{ m}^2$
$b_{ m ecs}$	width of the ECS domain/distance between	
	the artery and the venules	10^{-4} m
u^*	axial CSF velocity relative to the endfeet motion	

4.3 **Results**

With the valve mechanism, cardiac pulsations drive 4.3.1 a net CSF influx

We modeled flow driven by cardiac pulsations, which have high frequency (2-6 Hz) but small amplitude (1% to 5%). We first tested the model using an essentially

Figure 4.2: Flow and pressure driven by ten cycles of cardiac pulsation (f=3 Hz). **(a)**, As the artery dilates and constricts, the volume flow rate at the inlet of the penetrating perivascular space oscillates symmetrically around zero if no valve mechanism is implemented $(k_1/k_0=1)$, but favors inflow when the valve mechanism is active $(k_1/k_0=5)$. **(b)**, Net volume of fluid pumped into the penetrating perivascular space, starting at the beginning of the fifth cycle to avoid transients. The volume fluctuates but increases, on average, at a rate depending on the permeability ratio k_1/k_0 . **(c)**, Pressure fluctuations in the penetrating perivascular space, varying with endfoot wall elasticity $E_{\rm endft}$. In all cases, $k_1/k_0=5$. Softer walls deform more, reducing pressure fluctuations. **(d)**, Mean fluid velocity in the perivascular space, over the last five cardiac cycles, shows net inflow. **(e)**, The mean flow rate at the inlet increases with permeability ratio and wall elasticity. **(f)**, The mean pressure gradient at the pial PVS inlet (over five cycles) likewise increases with permeability ratio and wall elasticity.

rigid endfoot wall with elasticity $E_{\rm endft} = 10^6$ Pa, roughly an order of magnitude higher than measured for artery walls Messas, Pernot, and Couade 2013. In the

 $k_1/k_0 = 1$ case, where wall permeability remains constant and no valve action occurs, the inflow and backflow rates for each cycle were the same, resulting in zero net flow (figure 4.2a,b). With $k_1/k_0 > 1$, however, we observed less backflow than inflow and hence a net flow.

For a more compliant endfoot wall, we expect increased wall deformation that would absorb more of the arterial pump energy. To test this expectation, we performed simulations varying E_{endft} . We measured the mean flow rate $\int_0^{t_0} q \, dt / t_0$ (where q is the instantaneous volume flow rate) and the pressure difference between the two ends of the PVS. Both increased with k_1/k_0 and decreased for a more compliant endfoot wall, as expected (figure 4.2c-e). We observed a mean pressure gradient at the pial entrance on the order of 100 Pa/m (figure 4.2f), which matches experimental measurements (K. A. Boster et al. 2023) and other numerical models (Daversin-Catty et al. 2020; Ravi Teja Kedarasetti et al. 2020).

4.3.2 The valve mechanism is suppressed during wakefulness

In vivo experiments show that, compared to sleep or anesthesia, wakefulness results in smaller ECS permeability and reduced CSF influx (Xie et al. 2013; L. M. Hablitz et al. 2019). In this section, we show that our model likewise predicts reduced net flux during wakefulness. We modeled the difference between sleep and wakefulness by varying $k_{\rm ecs}$ from $2 \times 10^{-17} {\rm m}^2$ to $1 \times 10^{-16} {\rm m}^2$. For small $k_{\rm ecs}$ (wakefulness), we found an increased pressure response in the ECS and a reduced

net flow of CSF (figure 4.3a,b). Higher pressure in the ECS during wakefulness (figure 4.3c-d) hinders CSF entering across the endfoot wall, resulting in less axial CSF influx.

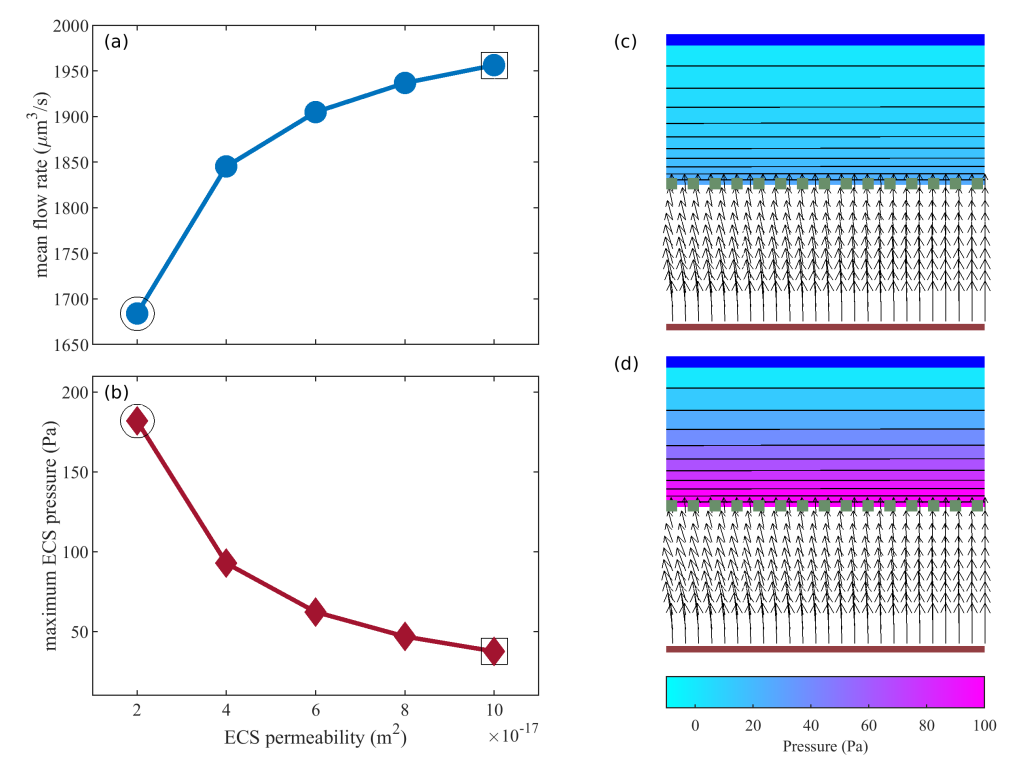


Figure 4.3: Modeling sleep-wake differences by varying the permeability of the extracellular space (ECS). (a), The mean flow rate at the pial entrance increases with ECS permeability. (b), The maximum pressure in the perivascular space decreases ECS permeability. (c), Instantaneous ECS pressure and PVS velocity, during artery dilation by 5%, with ECS permeability $k_{\rm ecs} = 1 \times 10^{-16} \, {\rm m}^2$, corresponding to points marked with circles in a-b. (d), Instantaneous ECS pressure and PVS velocity, during artery dilation by 5%, with ECS permeability $k_{\rm ecs} = 2 \times 10^{-17} \, {\rm m}^2$, corresponding to points marked with squares in a-b. Greater permeability, as expected during sleep, leads to much lower pressure gradients in the ECS, even for stronger artery dilation.

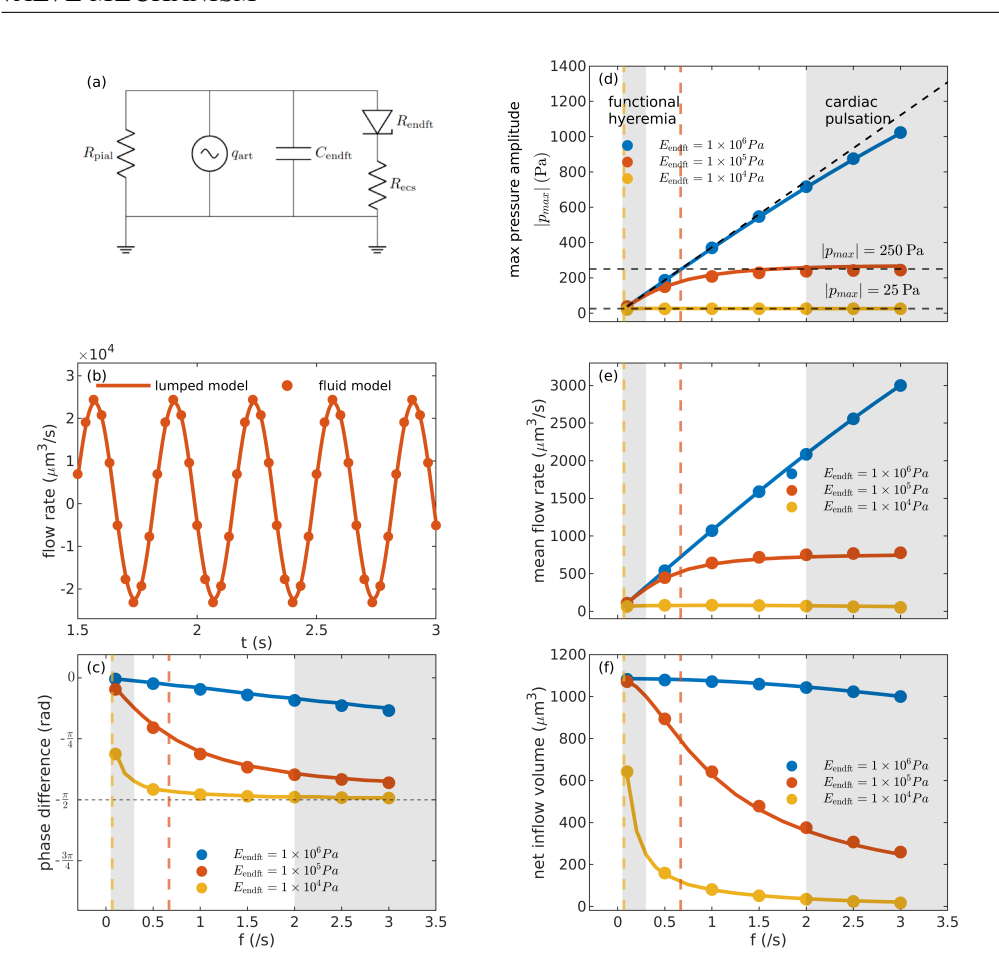


Figure 4.4: The lumped parameter model simplified from the fluid dynamic model and the frequency analysis. **(a)** Sketch of the lumped-parameter model. The volume change due to arterial pulsation is modeled as a flow source. Pathways to the pial PVS and the ECS each have a hydraulic resistance, and the endfoot wall is compliant. **(b)** In the absence of valve action, the fluid dynamical and lumped-parameter models predict similar pial PVS inflow rates in response to cardiac pulsations. **(c)** In the absence of valve action, the two models predict similar phase difference between wall velocity and q_{pial} . In panels c-d, simulation results are plotted as circles, and predictions from the lumped-parameter model are plotted as curves. In panels c-f, vertical dashed lines mark the characteristic frequencies ($R_{\text{eff}}C_{\text{endft}}$)⁻¹. **(d)** In the absence of valve action, the two models predict similar maximum pressure p_{max} , which is proportional to f when f is small and approaches a constant value when f is large. **(e)** With valve action, the lumped parameter model (dots) and the fluid dynamical model (solid lines) predict that the mean flow rate varies with f in much the same way as p_{max} does in the absence of valve action. **(f)** With valve action, the lumped parameter model (dots) and the fluid dynamical model (solid lines) predict that the net inflow per cycle is maximum at low frequencies and decreases rapidly as f exceeds ($R_{\text{eff}}C_{\text{endft}}$)⁻¹.

4.3.3 A lumped-parameter model and the frequency analysis

We further simplify our model in terms of lumped parameters (details of the simplified model are included in Appendix). There are two pathways by which fluid can enter or exit the penetrating PVS, as sketched in figure 4.4a: fluid can be exchanged with the pial PVS or the extracellular space, via the endfoot wall. R_{pial} , R_{ecs} , and R_{endft} represent the flow resistance in the pial PVS, ECS, and endfoot wall, respectively. Since the value of R_{endft} depends on the pressure difference (analogous to voltage) across it according to equation 4.1, we represent it as a Zener diode, a circuit device whose resistance is much higher (though not infinite) for reverse flow than forward flow. Flow through the capillary PVS is negligible because their resistance far exceeds that of the ECS and endfoot wall. The flow resistance within the penetrating PVS itself is negligible.

Fluid motion induced by the prescribed arterial pulsation is modeled as a flow source (analogous to a current source) with a volume flow rate equal to the rate of change of the artery volume:

$$q_{\rm art} = \frac{\partial}{\partial t} \left(\pi (r_1 + h)^2 l \right) \approx 2\pi r_1 l \frac{\partial h}{\partial t}.$$
 (4.4)

Here, the final expression results from neglecting terms that are second-order small, given that $h \ll r_1$. In addition to the change of the artery volume, the pressure-dependent deformation of the endfoot wall (analogous to capacitance) also causes

a change of PVS volume, which can be represented as a source with flow rate

$$q_{\text{compliance}} = \frac{\partial}{\partial t} \left(\pi l ((r_1 + b + d)^2 - (r_1 + b)^2) \right) \approx 2\pi (r_1 + b) l \frac{\partial d}{\partial t} = C_{\text{endft}} \frac{\partial p}{\partial t}, \tag{4.5}$$

where $C_{\text{endft}} = 2\pi l(r_1 + b)^2 E_{\text{endft}}^{-1}$, given that the deformation of the endfoot wall is proportional to pressure (equation A.8 in Appendix A). The system is then a parallel circuit (figure 4.4a) governed by

$$\frac{p}{R_{\text{endft}} + R_{\text{ecs}}} + \frac{p}{R_{\text{pial}}} + C_{\text{endft}} \frac{\partial p}{\partial t} = q_{\text{art}}.$$
 (4.6)

For convenience, we define $q_{\rm pial} = -pR_{\rm pial}^{-1}$ (the inflow rate from the pial PVS) and $q_{\rm ecs} = p(R_{\rm endft} + R_{\rm ecs})^{-1}$ (the outflow rate to the ECS).

Figure 4.4b shows that the value of $q_{\rm pial}$ predicted by the lumped-parameter model is close to that of the fluid dynamical model. Since the lumped-parameter model is simple, we can quickly study analytically how the system responds to arterial pulsations of different frequencies. Using equation 4.2 in the absence of the valve mechanism ($R_{\rm endft}=0$) and neglecting transients, we can solve for $q_{\rm pial}$ analytically:

$$q_{\text{pial}} = \frac{4\pi^2 r_1 l h_{\text{cp}} f}{R_{\text{pial}} C_{\text{endft}} \sqrt{4\pi^2 f^2 + (\frac{1}{R_{\text{eff}} C_{\text{endft}}})^2}} e^{2\pi i (ft - \frac{\arctan(2\pi f R_{\text{eff}} C_{\text{endft}})}{2\pi})}, \tag{4.7}$$

where R_{eff} is the effective flow resistance of the lumped parameter model ($R_{\text{eff}}^{-1} = (R_{\text{endft}} + R_{\text{ecs}})^{-1} + R_{\text{pial}}^{-1}$). Though equation 4.7 does not account for the valve

mechanism, it fully describes how the arterial pulsation frequency f and the endfoot wall elasticity E_{endft} influence the flow rate.

The exponential term in equation 4.7 describes the phase of $q_{\rm pial}$, from which we can calculate the phase difference between the arterial wall velocity and the inflow rate. In figure 4.4c, we calculate the phase difference for various pulsation frequencies f and $E_{\rm endft}$ and find that it matches the simulation result. Based on equation 4.7, the phase difference increases as we increase f or decrease $E_{\rm endft}$, eventually converging to $-\pi/2$. The phase difference changes most rapidly when the pulsation timescale f^{-1} is similar to the characteristic relaxation time $R_{\rm eff}C_{\rm endft}$ of the compliant system.

The initial factor in equation 4.7 describes the maximum value of $q_{\rm pial}$ and the maximum value of p. In figure 4.4d, we plot the maximum value of p for various pulsation frequencies f and $E_{\rm endft}$, which also matches the simulation result with the valve. When f is small or $E_{\rm endft}$ is large, the maximum value of p is proportional to f, whereas when f becomes large or $E_{\rm endft}$ becomes small, the maximum value of p approaches a constant. Both limiting cases are consistent with our expectations from the lumped-parameter model. First, equation 4.4 implies that $q_{\rm art} \sim \partial h/\partial t \sim fh$. Then, when f is small, the compliance term in equation 4.6 becomes negligible, so that $p \sim q_{\rm art} \sim f$. On the other hand, when f is large, the compliance term dominates because $\partial p/\partial t \sim fp$, so $p \sim q_{\rm art}/f$, a constant. The small and large frequency ranges are separated by $(R_{\rm eff}C_{\rm endft})^{-1}$, the inverse of the characteristic relaxation time.

In figure 4.4e, we show the mean inflow rate per cycle with the valve mechanism

in effect (with $k_1/k_0 = 2$), which follows the same trend as the maximum p in figure 4.4d, again increasing with f at low frequencies but saturating at high frequencies, with the two frequency regimes separated by $(R_{\rm eff}C_{\rm endft})^{-1}$. The increase with f at low frequencies can be explained by the higher wall velocities that occur at higher frequencies (for constant amplitude). Saturation at higher frequencies can be explained by rapid endfoot deformations damping the pumping. In the same way, as f increases, the net inflow volume per one cycle is nearly constant for large $E_{\rm endft}$ but gradually decreases for small $E_{\rm endft}$, still depending on $(R_{\rm eff}C_{\rm endft})^{-1}$ (figure 4.4f). The numerical solutions of the lumped parameter model (solid line) and the full fluid dynamic model (dots) in figure 4.4e and figure 4.4f match very well.

4.3.4 With the valve mechanism, functional hyperemia drives a net CSF influx in addition to that produced by cardiac pulsation

Next, we model flow driven when functional hyperemia, which has a longer time scale (5 to 20 s) but a larger oscillation amplitude (10 to 20%), occurs in addition to cardiac pulsation (figure 4.5a). We observe an increased net inflow volume for the coupled waveform compared to that of cardiac pulsation acting alone (figure 4.1d, figure 4.5b). We can also consider the hypothetical situation, which is physiologically impossible but nonetheless informative, of functional hyperemia acting in the absence of cardiac pulsation (figure 4.1e). We observe that acting

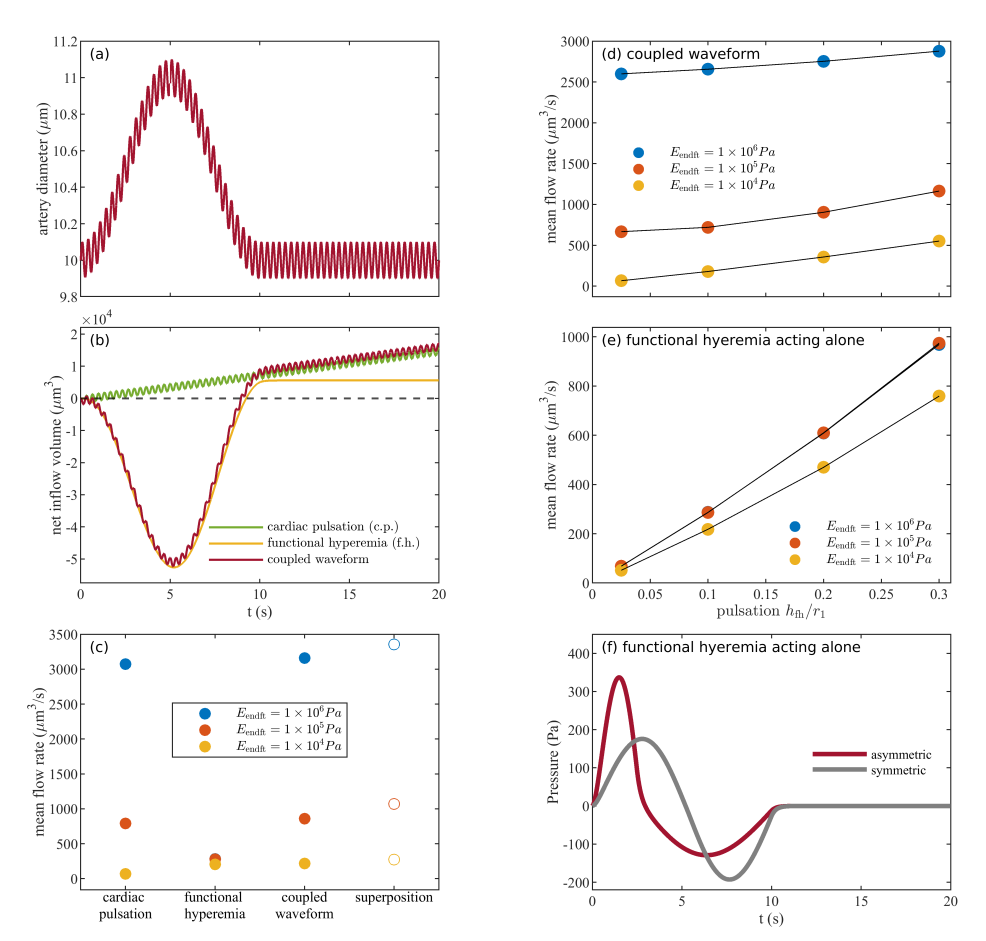


Figure 4.5: Modeling valve action during functional hyperemia. **(a)**, the arterial waveform that couples the cardiac pulsation and functional hyperemia. **(b)**, We observed an increased net inflow volume over time for the coupled waveform compared to cardiac pulsation or functional hyperemia acting alone. **(c)**, Comparison between the mean inflow rate driven by cardiac pulsation, functional hyperemia, the coupled waveform, and the superposition of the first two mean flow rates **(d)** The mean flow rate driven by the coupled waveform increases as with the dilation percentage, $h_{\rm fh}/r_1$, and the increase is more significant for $E_{\rm endft}=10^4$ Pa **(e)** The mean flow rate driven by functional hyperemia acting alone increases with $h_{\rm fh}/r_1$ **(f)** Asymmetric variation includes a quick dilation that greatly increases pressure.

alone, functional hyperemia drives less net inflow than either cardiac pulsation alone or their combination (figure 4.5b).

In figure 4.5c, we show the mean inflow rates driven by cardiac pulsation alone, functional hyperemia in combination with cardiac pulsation, and functional

hyperemia alone. Though the mean flow rate for the coupled waveform is larger than for either mechanism acting alone, it is also smaller than the sum of the mean flow rates induced independently by the two mechanisms. Valve action is a nonlinear process, so superposition does not hold; the rectified, summed flow is smaller than the sum of the rectified flows (see Appendix A).

We also observe that the mean flow rate driven by the cardiac pulsation is larger than the mean flow rate driven by functional hyperemia for large $E_{\rm endft}$, which is consistent with figure 4.4e. That is because there are many cycles of cardiac pulsation during one episode functional hyperemia (figure 4.5a). However, when the compliance of the endfoot wall is relatively low ($E_{\rm endft}=10^4$ Pa), functional hyperemia drives a larger mean flow rate than cardiac pulsation because the more compliant endfoot wall filters the high-frequency pulsation (figure 4.4d-f).

In figure 4.5d, we plot the mean flow rate for the coupled waveform. The mean flow rate increases as $h_{\rm fh}$ increases. When $E_{\rm endft}$ is large, the increase is less significant because the cardiac pulsation (the high frequency pulsation) dominates the pumping mechanism. In contrast, for smaller $E_{\rm endft}$, functional hyperemia dominates, and the increase of mean flow rate with $h_{\rm fh}$ is significant. In figure 4.5e, we plot the mean flow rate for the functional hyperemia waveform acting alone. The mean flow rate increases as $h_{\rm fh}$ increases and is less affected by $E_{\rm endft}$ (the mean flow rate for $E_{\rm endft} = 10^6$ Pa is nearly identical to that for $E_{\rm endft} = 10^5$ Pa).

A previous study by R. T. Kedarasetti, Drew, and Costanzo 2022 found that a more realistic, asymmetric artery pulsation waveform, composed of a fast dilation and a slow constriction, increased the net flux across the endfoot wall, perhaps

because fast dilation pushes more fluid into the ECS. We compared the effects of a simple pulsation waveform to those of the more realistic, asymmetric waveform (figure 4.1e) considered in R. T. Kedarasetti, Drew, and Costanzo 2022. Pressure in the PVS increased rapidly during fast dilation, reaching a large maximum value(figure 4.5f). During slow constriction, however, the reverse pressure amplitude change was weaker but slower. On the other hand, the simple pulsation waveform induced pressures of nearly equal amplitude during dilation and constriction. We also observed an 8% increase in the axial net flux for the more realistic, asymmetric waveform, as compared to the simple waveform, given $k_1/k_0 = 2$, $E_{\rm endft} = 10^5$ Pa.

4.4 Discussion

Gaps between astrocyte endfeet may theoretically act as valves that produce net flow across them, regulating the flow exchange between the CSF in the PVS and the ISF in the ECS (Gan, John H Thomas, and Douglas H Kelley 2024; Bork et al. 2023). Here we propose the perivascular pumping model, demonstrating that existence of valve-like action at the astrocyte endfeet as an explanation for the observed directed net flow in PVSs of the pial arteries. Our simulations model that action as a pressure-dependent permeability and predict that flow from PVS to ECS during artery dilation exceeds flow in the reverse direction during constriction, resulting in net fluid motion over time in the direction parallel to blood flow. Hence, it provides strong evidence that the net flow rectified by the endfoot gaps can

directly result in the axial CSF flow that previous studies observed in the PVS of the pial artery.

The pumping mechanism proposed here is based on the assumption that $k_{\rm endft}$ is larger when $p > p_{\rm ecs}$ than when $p \le p_{\rm ecs}$ (equation 4.1), which is supported by the hoop-stress model (Gan, John H Thomas, and Douglas H Kelley 2024) and a recent study of the mechanics of the endfoot gaps (Bork et al. 2023). One might, alternatively, imagine that $k_{\rm endft}$ or $k_{\rm ecs}$ is smaller when $p > p_{\rm ecs}$, which would lead to a reverse flow (opposite the direction of blood flow) in our model (Diem et al. 2017). The gaps between end feet and poles in the ECS might conceivably shrink when being squeezed by the pressure difference, causing reduced permeability. However, given the consistent experimental observations of forward CSF flow, we adopt the former assumption for our pumping model.

We find that greater variation of permeability with pressure leads to greater net flow. Greater rigidity of the endfoot wall and the surrounding brain tissue also increases net flow, along with instantaneous pressure fluctuations in the PVS. Reduced permeability (increased flow resistance) of surrounding brain tissue, as expected during wakefulness, leads to reduced net flow and increased mean pressure in the ECS, consistent with prior observations that glymphatic function is reduced during wakefulness. Net flow is driven by artery wall motions with frequency and amplitude characteristic of cardiac pulsation or functional hyperemia, although some frequencies pump more effectively than others (figure 4.5e), and by either symmetric or asymmetric pulsation waveforms.

Thus, the presence of valve-like action at the endfeet is consistent with many

phenomena observed previously, including strong pumping by functional hyperemia (Ravi Teja Kedarasetti et al. 2020; Veluw et al. 2020; Holstein-Rønsbo et al. 2023) and pumping by cardiac pulsations in the absence of functional hyperemia (Bedussi et al. 2017; Mestre, J. Tithof, et al. 2018; Raghunandan et al. 2018). Because our model assumes artery dilation and constriction to be uniform along the penetrating PVS, the observed effects do not depend on wavelength, wave speed, or the presence of traveling waves, in contrast to proposed peristalsis-like mechanisms (Hadaczek et al. 2006; Carr et al. 2021). Nor do the observed effects require temporal asymmetry of the artery pulsation waveform, though rapid dilation does increase net flow, consistent with prior modeling (R. T. Kedarasetti, Drew, and Costanzo 2022). In our simulations, that effect can be explained by the concomitantly higher instantaneous pressure, which coincides with increased permeability (and therefore lower resistance) at the endfoot wall. We also point out that flow rectification is a nonlinear phenomenon, and by definition, nonlinearity is amplified as magnitudes (of velocity and pressure, in this case) grow. That said, the presence of valve-like action does not exclude other proposed pumping mechanisms, such as impedance pumping (Avrahami and Gharib 2008; Holstein-Rønsbo et al. 2023).

The pressures predicted by our model depend sensitively on the elasticity of the endfoot wall and the elasticity and permeability of the surrounding tissue. In some cases, PVS pressure reached -1000 Pa = -7.5 mmHg (figure 4.2c). Though measurements of the pressure distribution in the brain in vivo are quite difficult, these values are much higher than the expected ~ 1 mmHg maximum pressure difference across the glymphatic system (Jeffrey Tithof et al. 2022; Penn and

Linninger 2009). Those extreme pressures, however, occurred only when the wall elasticity was $E_{\rm endft}=10^6$ Pa, much stiffer than we would expect (K. A. Boster et al. 2023; Ravi Teja Kedarasetti et al. 2020). With a smaller elasticity ($E_{\rm endft}=10^5$ Pa), PVS pressure reaches 200 Pa = 1.5 mmHg, more reasonably. The pressure gradient at the PVS inlet was around 100 Pa/m. Recent work using artificial intelligence velocimetry K. A. Boster et al. 2023 reports a time-averaged pressure gradient of 275 Pa/m in pial (not penetrating) PVS, which is of the same order of magnitude. Similar values were found in recent simulations (Ravi Teja Kedarasetti et al. 2020; Daversin-Catty et al. 2020). In the ECS, maximum pressure ranged from about 50 Pa = 0.38 mmHg when the permeability was $k_{\rm ecs}=10^{-16}$ m² to 200 Pa = 1.5 mmHg with $k_{\rm ecs}=2\times10^{-17}$ m² (figure 4.3b).

An effective valve mechanism does not necessarily require discrete, localized valves: it can be produced by an asymmetry along the flow pathway. Candidates for valves may include the astrocyte endfeet and valves along the perivenous space or the lymph vessels (the exit of the CSF pathway). Besides valves, the volume change of the brain during sleep may also contribute to that asymmetry. One important model proposed that, because a functional hyperemia cycle includes a rapid dilation and a slow constriction, it may push more CSF into the poroelastic ECS than it pulls back Ravi Teja Kedarasetti et al. 2020. We consider a penetrating artery of length 1000 μ m, a typical length for the mouse brain (Schreder et al. 2022). Owing to the small aspect ratio ε , solving the creeping flow equations numerically is more challenging than solving the thin-film equations (Romanò et al. 2020). More importantly, since p scales with $1/\varepsilon^2$ for creeping flow, a longer

penetrating artery can drive a larger pressure change that pumps the flow.

In our model, a pressure difference between the periarterial space and the perivenous space is the driver for advective flow in the ECS Schreder et al. 2022, which is necessary for our valve mechanism. According to Darcy's Law, the flow speed in the ECS is proportional to the pressure difference $p_{\text{artery}} - p_{\text{venule}}$ and the permeability k_{ecs} , and inversely proportional to the distance b_{ecs} between the periarterial space and the perivenous space. While the distance is constant, and the arterial pump determines the pressure difference, the ECS permeability varies from sleep to wake. From sleep to wakefulness, the porosity of the brain decreases from 0.234 to 0.141, while the tortuosity increases only very slightly, from 1.176 to 1.196. From these values, we estimate a \approx 4.82 times greater ECS permeability during sleep than during wakefulness based on the Kozeny-Carman equation Xie et al. 2013; J. H. Thomas 2019b. The lower ECS permeability during wakefulness creates higher flow resistance, suppressing the entire glymphatic circulation. The ECS is treated as a homogeneous medium in our model. We could incorporate spatial-dependent porosity, toruosity, and permeability, which would be valuable in future modeling to incorporate the inhomogeneities in the ECS Nicholson and Hrabětová 2017. The mechanical properties of the endfeet might also vary between sleep and wakefulness, potentially influencing our model. Future experimental measurements are needed to address this aspect.

The flow rates predicted by our model are broadly consistent with prior values obtained from experiments and simulations. In the cardiac pulsation simulation, we find a mean volume flow rate of order 1000 μ m³/s (for $k_1/k_0 = 2$, $E_{endft} =$

 1×10^5 Pa, figure 4.2e). A mouse has around 320 penetrating arteries branching from the middle cerebral artery (MCA) (Adams et al. 2018), from which we can estimate a total volume flow rate of $320 \times 1000 \mu \text{m}^3/\text{s} = 3.2 \times 10^5 \mu \text{m}^3/\text{s}$ in the PVS of an MCA. An experimental measurement reported a volume flow rate of $\sim 4.5 \times 10^4 \mu \text{m}^3/\text{s}$ for an MCA (K. A. Boster et al. 2023; Ray and Heys 2019). Our simulation thus gives a fairly close prediction, given that some key parameters, such as E_{endft} , k_{endft} , k_{1}/k_{0} , and k_{ecs} , have large uncertainty.

Various experimental studies indicate that the elastic modulus of the endfeet, $E_{\rm endft}$, lies in the range 10^2-10^4 Pa (Greiner et al. 2021; Lu et al. 2006; Messas, Pernot, and Couade 2013; Benveniste et al. 2019). For the softest endfoot wall, the pressure difference across the wall is limited to small values that would not admit any significant through flow with the assumed values of the permeability $k_{\rm endft}$ (Romanò et al. 2020).

The astroglial aquaporin-4 water channels (AQP4) in the endfeet allow faster fluid transport: AQP4 knock-out mice have lower CSF influx Mestre, L. M. Hablitz, et al. 2018. This might be due to an effect of AQP4 on the properties of the endfoot wall. Thus, the range of values of k_{endft} might change, compared to previous estimations, if the role of AQP4 is considered (Koch, Vegard Vinje, and Mardal 2023). It has been suggested that AQP4 might affect the stiffness and flexibility of the endfoot wall (Bork et al. 2023).

The lumped-parameter model reveals what determines the portion of cardiac pulsation and functional hyperemia in pumping the CSF inflow. While the former is 50 times more rapid, the latter is five times larger in amplitude. Both factors

can contribute to a higher inflow rate (figure 4.4e, figure 4.5e,f). The model points out that deformation of the endfoot wall plays a role as a low-pass filter (the compliance) that limits the pumping efficiency of the cardiac pulsation figure 4.4e,f). In the simulations, for $E_{\rm endft} > 10^4$ Pa, cardiac pulsation dominates the inflow (figure 4.5b,c,d), but functional hyperemia gradually becomes a comparable driver as $E_{\rm endff}$ decreases (figure 4.5c). Besides, our model reveal that the phase difference between the artery motion and the flow rate is significant at high frequency domain, and insignificant at low frequency domain. At the ultra low frequency domain (with ultra slow vasomotion ≈ 0.05 Hz), Fultz et al. 2019 observe a correlation between CSF flow up the fourth ventricle and the cerebral blood volume with nearly zero phase difference, which is consistent with our findings. Based on our model, future experiments may observe larger phase difference and smaller pumping efficiency as the frequency of the artery motion increases. Understanding how frequency influences the CSF flow is vital, as it could help us reveal and compare the role of the fast artery pulsation (such as the cardaic pulsation) and the slow vasomotion (such as functional hyperemia) in the glymphatic transport. In addition, Ye et al. 2023 find that glymphatic transport can be mechanically manipulated by ultra sound $(\approx 1 \text{ MHz})$. Understanding how the glymphatic transport is enhanced in such ultra high frequency domain is interesting and important. The numerical solutions of the lumped-parameter model and the fluid-dynamic model match each other very well (figure 4.4e,f). While the fluid-dynamic model resolves the flow spatially and temporally, the lumped parameter model represents a pure time-varying system without spatial resolution and is therefore computationally inexpensive and quite

suitable for vascular network modeling (Jeffrey Tithof et al. 2022).

Another important observation is that although coupling functional hyperemia and cardiac pulsation drives more flow than either mechanism acting alone, it drives less than the superposition of them pumping independently (figure 4.5c). That said, the coupled waveform is more realistic, as functional hyperemia never occurs in the absence of cardiac pulsation. On the other hand, while functional hyperemia happens only occasionally, cardiac pulsation, CSF inflow is consistently observed as a continual process in experiments (Bedussi et al. 2017; Mestre, Kostrikov, et al. 2017; Raghunandan et al. 2018; K. A. Boster et al. 2023; Holstein-Rønsbo et al. 2023). The fact that cardiac pulsation is ~30 times more rapid than functional hyperemia, and occurs all the time, makes it a much stronger driver of CSF flow (figure 4.5b,c,d), at least in the context of our model.

For given values of $k_{\rm ecs}$ and $b_{\rm ecs}$, the flow speed is determined by the pressure gradient driven by the arterial motion. The cardiac pulsation amplitude for a pial artery is usually about 1% of the artery diameter and 0.5% of the PVS width (M. X. Wang et al. 2021). For penetrating arteries, a time-averaged pressure difference of 10 Pa over an axial distance of 1000 μ m can drive a 1 μ m/s net interstitial flow in the ECS. Because flow measurements in the ECS are exceptionally challenging, it has long been debated whether there is any significant flow there. A recent theoretical analysis (J. H. Thomas 2019b) demonstrates that the permeability increase from wake to sleep reduces diffusive transport slightly but would increase advection significantly (due to reduced hydraulic resistance), suggesting that a flow in the ECS might help explain the observed increase in brain clearance from wakefulness

to sleep. Our valve model shows that a flow in the ECS might also be an important part of the mechanism that produces the net flow in the system of perivascular spaces.

It is also important to point out that when there is an influx from the PVS to the ECS there must be a nearly simultaneous efflux somewhere, because the volume of the brain is nearly constant, and the fluid inside (CSF, interstitial fluid) is incompressible. The poroelasticity of the brain might allow a slight time lag between the influx and efflux, but they have to happen on the same time scale.

The predictions of our model are subject to additional caveats. First, we have modeled penetrating PVSs as open spaces, where flow is governed by the Navier-Stokes equation, but they may contain enough tissue that they should be modeled as a porous medium, with flow governed instead by the Darcy equation. Recent imaging of penetrating PVSs suggests this may be the case (Mestre, Verma, et al. 2022), although pial PVSs are known to be open (Min Rivas et al. 2020). In fact, whether penetrating PVSs are porous and what their permeability might be has been identified as the source of greatest uncertainty for brain-wide modeling of glymphatic flows (K. A. S. Boster et al. 2022). That said, other modeling suggests a useful constraint: good perfusion throughout the brain seems to require that the resistance of penetrating PVSs (which is proportional to their permeability) be much greater than that of pial PVSs but much less than that of the ECS (Jeffrey Tithof et al. 2022). Regardless of the permeability of penetrating PVSs, valve action of the sort we suggest here would rectify oscillations and produce a net flow. Whether the potential poroelasticity of the PVSs plays a role in the valve

mechanism will be addressed in further studies.

Second, we have modeled the penetrating PVS as a circular annulus, concentric with the artery, but in vivo measurements show that large eccentricity is common, with the artery positioned against one wall of the PVS (J. Tithof et al. 2019). We expect that accounting for this eccentricity would lead to slightly different predictions. For an open PVS, eccentricity reduces the hydraulic resistance, tending to increase flow and reduce axial pressure gradients. On the side of the artery where the PVS is narrowest, dilation and constriction would cause larger local pressure fluctuations (J. H. Thomas 2019a; Carr et al. 2021) and presumably stronger valve action. On the other side of the artery, however, pressure fluctuations would be smaller and valve action weaker. Future simulations might incorporate eccentric PVSs to explore the effect of these adjustments.

A penetrating artery, along with its PVS, branches into smaller arterioles and smaller PVSs as it goes deeper into the brain tissue. These smaller PVSs likely will not contribute significant pumping because of their high hydraulic resistance, but they are still of interest for future brain-scale vascular network modeling. Jeffrey Tithof et al. 2022 incorporates the hydraulic resistance of PVSs all along the vascular network in a lumped parameter model. Our local lumped-parameter model can be extended to a full vascular network model in the similar way, but with the proposed pumping mechanism included. This approach could also be applied to flow in the lymphatic vessel network, which is driven by artery wall motion and rectified by valves.

Third, we have not considered PVSs around veins in any detail, although they

have been proposed as a route for fluid to leave brain tissue (Iliff, M. Wang, Liao, et al. 2012). If fluid is passing from a higher-pressure ECS to a lower-pressure perivenous space, by the same reasoning discussed above, we would expect the endfoot wall to be compressed, shrinking gaps between endfeet and hindering flow. That is, we would naively expect valve action at the endfoot wall of a perivenous space to promote net flow in the direction opposite to that which has been observed in vivo. The valve mechanism proposed by Bork et al. 2023, if acting at perivenous spaces, would also promote flow in the opposite direction, unless the wedge-shaped edges of endfeet were reversed. However, pulsatility, pressure, and its gradients are much lower in veins (Bohr et al. 2022), so both sorts of valve action may be negligible there. Generally, far less is known about glymphatic efflux than about influx, making it a worthy topic for future studies.

5. Experimental measurements of functional hyperemia and cardiac pulsation, and their impacts on the CSF flow

This chapter presents experimental work and a numerical model of impedance pumping conducted by the author, which has been published in Holstein-Rønsbo et al. 2023 and Gan, Holstein-Rønsbo, et al. 2023. It has been reformatted and edited to fit within the thesis. The thesis author was the second prime author of Holstein-Rønsbo et al. 2023, and the prime author of Gan, Holstein-Rønsbo, et al. 2023. The author did the diameter measurements for both the artery and the PVS, along with the particle velocity velocimetry (PTV) measurements of the CSF flow, and built the model of impedance pumping. Stephanie Holstein-Rønsbo, as the prime author of Holstein-Rønsbo et al. 2023, performed the in-vivo experiments, CSF tracer intensity measurements, and carried out the remaining analysis.

5.1 Background

The experimental exploration of the relationship between cerebrospinal fluid and artery pulsations has been a fascinating and winding journey. In the study by Iliff, M. Wang, Liao, et al. 2012, the visualization of cerebrospinal fluid (CSF) tracer dye along the perivascular network revealed the propagation of the dye from the surface pial perivascular spaces (PVSs) to the PVSs of deep penetrating arteries. This finding confirmed the existence of directional CSF flow. Using the particle tracking velocimetry (PTV), Mestre, J. Tithof, et al. 2018 quantified the mean flow velocity, pulsatility, and Reynolds number of the CSF flow in the PVSs of the surface pial arteries. The study demonstrated a strong correlation between the flow velocity and the cardiac pulsation, indicating that cardiac pulsation is a primary driver of the directed flow. The conclusion was further supported by observations of suppressed flow after injection of hypertension drugs that reduce arterial pulsatility.

In addition to cardiac pulsation, Fultz et al. 2019 demonstrated that slow vasomotion, synchronized with the ultra-slow EEG wave and neural activity, also drives the CSF flow. During natural sleep, CSF influx into the ventricles and the change in blood volume show an anti-correlation, with blood volume change reflecting the vasomotion-induced artery diameter change. However, the study uses fMRI to quantify flow dynamics, which has limitations in time and spatial resolution. It measured the blood-oxygen level dependence (BOLD) to label blood volume change, instead of directly measuring the artery diameter change, which

is challenging. The slow vasomotion driven by neural activity, also known as functional hyperemia, can be manually induced through stimulations. Studies by Veluw et al. 2020 and Williams et al. 2023 demonstrated enhanced clearance rates during functional hyperemia induced by visual stimulations in awake mice. However, simultaneous direct measurement of the slow vasomotion, CSF flow, and potential coupling between them remains a challenge in this field.

This chapter investigates functional hyperemia in mouse brain induced by whisker stimulations, focusing on measuring the artery diameter change waveform, and quantifying the CSF inflow. The stimulations activate functional hyperemia in specific regions in a hemisphere of the anesthetized mouse's brain. By measuring CSF tracer intensity over time, we observe increased CSF influx and clearance rates in the stimulated hemisphere compared to the unstimulated hemisphere. In the pial PVSs, we measure the diameter change waveform and the simultaneous CSF flow dynamics (Holstein-Rønsbo et al. 2023). We find that the artery dilation decreases the width and volume of the PVS, hindering the CSF inflow velocity, whereas the consecutive artery constriction increases PVS width and volume, accelerating the CSF velocity.

Through optical stimulations of local cerebrovasculature, we induced vasoconstriction without activating neural activity and observed increased CSF inflow in the PVSs and increased CSF tracer influx in the stimulated hemisphere. Therefore, we conclude that it is the vasomotion, rather than neural activations, that enhances the CSF inflow.

We suggest that the mechanism of impedance pumping enables both vaso-

Current measurements of the glymphatic system, including artery pulsations and CSF dynamics, are limited to PVSs of the pial arteries (Mestre, J. Tithof, et al. 2018). Measuring the artery diameter change of the penetrating arteries is challenging. Since we can only image the circular cross-section of the penetrating arteries, traditional diameter measurement techniques, such as line scans, become more sensitive to the error in image registration, particularly due to the in-plane shift of the camera, leading to significant variations in diameter measurements as artifacts. Here, we used an algorithm designed to segment the cross-sectional area of penetrating arteries and measure their change over time, which is less sensitive to registration errors. We derived the diameter change over time from the area change measurement.

5.2 Results

5.2.1 Whisker stimulations induce functional hyperemia in mouse's brain, causing an increased CSF influx

We used whisker puffing to stimulate a mouse hemisphere (30 s stimulation periods with 60 s interval, as shown in figure 5.1a). The simulation causes increased neural activity (marked by the Ca²⁺) and cerebral blood flow (marked by hemodynamic signals measured through intrinsic optical imaging (IOS)) in the stimulated hemi-

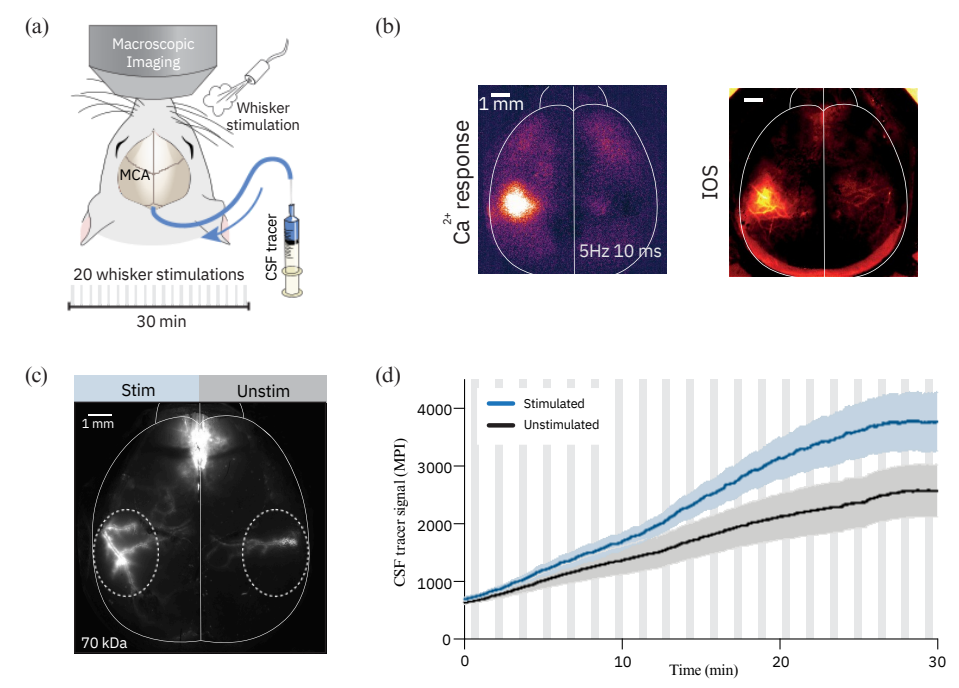


Figure 5.1: Functional hyperemia increases neural activity, cerebral blood flow, and CSF tracer influx in the stimulated hemisphere (a) Adult wild-type mice were stimulated by whisker puffing (30 s each). (b) The whisker stimulations (5 Hz, 10 ms, which means a 5Hz stimulation protocol with 10 ms pulses (190 ms interval)) increase neural activity (marked by Ca²⁺) and cerebral blood flow (marked by hemodynamic signals (IOS)) in the stimulated hemisphere. (c) Representative image of tracer influx around the middle cerebral artery (MCA) (d) Fluorescence signal (MPI) of the tracer influx (n=10 mice). Gray bars show 30 s whisker stimulation. The intensity of the CSF tracers in the stimulated hemisphere increases faster than in the unstimulated hemisphere.

sphere (figure 5.1b). By measuring the CSF tracer intensity, we find increased CSF influx in the stimulated hemisphere (figure 5.1c).

Coupling between the CSF flow velocity and the 5.2.2 vasomotion induced by whisker stimulation

In the previous section, we showed that whisker stimulations induce functional hyperemia, which increases CSF influx. Functional hyperemia is associated with slow vaso-dilation cycles. We further hypothesized that the vaso-dilation is coupled with the CSF flow, and that it is the vaso-dilation that enhances the net flow. We injected tracers to visualize the pial arteries and measure the vaso-dilation waveform (figure 5.2a). We found that whisker stimulation led to an increase in the MCA diameter of 3.3±0.7 µm (resting baseline diameter: 58±3.5 µm, corresponding to 5.7±1% dilation (figure 5.2b)). We injected and tracked illuminated particles to measure the CSF flow of the PVSs of those arteries (figure 5.2c). During arterial dilation, the downstream velocity of the microspheres transiently decreased (from $17.1\pm3.5 \,\mu\text{m/s}$ to $8.8\pm3.2 \,\mu\text{m/s}$, or a decrease of 48.5% (figure 5.2d)), indicating that CSF inflow in the PVSs of the pial arteries is transiently hindered as whisker stimulation expands the arterial diameter. Forward flow rapidly continues as the dilated vessel wall constricts back. The change in downstream velocity peaks (figure 5.2d) appears shortly after the velocity peak of the vessel wall (figure 5.2b), supporting the idea that flow is driven by the artery wall motion. In parallel, as the downstream velocity decreases, the cross-stream velocity increases because microspheres move in the direction of the arterial wall motion (figure 5.2e,f). In general, this demonstrates that dynamic fluctuations in arterial diameter are mirrored by changes in the velocity of perivascular CSF inflow. The pressure exerted by arterial dilation appears to transiently reduce the forward movement of the microspheres while driving an increase in cross-stream velocity.

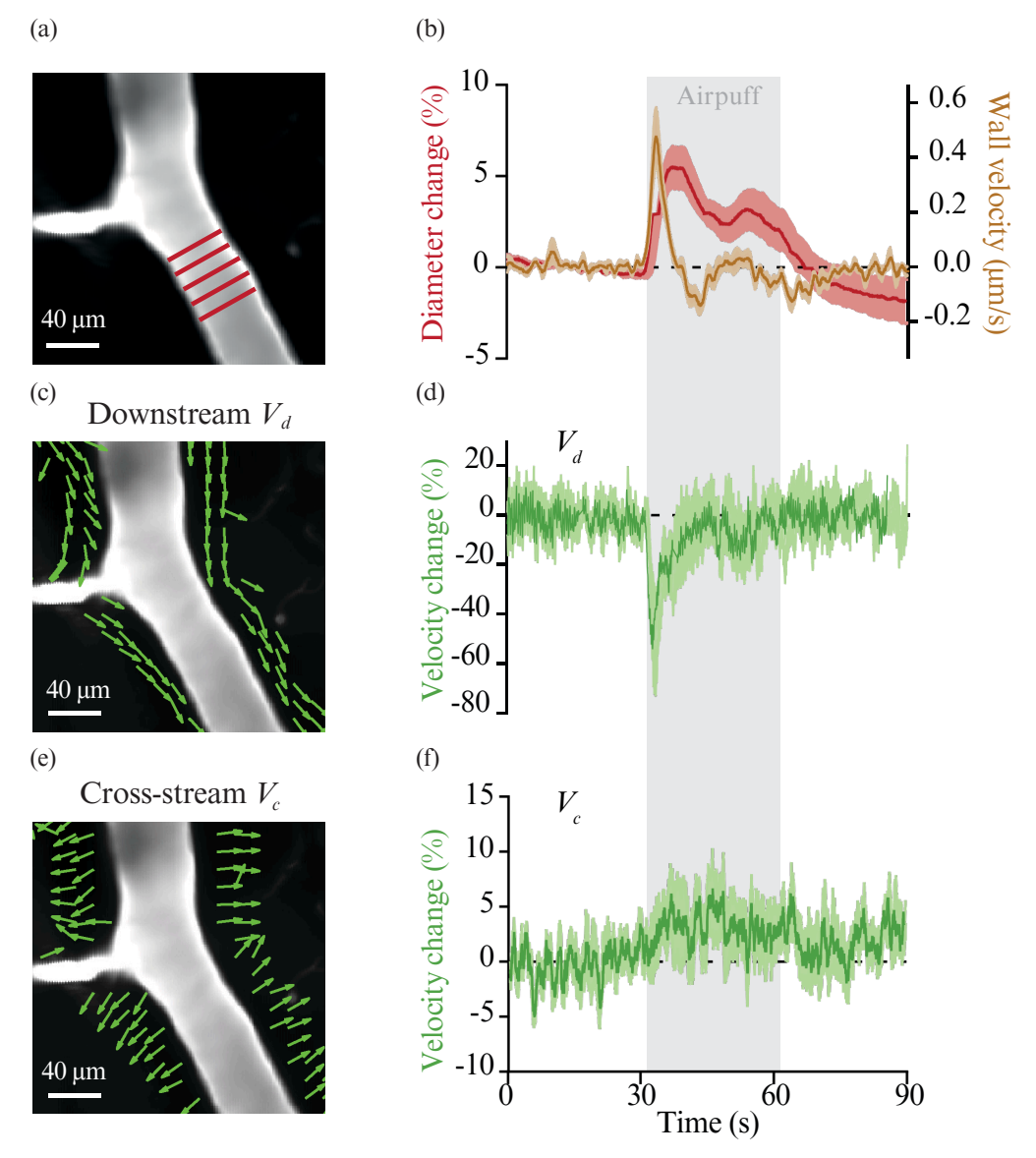


Figure 5.2: Partile tracking velocimetry (PTV) experiments reveal that functional hyperemia causes changes in artery diameter and CSF velocity. (a) Artery diameter changes were measured and averaged across five lines spanning the artery lumen. The artery boundaries were automatically registered based on fluorescence intensity (b) Percentage artery diameter change (red) and vessel wall velocity (brown) during functional hyperemia (n=7). (c) The time-averaged velocity direction field (green arrows) shows net transport in the downstream direction (d) Percentage change of downstream velocity (V_d) during functional hyperemia (n=7). (e) The time-averaged velocity direction field (green arrows) shows the net transport in the cross-stream direction. (f) Percentage change of cross-stream velocity (V_c) during functional hyperemia (n=7).

5.2.3 Coupling between the PVS width and the vasomotion induced by whisker stimulation

We speculated that changes in CSF flow velocity were caused by changes in PVS volume induced by arterial dilation. Through cranial windows, we obtained high-resolution two-photon imaging of the PVSs as they were filled with CSF tracer (cyan in figure 5.3a). In the imaged segments around the pial arteries, the average PVS width was 23.6±2.4 μm before stimulation. As the artery dilates during hyperemia, the width of the PVS decreases by -1.5±0.6 μm (corresponding to -5.9±2%), demonstrating that the change in artery radius directly affects the PVS width (figure 5.3b,c), consistent with a recent report in head-fixed awake and naturally sleeping mice (Bojarskaite et al. 2023). Parallel to arterial dilation, a small outward movement of the outer membrane of the PVS of approximately 1 μm was noted (figure 5.3d).

The measurements of the PVS width change (figure 5.3) and the velocity (figure 5.2) corroborate each other. As the dilating artery decreases the PVS volume, the CSF flow is hindered by the constricted PVS, and therefore the downstream velocity transiently decreases. As the dilated artery constricts back and the PVS volume increases, the CSF flow increases to fill the expanding PVS. It is worth noting that there exists the question whether the flow is driven by some arterial pumping mechanisms, or a naturally existing, constant pressure difference, or both. R. T. Kedarasetti, Drew P., and Costanzo 2020 pointed out that a small constant pressure difference is sufficient to drive the CSF flow of the observed magnitude

in experiment (Mestre, J. Tithof, et al. 2018). However, if the constant pressure is dominant, the flow rate should be inversely proportional to the fourth power of the PVS width (J. H. Thomas 2019a; J. Tithof et al. 2019; White 2006). In other words, the valley of the CSF velocity (figure 5.2d) should be in phase with the peak of the artery diameter (figure 5.2b) instead of being in phase with the wall velocity (figure 5.2b,d). On the other hand, the velocity should be in phase with the wall velocity if the pressure change is driven by the vasodilation cycle itself. Therefore, we can conclude that the constant pressure, if it exists, should not be larger than the pressure oscillation amplitude driven by the vasodilation cycle.

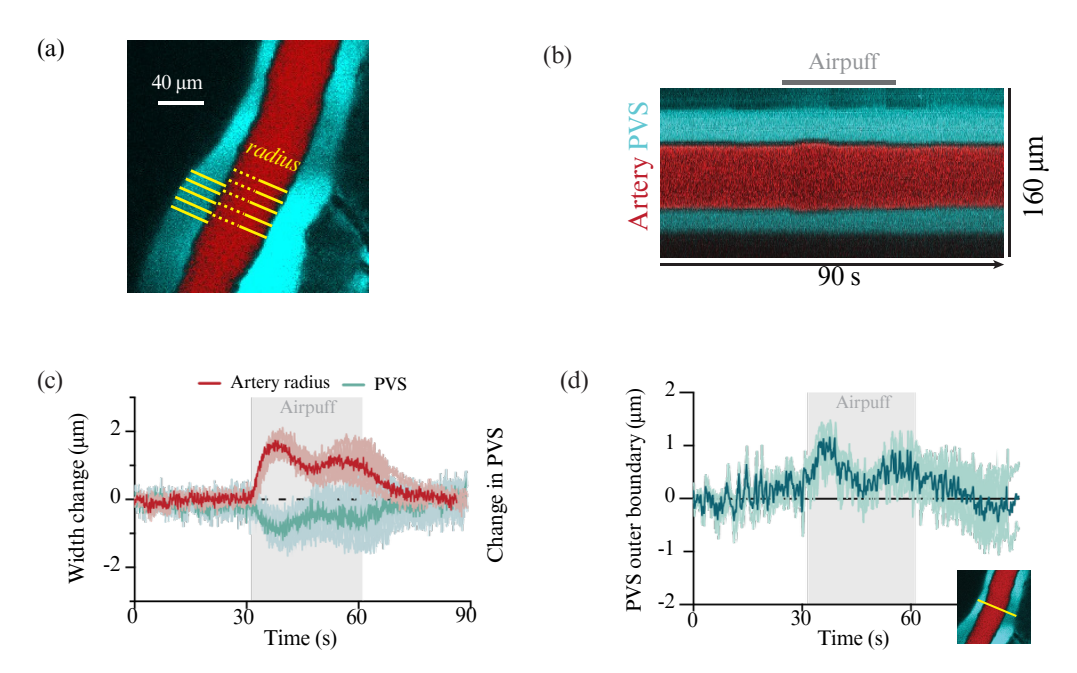


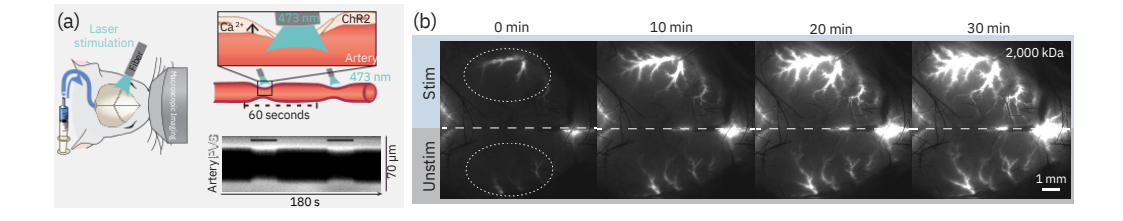
Figure 5.3: Vasodilation cycles cause dynamical change in the width of perivascular space (PVS). **(a)** CSF tracer (3 kDa dextran) was injected into the cisterna magna to visualize the PVS before exposure to unilateral whisker stimulation. Two-photon imaging was used to map width changes of artery and perivascular space. The width changes were averaged across five lines. **(b)** Kymograph of artery and PVS during a 90 s protocol with 30 s stimulation. **(c)** Change of arterial radius and perivascular space width during functional hyperemia (n=6) **(d)**, Movement of the outer PVS wall.

5.2.4 Arterial diameter changes and not neural activation increases CSF inflow

To test the importance of artery diameter change (vaso-motion) as a driver of CSF flow, we used optogenetic mice expressing channelrhodopsin-2 (ChR2) in vascular smooth muscle cells (genetically modified mice whose arteries constrict when exposed to colored light). ChR2-gated cation channels drive an increase in cytosolic Ca²⁺ along with membrane depolarization, which induces arterial constriction, unlike whisker stimulations that induce neural activity and vasodilation. After injection of the CSF tracer, we induced repeated vasoconstrictions of the middle cerebral artery (MCA) by transcranial optogenetic stimulation of the arterial trunk (30 s stimulation periods with 60 s interval, figure 5.4a). The optogenetic stimulation did not allow simultaneous tracer recording, so imaging was restricted to intervals between stimulations. Over the course of the experiment, the tracer signal in the PVS of the MCA exposed to optogenetic stimulation increased faster compared to the unstimulated hemisphere (figure 5.4b), which suggests that it is not the neural activity that drives perivascular CSF inflow, but rather the dynamic changes in arterial diameter. Furthermore, the observations point to the conclusion that it is not specifically the positive (dilation) or negative (constriction) change in diameter but rather vasomotion that propels forward CSF flow along the PVSs. Again, we performed PTV experiments to measure the CSF flow velocity. The vasoconstriction initially caused a transient decrease in CSF flow velocity, likely a consequence of distal microspheres being pulled toward the stimulation site,

101

where vasoconstriction transiently increased PVS volume. However, the CSF flow velocity quickly increased as the artery dilated back, and the overall effect of vasoconstriction was thus an increase in CSF flow velocity (between t= 30–60 s, figure 5.4c).



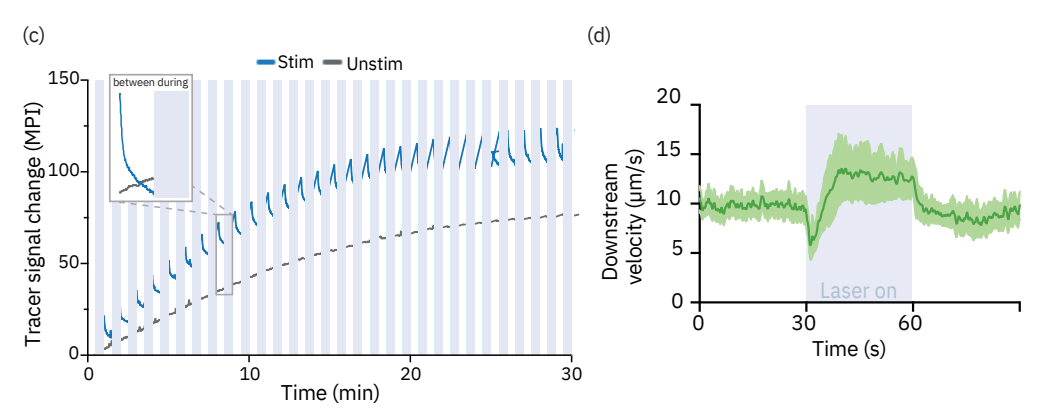


Figure 5.4: Optogenetic stimulations on smooth muscle cells can cause changes in artery diameter (vasoconstriction cycle) in the brains of optogenetic mice without inducing neural activity. (a) Light stimulation increases intra-cellular Ca²⁺ in the smooth muscle cells causing depolarization and vasoconstriction. (b) Representative images of CSF tracer intensity during 30 min circulation. Optogenetic stimulations were given on one hemisphere (30 s stimulation periods with 60 s interval, following a 5Hz stimulation protocol with 10 ms pulses (190 ms interval)). The tracer accumulates faster in the stimulated hemisphere compared to the unstimuated, indicating a higher CSF inflow rate. (c) Representative images of CSF tracer influx during 30 min circulation. (d) Average CSF flow velocity of microspheres in response to optogenetic stimulation (n=5 mice).

5.2.5 Impedance pumping models reproduce flow characteristics

Setting aside, for now, the idea of valves in the glymphatic system, we speculated which valveless pumping mechanism might explain the flow characteristics observed in vivo, particularly the counterintuitive fact that CSF influx is increased both by vasodilation and by vasoconstriction or opposite motions. We found that impedance pumping models reproduce our observations, including the fact that microspheres are transiently pulled toward the site of vasoconstriction. Impedance pumping can occur when a fluid-filled vessel with flexible walls, such as a PVS, is subjected to active, repeating dilation and/or constriction in a local region (Avrahami and Gharib 2008; Hickerson and Morteza Gharib 2006), such as in the embryonic heart, where impedance pumping is important for unidirectional forward flow (Forouhar et al. 2006). Those motions displace fluid locally while also propagating in both directions along elastic vessel walls as waves, which eventually encounter wall features that cause partial or total wave reflection, such as bifurcations, connections to a different fluid chamber or sudden changes in wall stiffness, density or diameter. Primary and reflected waves then interfere constructively or destructively, and if their interference causes a net flow, impedance pumping is said to occur. The flow speed and direction (downstream or upstream) are determined primarily by the wave speed, locations of reflectors, and repetition frequency. Flow direction is not strongly affected by changing dilation to constriction.

We built numerical models of impedance pumping in a simplified PVS (Ap-

pendix B). First, we modeled functional hyperemia induced by whisker stimulation. To do so, we drove periodic dilation of the artery wall near the left side of a simulation domain by applying a periodic force there (figure 5.5a,c). Dilation caused pulsatile CSF flow in the surrounding PVS (figure 5.5b,d). At a cross-section near the left end of the PVS domain, flow proceeded primarily to the left during dilation and to the right when the artery diameter was unperturbed. The flow, however, was not entirely symmetric, and simulated flow tracers moved to the right over time (figure 5.5e). Similarly, the net flux (normalized cumulative volume of CSF moving to the right through the same cross-section) oscillated with each dilation cycle but increased steadily over long times (figure 5.5f).

Next, we modeled vasoconstriction caused by optogenetic stimulation. To do so, we drove periodic constriction of the artery wall (figure 5.5g,i). Constriction, like dilation, caused alternating flow in the surrounding PVS, but with opposite direction—at the same cross-section, flow proceeded primarily to the right during constriction and to the left when the artery diameter was unperturbed (figure 5.5h,j). Nonetheless, tracers again moved to the right over time, and the net flux of CSF again increased steadily (figure 5.5k,l). Future studies should explore whether the valve mechanism and impedance pumping act in concert to orchestrate the unidirectional CSF flow in the periarterial space.

5.2.6 Experimental measurements of penetrating artery motions due to cardiac pulsations and functional hyperemia

Compared to the surface pial arteries, experiments for penetrating arteries and the CSF flow there are limited. Fast line scans provide high temporal resolution (Iliff, M. Wang, Zeppenfeld, et al. 2013; Kress et al. 2014; Bojarskaite et al. 2023) but are sensitive to errors in image registration. A slight shift in the cross-sectional plane, perhaps due to motion artifacts during an experiment, can cause a large variation in the measurement. Here, we present 2-photon measurements of the cross-sectional plane of the penetrating artery.

In the experiments, mice were head-plated and a cranial window was carefully inserted above the middle cerebral artery under ketamine/xylazine anesthesia, before transferring the mice for 2-photon in vivo imaging. Before imaging, an intravascular tracer (0.1 ml FITC-labeled 2,000 kDa dextran, 1%; Sigma-Aldrich, FD2000S) was injected in order to visualize the artery. A penetrating branch of the middle cerebral artery was located and unilateral whisker stimulations Holstein-Rønsbo et al. 2023 were applied to record arterial diameter changes. Imaging was performed just below the cortical surface (at 0 μ m) and 100 μ m deeper. We alternated between the upper and lower depth (5 stimulations each). The imaging was performed at 128 × 128 pixels, 4× zoom, 59 or 113 frames per second.

To measure the area change of the artery over time, we used a custom segmentation code that is insensitive to artifacts of in-plane shifts (figure 5.4d). Since

the cross-section of the penetrating artery is essentially circular, we can calculate an effective diameter $d = 2(A_{\rm artery}/\pi)^{1/2}$, where $A_{\rm artery}$ is the measured area (figure 5.6b,e).

It has been reported that a penetrating artery has pulsatility that increases from the surface to deeper brain regions (Iliff, M. Wang, Zeppenfeld, et al. 2013; Kress et al. 2014). To confirm this, we compared observations at depths 0 μ m and 100 μ m. When observing pulsation due to the cardiac cycle, we applied a bandpass filter in the range 2 Hz to 6 Hz to the diameter signal (figure 5.6b shows 5 seconds of the signal). The pulsation percentage was calculated as the interquartile range of the bandpass diameter signal times $\sqrt{2}$ divided by the mean diameter. From the measurements of eight mice, we observed a mean pulsation percentage around 1% for the 0 μ m deep plane and a mean pulsation percentage of 1.5% for the 100 μ m deep plane (figure 5.6c).

To observe pulsation due to functional hyperemia, we activated neural activity via whisker stimulations (Holstein-Rønsbo et al. 2023). We measured the dilation waveform induced by functional hyperemia in both planes over the 90 s of the recording (figure 5.6e). Over the 30 s stimulation period (from 30 s to 60 s in figure 5.6e), we observed several dilation peaks. By dividing the peak diameter change by the mean diameter of the baseline (from 0 s to 30 s in figure 5.6e), we obtained a pulsation percentage of 6% for the 0 µm deep plane and 11% for the 100 µm deep plane (figure 5.6f). Our experiments thus demonstrate that functional hyperemia induces larger dilation amplitudes in the deep cross-section of the penetrating arteries compared to the surface cross-section.

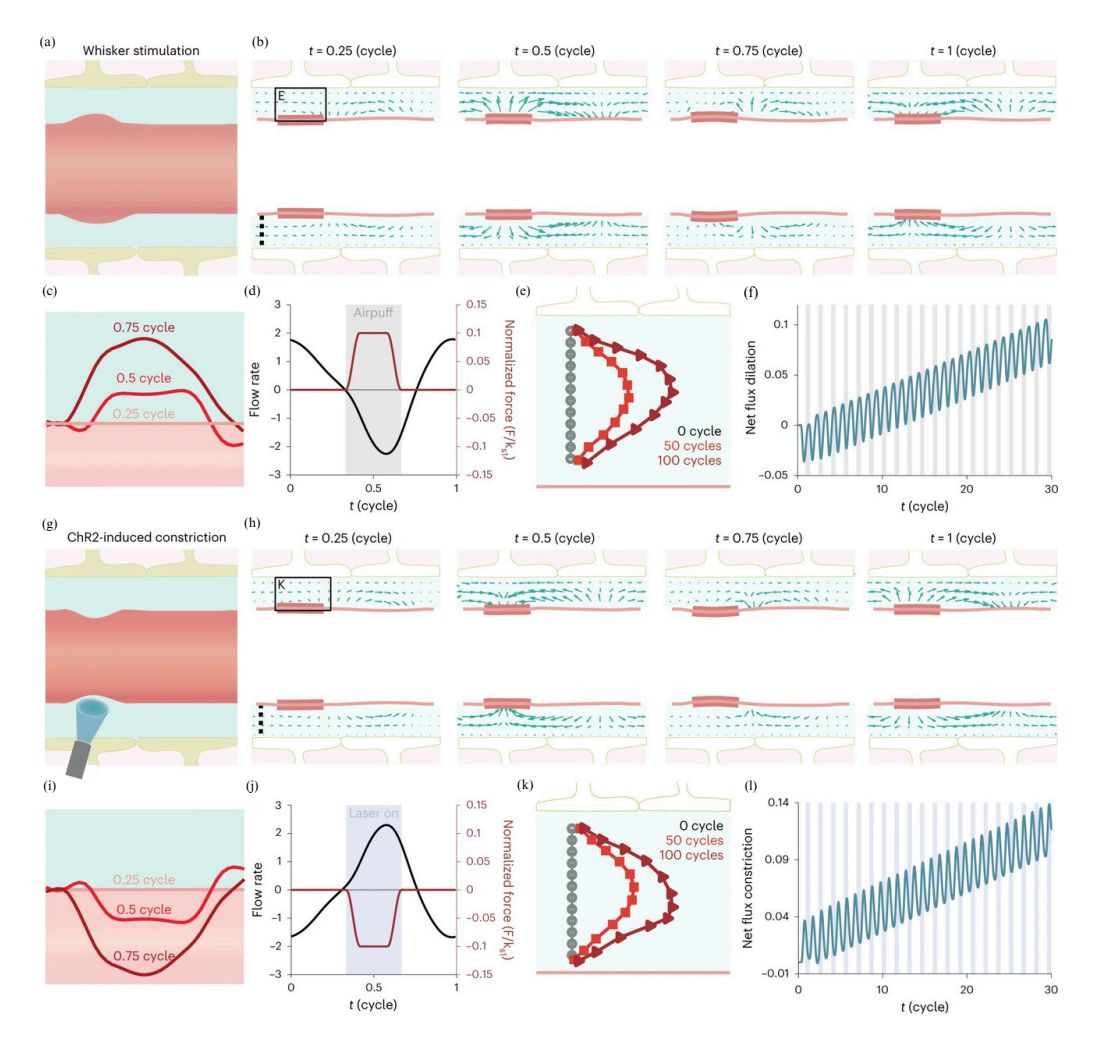


Figure 5.5: Impedance pumping models reproduce characteristics of flows driven by functional hyperemia and optogenetic stimulation. (a) The first model is based on arterial dilation, which we experimentally induced by unilateral whisker stimulation. (b) In the first model, an arteriolar wall (red, shown in cross-section) actively dilates and relaxes in a small region (shaded red), with wall motion spreading in both directions along the artery, causing the flow of CSF (arrows) in the surrounding perivascular spaces. (c) Local wall motion across one dilatory cycle (enlargement of red shaded area in b). (d) The volume flow rate through one cross-section of the perivascular space (dashed line in b) varies over each dilation cycle. Flow is decreased during local dilation, with a slight lag, and increases during local relaxation. (e) Over many cycles, the flow carries passive tracers to the right along the perivascular space (enlargement of region marked in b). (f) The net flux (cumulative volume of fluid moving rightward through the cross-section shown in b) oscillates and increases steadily over time. Gray bars, whisker stimulations. (g) The second model is based on local vasoconstriction, which experimentally is obtained by optogenetic stimulation of mice expressing ChR2 in smooth muscle cells. (h,i) In our second model, the artery constricts instead of dilating, driving a flow with different spatial structures and different volume flow rates. (j-i), In the constriction model, as in the dilation model, tracer moves to the right and net flux increases over time. The direction of the tracer (to the right, not left) is determined by the location of the active arterial diameter change, not by whether it is dilation or constriction. Blue bars, laser stimulations.

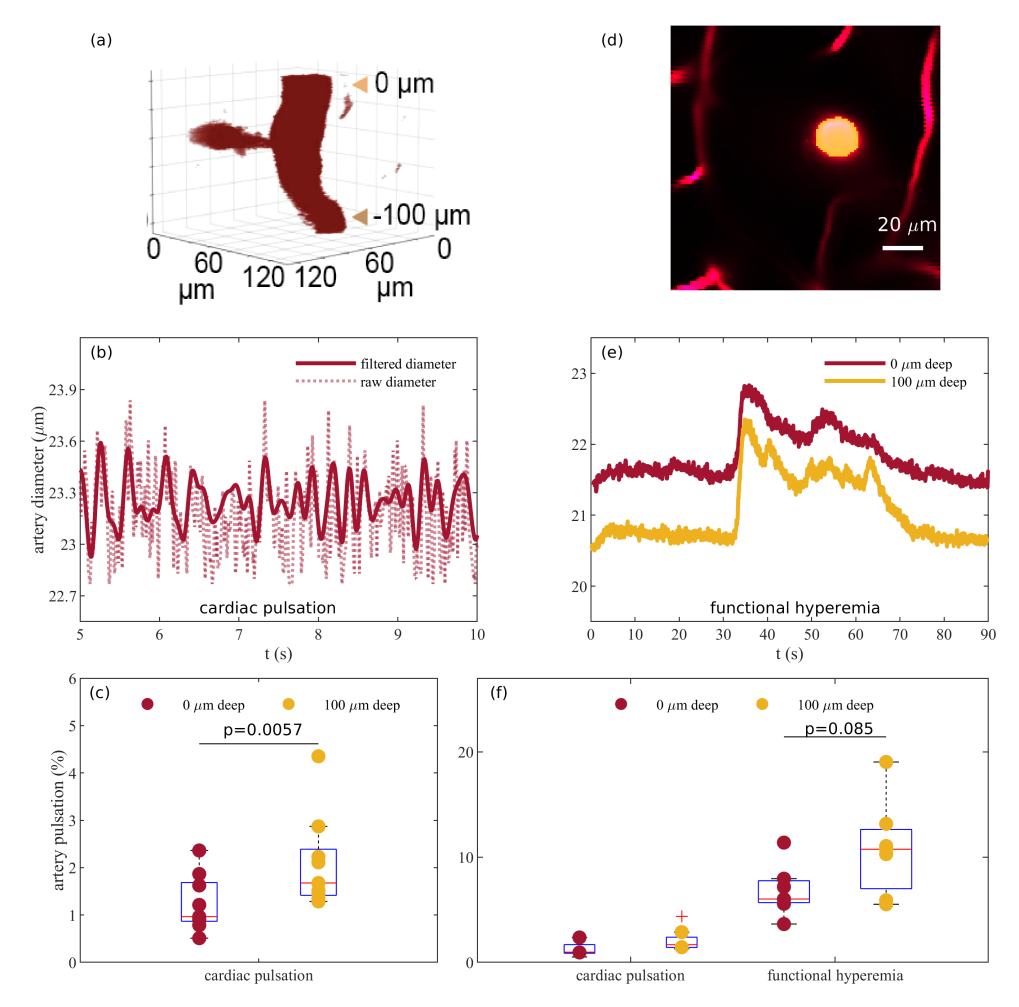


Figure 5.6: Measurements of cardiac pulsation and functional hyperemia in the penetrating arteries. (a) A penetrating artery of a mouse, from depths 0 µm to 100 µm, as imaged in vivo. (b) Artery diameter variation, measured from area changes. (c) Average normalized artery diameter variation in the cardiac frequency band, at depths 0 μ m and 100 μ m, in N=8 mice. Boxes show median and interquartile range. (d) Cross-section of a penetrating artery of a mouse. The shaded yellow mask represents the result of the segmentation algorithm. (e) Artery diameter variation, measured from area changes during functional hyperemia, averaged over N=7 mice. (f) Average normalized artery diameter variation during cardiac pulsation, in N=8 mice, and functional hyperemia, at depths 0 μ m and 100 μ m, in N=7 mice. Functional hyperemia causes greater diameter variations than cardiac pulsation (p $< 10^{-4}$ for an unpaired t-test), and with both mechanisms, there is a trend toward greater diameter variation at greater depths.

5.3 Discussion

The artery diameter variation is an important driver of the directed CSF flow. Mestre, J. Tithof, et al. 2018 demonstrated that the cardiac pulsation pumps the directed flow consistently observed in the anesthesia mice. Although cardiac pulsations have a small amplitude and a long wavelength, which decrease the efficiency of peristaltic pumping, their high frequency can contribute to increased flow rates. However, the compliance of the brain tissue, including astrocytes, may act as a low-pass filter, attenuating high-frequency pumping. On the other hand, functional hyperemia, or neural-vascular coupling, characterized by its large amplitude and slow frequency, may efficiently pump the CSF flow. Spontaneous neural-vascular coupling often occurs during sleep, when CSF flow is active. Therefore, it is crucial to study how functional hyperemia may enhance the CSF flow.

In this chapter, we use whisker stimulation to induce functional hyperemia in the mouse brain, observing an enhanced influx of CSF in the stimulated hemisphere. Simultaneously measuring the diameter change waveform in the pial artery and CSF dynamics in the surrounding PVS reveals a direct coupling between them. Furthermore, through optogenetic stimulation to induce vasoconstriction cycles, we find that vasomotion in the absence of neural activity increases CSF inflow. Hence, we find the vaso-motion a secondary driver of the CSF inflow, in addition to the cardiac pulsation.

Although the optogenetic experiments demonstrate that vaosomotion increases

CSF in the absence of neural activity, they do not exclude the possibility that neural activity itself can increase CSF inflow without inducing vasomotion. As demonstrated by Jiang-Xie et al. 2024, neural activity-induced ionic waves can also drive glymphatic flow through the brain parenchyma, which is independent of vasomotion. It is also worth noting that the vasomotion induced by optogenetic stimulations is usually stronger (faster) than functional hyperemia, which results in a larger change in CSF flow speed.

Our experiments further demonstrate the importance of the artery diameter change in driving the directed CSF inflow, contrary to arguments suggesting that diameter changes cause only oscillatory flow back and forth without driving directed flow. Through manually inducing artery diameter changes (vasomotion) via functional hyperemia or optical stimulation, we see an increased influx of CSF tracers, suggesting that the change in the diameter of the arteries indeed drives a net flow of CSF.

Cardiac pulsation is in the sub-wavelength domain, in which peristaltic pumping cannot drive significant flow. Due to a longer time scale, the wavelength of functional hyperemia is smaller ($\approx 1000 \mu m/s$) compared to cardiac pulsation. In such wavelength domain, peristaltic pumping could be efficient. However, functional hyperemia often propagates in the reversed direction of the CSF flow, traveling from the deep penetrating artery to the surface pial in the mouse brain (Munting et al. 2023). As peristalsis pumps the flow in the same direction as the traveling direction of the pulsation wave, the increased CSF inflow cannot be explained by peristaltic pumping itself. These findings urge further studies of the

arterial pumping mechanism, such as the impedance pumping mechanism and the endfoot valve mechanism we discussed in previous chapters.

The diameter change of the penetrating arteries has not been well measured. We developed a segmentation tool to segment and measure the cross-sectional area of the penetrating arteries over time, based on which the diameter measurement is obtained. Compared to traditional methods, the method provides a more accurate diameter change measurement, as it is less sensitive to translational camera shifts. We measure the diameter change of both cardiac pulsation and functional hyperemia at various depths. Our findings reveal larger diameter change amplitudes in deeper cross-sections of penetrating arteries compared to those at the brain surface. This suggests that the deep penetrating artery could play a more important role in pumping the CSF flow, as a larger diameter change often pumps more fluid.

The increased tracer influx during functional hyperemia (figure 5.1) is unlikely to be attributed solely to the dispersion of the purely oscillatory flow (mixing), as a purely oscillatory flow enhances dispersion only weakly and does not produce significant transport (Troyetsky et al. 2021). Therefore, the increased tracer influx strongly suggests that functional hyperemia drives an increased net flow of CSF, which enhances solute transport more effectively. Although our particle tracking velocimetry (PTV) data captures the transient velocity change during functional hyperemia, this increased flow is not directly observed, probably because PTV can only measure flow velocity in a single focal plane, not the volumetric flow rate. Also, since the flow in the stimulated hemisphere and that in the unstimulated hemisphere cannot be measured simultaneously using PTV, we cannot directly

quantify the flow change for the same animal. New methodologies, such as artificial intelligence velocimetry (K. A. Boster et al. 2023), should be adopted to directly measure the volumetric flow rate during the vaso-dilation cycles of functional hyperemia or other types of vasomotion.

6. Discussion and future work

Arterial pumping is a key driver of the directed cerebrospinal fluid in the perivascular space. In this thesis, I have examined how arterial pumping could produce net flow considering the potential valve action of the astrocyte endfoot. In Chapter 2, I discussed the potential valve mechanism based on the stretching and constriction of the astrocyte endfeet gaps. In Chapter 3, I modeled long slit-shaped endfoot gaps as elliptical gaps to study how the aspect ratio and orientations of the gap influenced the potential valve mechanism. In Chapter 4, I demonstrated that the valve mechanism can explain how the arterial diameter change pumps the directed CSF flow in the pial artery in the same direction as the blood flow. In Chapter 5, I presented experimental work that shows that slow vasomotion, including functional hyperemia, enhances CSF inflow.

The driving mechanism of cerebrospinal fluid flow is not single-handed. In addition to the valve mechanism we proposed here, valveless pumping mechanisms, such as peristaltic pumping (Carr et al. 2021) and impedance pumping (Hickerson and Morteza Gharib 2006), may also explain how artery pulsations produce the net flow of CSF. In addition to arterial pumping, the osmotic force created by the

concentration difference of solutes can produce a steady pressure gradient that drives CSF net flow. In this chapter, we will explore the characteristics of each mechanism, hoping to inspire future research in this field.

6.1 Valve Mechanism

Candidates for valve actions include stretching and constriction of the endfoot gaps (Gan, Holstein-Rønsbo, et al. 2023), bending of wedge-shape endfeet (Bork et al. 2023), and deformation of the poroelastic brain tissue (Ravi Teja Kedarasetti et al. 2020). Some valve candidates may be more effective at rectifying the flow than others, but there is a limitation.

For a given pressure waveform, the pumping efficiency is maximum when the flow is rectified by an ideal valve, which blocks all backflow and only permits inflow. For a binary alternating pressure waveform that is symmetric in time (figure 6.1a). The maximum pumping efficiency is $\eta \approx 0.71$ or $1/\sqrt{2}$ (T⁺/T = 0.5, where T⁺ is the duration of the positive pressure and T is the total duration of the waveform, (figure 6.1b, red dot)). For a sinusoidal pressure waveform, the maximum pumping efficiency is 0.58.

The realistic pressure waveforms of the arterial pulsations are not symmetric in time. Figure 6.1b shows that pumping efficiency increases with $T^+/T=0.8$. For example, when $T^+/T=0.8$, the maximum pumping efficiency is $\eta\approx 1.41$ or $\sqrt{2}$ (blue dot). The same conclusion applies to any other asymmetric waveforms that are not binary. If the duration of the positive pressure covers the entire period

 $(T^+/T\approx 1)$, the alternating pressure waveform becomes a steady constant positive pressure waveform, which drives a steady flow with a pumping efficiency of $\eta=\infty$. A positive pressure in the PVS drives an inflow into the ECS but results in an axial backflow in the PVS, whereas a negative pressure drives a backflow across the gaps and an axial CSF inflow (as demonstrated in the perivascular pumping model in Gan, Holstein-Rønsbo, et al. 2023). Therefore, an asymmetric pressure waveform, with a shorter duration of positive pressure and a longer duration of negative pressure, could generate an axial CSF flow in the PVS with higher pumping efficiency, aligning more closely with experimental observations. The arterial diameter change waveform during functional hyperemia, characterized by a fast dilation and slow constriction, can generate such an asymmetric pressure waveform in the PVS and a higher pumping efficiency, whereas the symmetric cardiac pulsation cannot.

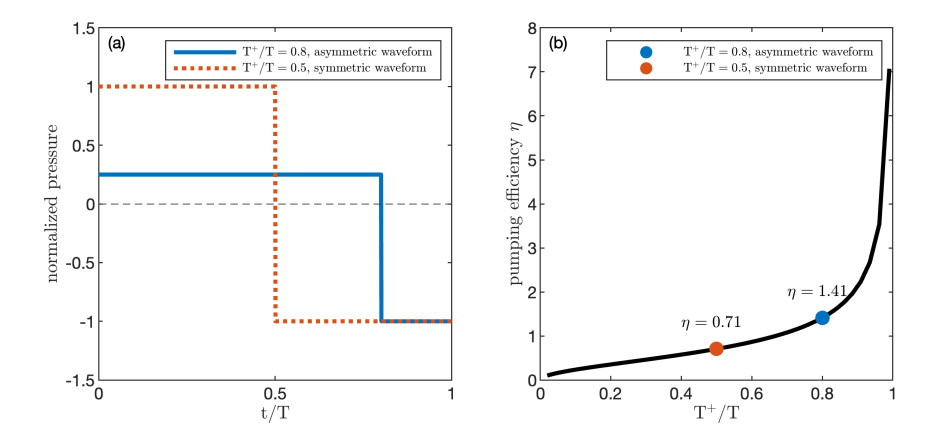


Figure 6.1: When rectified by ideal valves, asymmetric pressure waveforms with a longer duration of positive pressure (T^+) , result in a higher pumping efficiency compared to the symmetric pressure waveform. T represents the period of the waveform. (a) A symmetric binary alternating pressure waveform and an asymmetric binary alternating pressure waveform normalized to the maximum pressure amplitude. In the asymmetric waveform, the positive pressure amplitude is smaller than the negative pressure amplitude to maintain a zero average pressure. (b) As T^+/T increases, the maximum pumping efficiency increases

6.2 Valveless pumping

6.2.1 Peristaltic pumping

Peristalsis generally drives a pulsatile flow with both an oscillatory component and a steady component in the direction of the traveling pulsation wave in the artery wall. Multiple models have predicted steady flow components with similar magnitudes to those observed in vivo but usually accompanied by a much stronger oscillatory component than is observed (Hadaczek et al. 2006; Douglas H. Kelley and John H. Thomas 2023). The ratio of the fluctuating flow rate and the mean flow rate is approximately 1000, while in vivo measurement of that ratio is at the order of 1. The discrepancy can be resolved by applying proper boundary conditions that account for the resistance and compliance of the entire CSF circulation system

(Ladrón-de-Guevara et al. 2022).

Additionally, the wavelength of cardiac pulsations (≈ 1 m), is far greater than the length of a PVS segment ($\approx 200~\mu m$), and the diameter change amplitude is $\approx 1\%$. With such a short wavelength and small diameter change amplitude, the peristaltic pumping cannot drive a flow of the observed magnitude ($\approx 20~\mu m/s$, Daversin-Catty et al. 2020).

In contrast to cardiac pulsation, Gjerde, Rognes, and Sanchez 2023 demonstrates that the peristaltic wave of slow vasomotion, including functional hyperemia, which has a much smaller wavelength ($\approx 1000~\mu m$) and larger diameter change amplitude ($\approx 10\%$) can induce a non-negligible net perivascular fluid flow at the order of some $\mu m/s$ in the perivascular networks. The model neglects the reflections of peristaltic waves at the arterial bifurcations. However, the wave of vasomotion does not always travel in the same direction as the CSF flow Munting et al. 2023; Yao et al. 2019. As peristaltic pumping cannot explain how vasomotion drives a flow in its reverse travelling direction, other mechanisms must be considered, such as the valve mechanism considered by this thesis, the poroelasticity considered by Ravi Teja Kedarasetti et al. 2020, and impedance pumping considered by Holstein-Rønsbo et al. 2023. It is also necessary to note that, since the CSF flow in PVSs has been observed even in the absence of vasomotion (Mestre, J. Tithof, et al. 2018), the peristalsis of vasomotion is unlikely to be the only driving mechanism.

6.2.2 Impedance Pumping

Impedance pumping can occur when a vessel, such as PVS, with a flexible wall, such as the artery wall, is subjected to repeating dilation and/or constriction cycles in a local region (Hickerson and Morteza Gharib 2006). Those artery wall motions propagate in both directions along elastic vessel walls as waves, which eventually encounter wall features that cause wave reflection, such as bifurcations or sudden changes in wall stiffness. Primary and reflected waves then interfere constructively or destructively, which can drive a net flow. The flow speed and direction (downstream or upstream) are determined primarily by the wave speed, the locations of the reflectors, and the repetition frequency (Avrahami and Gharib 2008). Since wave reflection is non-linear, a small amplitude of artery pulsation can drive a significant amount of flow. Flow direction is not strongly affected by changing dilation to constriction. Impedance pumping may, in part, explain how cardiac pulsation, functional hyperemia, and vaso-constrictions cycles induced by opto-stimulations drive the directed CSF flow (Holstein-Rønsbo et al. 2023).

It is important to model arterial wave reflection in the perivascular network with physiological parameters. Wave reflection may occur at bifurcations of the PVSs and cause impedance pumping. Additionally, pulsatility in a penetrating artery increases from the surface to deeper brain regions (Iliff, M. Wang, Zeppenfeld, et al. 2013; Kress et al. 2014; Gan, Holstein-Rønsbo, et al. 2023), indicating that the arterial section at the surface is stiffer than that in deeper brain regions (Mestre, J. Tithof, et al. 2018). This stiffness change could also cause wave reflection and impedance pumping.

Impedance pumping drives maximum net flow when the arterial segment pulses at its harmonic frequency (Zislin and Rosenfeld 2018; Avrahami and Gharib 2008; Hickerson and Morteza Gharib 2006). The wave speed of an artery is $c = \sqrt{Eh/\rho r_0} \approx 1$ m/s, where $E \approx 10^5$ Pa is the Young's modulus of the artery, $\rho \approx 1000 \text{ kg/m}^3$ is the estimated density of the artery (or the CSF&Blood fluid phase), and $h/r_0 \approx 10$ is the ratio between the thickness of the artery wall and the radius of the artery. The harmonic frequency is therefore $f = c/2L \approx 2500 \; \mathrm{Hz}$ (Olufsen et al. 2000; Zislin and Rosenfeld 2018), where $L \approx 200 \,\mu m$ is a typical length of a PVS segment. If reflection occurs on the length scale of the entire PVS network (≈ 2 mm, K. A. S. Boster et al. 2022), the harmonic frequency is $f \approx 250$ Hz. These harmonic frequencies are much higher than the frequency of cardiac pulsation ($f \approx 5$ Hz), the frequency of vasomotion (≈ 0.1 Hz), or other physiological frequencies. However, stimulations at higher frequencies can enhance CSF influx, which may be related to the mechanism of impedance pumping at the harmonic frequencies. Murdock et al. 2024; Chan et al. 2022 find that multi-sensory gamma stimulations at $f \approx 40$ Hz promote the influx of cerebrospinal fluid, the efflux of interstitial fluid, and glymphatic clearance of amyloid. Ye et al. 2023 demonstrated that stimulations at ultrasound frequency increase glymphatic net flow ($f \approx 10^5$ Hz). Investigating whether stimulations at the harmonic frequency of the glymphatic network can significantly enhance CSF net flow is a promising direction for future research.

6.3 The osmotic force

The osmotic force, created by the concentration difference of solutes, could generate a steady pressure gradient that drives CSF flow. During stroke, the spread of depolarization creates a strong concentration gradient across the extracellular space (ECS), causing a pressure gradient that pumps significant CSF flow (Mukherjee, Mirzaee, and Jeffrey Tithof 2023). Injecting hyperosmotic solutes into mouse's arteries enhances CSF inflow during sleep, sleep-like state and wakefulness (Plog and M. Nedergaard 2018).

The production of CSF also, in part, depends on regulated ion transport that generates osmotic gradients and water transport. The transcellular movement of Na⁺ is primarily driven by the Na⁺/K⁺-ATPase expressed at the luminal membrane facing the CSF. The movement of Na⁺ is accompanied by water that follows the solute gradient (Wichmann, Damkier, and Pedersen 2022). The production of CSF may also create a steady pressure gradient, driving the directed CSF flow.

Characterizing the role of osmotic force in driving CSF flow is crucial not only for understanding the glymphatic system but also for advancing drug delivery techniques for brain diseases. Traditional drug delivery relies on blood circulation; However, due to the blood-brain barrier, drugs carried by blood flow cannot be delivered into the brain parenchyma efficiently, whereas drug delivery is much easier through the glymphatic pathway. Hyperosmotic solutes that enhance glymphatic flow could accelerate drug delivery via the glymphatic pathway, which is important for treating brain diseases.

6.4 Modeling advection and diffusion in the glymphatic network

Solute transport in the brain is accomplished by a combination of advection and diffusion. Solving solute transport based on the CSF flow information helps reveal the processes of brain waste removal, drug delivery, and tracer (dye) injection (figure 6.2a,b, Holstein-Rønsbo et al. 2023) in the glymphatic network, which includes perivascular spaces with bifurcations and the parenchyma. It can also help interpret CSF tracer measurements in the PVSs of the penetrating arteries and MRI measurements in the parenchyma (Y. Zhu et al. 2023). The basic equation governing the concentration C of a solute is the advection-diffusion equation.

$$\frac{\partial C}{\partial t} + u \cdot \nabla C = D\nabla^2 C + f, \tag{6.1}$$

where *u* is the local CSF/ISF flow velocity, D is the local diffusion coefficient, and f is the local source term (the rate of generation of the solute per unit volume per unit time). Based on a reduced order network model that solves the CSF flow field numerically (figure 6.2c, Jeffrey Tithof et al. 2022), the process of time-dependent solute transport (equation 6.1) can be implemented and solved. The author of the thesis and his colleague, Keelin Quirk, are working on building such a solver. Some examples of the spatially and temporarily resolved tracer concentration are presented in figure 6.2d. Due to artery motion, the pulsatility of CSF flow increases, which may also slightly enhance solute influx and clearance (mixing, Troyetsky

et al. 2021). Having functional hyperemia acting over cardiac pulsation increases flow pulsatility, which may also promote waste clearance in the aspect of mixing. Incorporating pulsatile flow profiles into the model can help us better understand the role of mixing in solute transport and clearance in the brain.

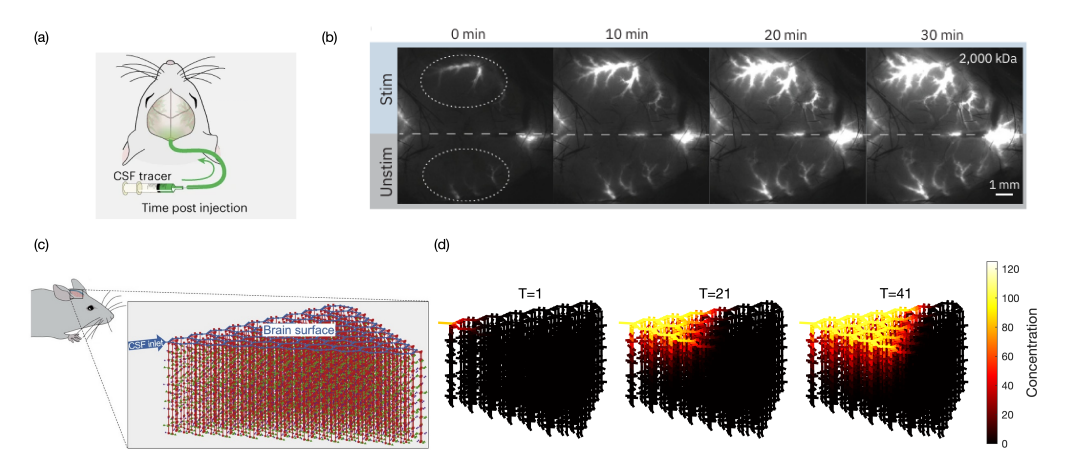


Figure 6.2: Solute transport in the brain. Panel (a),(b) adapted from Holstein-Rønsbo et al. 2023, copyright the authors. Panel (c) adapted from Jeffrey Tithof et al. 2022, copyright the authors. CSF tracers injected into the mouse brain (a) are transported in the glymphatic network by a combination of advection and diffusion (b). (c) The CSF flow of the glymphatic network, including PVSs with bifurcations and the parenchyma has been modeled numerically (K. A. S. Boster et al. 2022), based on which we are building a solver to model time-dependent solute transport. By setting a concentration value of 100 at the inlet pial artery's PVS and a concentration value of 0 at the outlets of the network, we calculate and present spatially-resolved tracer concentration at three instants (d).

6.4.1 Estimating the amplitude of the pressure difference driven by functional hyperemia

Although K. A. Boster et al. 2023 measured the pressure difference between the inlet and outlet of a PVS segment using artificial intelligence velocimetry, this approach has not yet been applied to assess the pressure driven by functional hyperemia. In this section, I attempt to estimate this pressure difference based on

the flow velocity measurement during functional hyperemia (figure 5.2) in Chapter 5.

We divide the pressure difference between two ends of the PVS into two parts

$$\Delta p(t) = \Delta \overline{p} + \Delta \tilde{p}(t), \tag{6.2}$$

where $\Delta \overline{p}$ is a steady pressure difference component, and $\Delta \tilde{p}$ is the transient pressure difference component driven by the artery motion.

The flow rate can be represented in the same way:

$$Q(t) = \frac{\Delta p(t)}{R(t)} = \frac{\Delta \overline{p}}{R(t)} + \frac{\Delta \tilde{p}(t)}{R(t)} = \overline{Q}(t) + \tilde{Q}(t), \tag{6.3}$$

where R(t) is the flow resistance of the local PVS segment, which also changes transiently with the diameter change (inversely proportional to the fourth power of the PVS diameter). If $\Delta \overline{p} \gg \Delta \widetilde{p}(t)$, that the flow rate is dominated by the steady pressure, and the PVSs do not connect with any high resistance pathway, we have $Q(t) \approx \overline{Q}(t)$, which scales as $r^4(t)$, where r(t) is the artery radius. The flow rate change should theoretically be in phase with the changes in artery diameter. However, experiments show that the mean flow velocity is actually in phase with the wall velocity, rather than the changes in diameter (Holstein-Rønsbo et al. 2023). Given that wall velocity should be in phase with the transient pressure, the transient pressure difference caused by artery motion is at least as significant as any steady pressure difference that may exist.

According to the lumped parameter model (figure 4.4), the phase of the transient

pressure driven by artery motion should align perfectly with the wall velocity when the brain is rigid. However, as the arterial pumping frequency exceeds the cutoff frequency, determined by the compliance of the brain tissue and the resistance of the flow pathway, a phase shift occurs. At the frequency of slow vasomotion, our experiments indicate that the peak of the wall velocity and the trough of the flow velocity are almost perfectly in phase Holstein-Rønsbo et al. 2023. At the frequency of cardiac pulsation, the phase difference is more pronounced (Mestre, J. Tithof, et al. 2018).

Based on the discussion above, the change in flow resistance of PVSs due to the change in the diameter of the arteries can be neglected, allowing equation 6.3 can be simplified to

$$Q(t) = \frac{\Delta p(t)}{R} = \frac{\Delta \overline{p}}{R} + \frac{\Delta \tilde{p}(t)}{R} = \overline{Q} + \tilde{Q}(t), \tag{6.4}$$

Using equation 6.4, we can estimate the ratio between the magnitude of the steady pressure difference and the magnitude of the transient pressure difference. During functional hyperemia, a 60% change in flow velocity is recorded compared to the baseline velocity (Holstein-Rønsbo et al. 2023). $1 + \max{(\tilde{Q}(t)/\bar{Q})} = 1 + \max{(\Delta \tilde{p}(t)/\Delta \bar{p})} = 0.6$, which yields $\max{|\Delta \tilde{p}(t)/\Delta \bar{p}|} = 2.5$. That is, between two ends of a pial PVS segment, the transient pressure difference driven by the functional hyperemia component is 2.5 times greater than the steady pressure difference component, smaller than the ratio of oscillatory-to-net pressure of cardiac pulsation (a ratio of 3.3), measured from artificial intelligence velocimetry

(K. A. Boster et al. 2023). Since artificial intelligence velocimetry reveals the steady axial pressure difference per unit length of a PVS segment 2.75×10^2 Pa/m, we can estimate that the maximum pressure difference amplitude driven by functional hyperemia is 6.88×10^2 Pa/m. In future work, artificial intelligence velocimetry method could be extended to measure the pressure waveform driven by functional hyperemia.

Bibliography

- Adams, Matthew D et al. (2018). "The pial vasculature of the mouse develops according to a sensory-independent program". In: Scientific reports 8.1, p. 9860.
- Aldea, R. et al. (2019). "Cerebrovascular smooth muscle cells as the drivers of intramural periarterial drainage of the brain". In: Front. Aging Neurosci. 11.
- Alnaes, M. S. et al. (2015). "The FEniCS Project Version 1.5". In: <u>Archive of Numerical Software</u> 3. DOI: 10.11588/ans.2015.100.20553.
- Avrahami, I and M Gharib (July 2008). "Computational studies of resonance wave pumping in compliant tubes". In: J. Fluid Mech. 608, pp. 205–22.
- Basser, P. J. (1992). "Interstitial pressure, volume, and flow during infusion into brain tissue". In: Microvasc. Res. 44.2, pp. 143–165.
- Battista, Nicholas A, Austin J Baird, and Laura A Miller (2015). "A mathematical model and MATLAB code for muscle–fluid–structure simulations". In: Integrative and comparative biology 55.5, pp. 901–911.
- Battista, Nicholas A, W Christopher Strickland, and Laura A Miller (2017). "IB2d: a Python and MATLAB implementation of the immersed boundary method". In: Bioinspiration & biomimetics 12.3, p. 036003.
- Bedussi, B. et al. (Oct. 2017). "Paravascular spaces at the brain surface: Low resistance pathways for cerebrospinal fluid flow". In: <u>Journal of Cerebral Blood Flow & Metabolism</u>, pp. 0271678X1773798–8.
- Benveniste, Helene et al. (2019). "The glymphatic system and waste clearance with brain aging: a review". In: Gerontology 65.2, pp. 106–119.
- Bohr, Tomas et al. (2022). "The glymphatic system: Current understanding and modeling". In: iScience 25.9, p. 104987.
- Bojarskaite, Laura et al. (2023). "Sleep cycle-dependent vascular dynamics in male mice and the predicted effects on perivascular cerebrospinal fluid flow and solute transport". In: Nature Communications 14.1, p. 953.

Bork, P. A. R. et al. (2023). "Astrocyte endfeet may theoretically act as valves to convert pressure oscillations to glymphatic flow". In: <u>Journal of The Royal Society Interface</u> 20. DOI: 10.1098/rsif.2023.0050.

- Boster, K. A. S. et al. (2022). "Sensitivity analysis on a network model of glymphatic flow". In: <u>Journal of The Royal Society Interface</u> 19.191, p. 20220257. DOI: 10.1098/rsif.2022.0257.eprint: https://royalsocietypublishing.org/doi/pdf/10.1098/rsif.2022.0257. URL: https://royalsocietypublishing.org/doi/abs/10.1098/rsif.2022.0257.
- Boster, Kimberly AS et al. (2023). "Artificial intelligence velocimetry reveals in vivo flow rates, pressure gradients, and shear stresses in murine perivascular flows". In: Proceedings of the National Academy of Sciences 120.14, e2217744120.
- Carr, J. B. et al. (2021). "Peristaltic pumping in thin non-axisymmetric annular tubes". In: J. Fluid Mech. 917.A10.
- Chan, Diane et al. (2022). "Gamma frequency sensory stimulation in mild probable Alzheimer's dementia patients: Results of feasibility and pilot studies". In: PloS one 17.12, e0278412.
- Chourdakis, G et al. (2022). "preCICE v2: A sustainable and user-friendly coupling library [version 2; peer review: 2 approved]". In: Open Research Europe 2.51. DOI: 10.12688/openreseurope.14445.2. URL: https://doi.org/10.12688/openreseurope.14445.2.
- Daversin-Catty, C. et al. (Dec. 2020). "The mechanisms behind perivascular fluid flow". In: <u>PLOS ONE</u> 15.12, pp. 1–20. DOI: 10.1371/journal.pone.0244442. URL: https://doi.org/10.1371/journal.pone.0244442.
- Diem, A. K. et al. (Aug. 2017). "Arterial Pulsations cannot Drive Intramural Periarterial Drainage: Significance for A β Drainage". In: Front Neurosci 11, pp. 353–9.
- Forouhar, Arian S et al. (2006). "The embryonic vertebrate heart tube is a dynamic suction pump". In: Science 312.5774, pp. 751–753.
- Fultz, N E et al. (2019). "Coupled electrophysiological, hemodynamic, and cerebrospinal fluid oscillations in human sleep". In: Science 366, pp. 628–631.
- Gan, Yiming, Stephanie Holstein-Rønsbo, et al. (2023). "Perivascular pumping of cerebrospinal fluid in the brain with a valve mechanism". In: <u>Journal of the Royal Society Interface</u> 20.206, p. 20230288.
- Gan, Yiming, John H Thomas, and Douglas H Kelley (2024). "Gaps in the wall of a perivascular space act as valves to produce a directed flow of cerebrospinal fluid: a hoop-stress model". In: <u>Journal of the Royal Society Interface</u> 21.213, p. 20230659.

Gjerde, Ingeborg G, Marie E Rognes, and Antonio L Sanchez (2023). "The directional flow generated by peristalsis in perivascular networks—Theoretical and numerical reduced-order descriptions". In: Journal of Applied Physics 134.17.

- Greiner, Alexander et al. (2021). "Poro-viscoelastic effects during biomechanical testing of human brain tissue". In: <u>Frontiers in Mechanical Engineering</u> 7, p. 708350.
- Hablitz, L. M. et al. (2019). "Increased glymphatic influx is correlated with high EEG delta power and low heart rate in mice under anesthesia". In: Science Advances 5.2, eaav5447. DOI: 10.1126/sciadv.aav5447. eprint: https://www.science.org/doi/pdf/10.1126/sciadv.aav5447. URL: https://www.science.org/doi/abs/10.1126/sciadv.aav5447.
- Hadaczek, P. et al. (June 2006). "The "Perivascular Pump" Driven by Arterial Pulsation Is a Powerful Mechanism for the Distribution of Therapeutic Molecules within the Brain". In: Mol Ther 14.1, pp. 69–78.
- Hickerson, Anna Iwaniec and Morteza Gharib (2006). "On the resonance of a pliant tube as a mechanism for valveless pumping". In: <u>Journal of Fluid Mechanics</u> 555, pp. 141–148.
- Holstein-Rønsbo, Stephanie et al. (2023). "Glymphatic influx and clearance are accelerated by neurovascular coupling". In: Nature Neuroscience, pp. 1–12.
- Holter, K. E. et al. (2017). "Interstitial solute transport in 3D reconstructed neuropil occurs by diffusion rather than bulk flow". In: PNAS 114.37, pp. 9894–9899.
- Iliff, JJ, M Wang, Y Liao, et al. (Aug. 2012). "A Paravascular Pathway Facilitates CSF Flow Through the Brain Parenchyma and the Clearance of Interstitial Solutes, Including Amyloid β ". In: Sci Transl Med 4.147, 147ra111.
- Iliff, JJ, M Wang, DM Zeppenfeld, et al. (Nov. 2013). "Cerebral arterial pulsation drives paravascular CSF-interstitial fluid exchange in the murine brain". In: J Neurosci 33.46, pp. 18190–18199.
- Jiang-Xie, Li-Feng et al. (2024). "Neuronal dynamics direct cerebrospinal fluid perfusion and brain clearance". In: <u>Nature</u> 627.8002, pp. 157–164.
- Kedarasetti, R. T., P. J. Drew, and F. Costanzo (2022). "Arterial vasodilation drives convective fluid flow in the brain: a poroelastic model". In: Fluids and Barriers of the CNS 19 (1), p. 34. ISSN: 2045-8118. DOI: 10.1186/s12987-022-00326-y. URL: https://doi.org/10.1186/s12987-022-00326-y.
- Kedarasetti, R. T., T. Drew P., and F. Costanzo (2020). "Arterial pulsations drive oscillatory flow of CSF but not directional pumping". In: <u>Sci. Rep.</u> 10.1.
- Kedarasetti, Ravi Teja et al. (2020). "Functional hyperemia drives fluid exchange in the paravascular space". In: Fluids and Barriers of the CNS 17.1, pp. 1–25.

Kelley, Douglas H. and John H. Thomas (2023). "Cerebrospinal Fluid Flow". In: Annual Review of Fluid Mechanics 55.1, null. DOI: 10.1146/annurev-fluid-120720-011638. eprint: https://doi.org/10.1146/annurev-fluid-120720-011638. URL: https://doi.org/10.1146/annurev-fluid-120720-011638.

- Koch, Timo, Vegard Vinje, and Kent-André Mardal (2023). "Estimates of the permeability of extra-cellular pathways through the astrocyte endfoot sheath". In: Fluids and Barriers of the CNS 20.1, p. 20.
- Kress, BT et al. (2014). "Impairment of paravascular clearance pathways in the aging brain". In: Ann Neurol 76.6, pp. 845–861.
- Ladrón-de-Guevara, Antonio et al. (2022). "Perivascular pumping in the mouse brain: Improved boundary conditions reconcile theory, simulation, and experiment". In: Journal of Theoretical Biology 542, p. 111103.
- Lei, GH, Charles WW Ng, and Douglas B Rigby (2001). "Stress and displacement around an elastic artificial rectangular hole". In: <u>Journal of Engineering Mechanics</u> 127.9, pp. 880–890.
- Lu, Yun-Bi et al. (2006). "Viscoelastic properties of individual glial cells and neurons in the CNS". In: <u>Proceedings of the National Academy of Sciences</u> 103.47, pp. 17759–17764.
- Markert, Bernd (2005). <u>Porous media viscoelasticity with application to polymeric foams</u>. Mathiisen, Thomas Misje et al. (Mar. 2010). "The perivascular astroglial sheath provides a complete covering of the brain microvessels: An electron microscopic
- Messas, E., M. Pernot, and M. Couade (2013). "Arterial wall elasticity: State of the art and future prospects". In: <u>Diagnostic and Interventional Imaging</u> 94.5. Ultrasound elastography, pp. 561–569. ISSN: 2211-5684. DOI: https://doi.org/10.1016/j.diii.2013.01.025. URL: https://www.sciencedirect.com/science/article/pii/S2211568413000338.

3D reconstruction". In: Glia 58.9, pp. 1094–1103.

- Mestre, H., L. M. Hablitz, et al. (2018). "Aquaporin-4-dependent glymphatic solute transport in the rodent brain". In: eLife 7, e40070.
- Mestre, H., S. Kostrikov, et al. (Aug. 2017). "Perivascular spaces, glymphatic dysfunction, and small vessel disease". In: Clinical Science 131.17, pp. 2257–2274. ISSN: 0143-5221. DOI: 10.1042/CS20160381. eprint: https://portlandpress.com/clinsci/article-pdf/131/17/2257/445646/cs-2016-0381c.pdf. URL: https://doi.org/10.1042/CS20160381.
- Mestre, H., J. Tithof, et al. (2018). "Flow of cerebrospinal fluid is driven by arterial pulsations and is reduced in hypertension". In: Nat Commun 9.1, p. 4878.

Mestre, H., N. Verma, et al. (2022). "Periarteriolar spaces modulate cerebrospinal fluid transport into brain and demonstrate altered morphology in aging and AlzheimerÕs disease". In: Nature Communications 13 (1), p. 3897. ISSN: 2041-1723. DOI: 10.1038/s41467-022-31257-9. URL: https://doi.org/10.1038/s41467-022-31257-9.

- Min Rivas, F. et al. (2020). "Surface periarterial spaces of the mouse brain are open, not porous". In: <u>Journal of The Royal Society Interface</u> 17.172, p. 20200593. DOI: 10.1098/rsif.2020.0593. eprint: https://royalsocietypublishing.org/doi/pdf/10.1098/rsif.2020.0593. URL: https://royalsocietypublishing.org/doi/abs/10.1098/rsif.2020.0593.
- Mukherjee, Saikat, Mahsa Mirzaee, and Jeffrey Tithof (2023). "Quantifying the relationship between spreading depolarization and perivascular cerebrospinal fluid flow". In: Scientific reports 13.1, p. 12405.
- Munting, Leon P et al. (2023). "Spontaneous vasomotion propagates along pial arterioles in the awake mouse brain like stimulus-evoked vascular reactivity". In: Journal of Cerebral Blood Flow & Metabolism, p. 0271678X231152550.
- Murdock, Mitchell H et al. (2024). "Multisensory gamma stimulation promotes glymphatic clearance of amyloid". In: <u>Nature</u> 627.8002, pp. 149–156.
- Murthy, MV Vedavyasa (1969). "Stresses around an elliptic hole in a cylindrical shell". In.
- Nedergaard, Maiken and Steven A. Goldman (2020). "Glymphatic failure as a final common pathway to dementia". In: Science 370.6512, pp. 50–56.
- Neeves, K.B. et al. (2006). "Fabrication and characterization of microfluidic probes for convection enhanced drug delivery". In: <u>Journal of Controlled Release</u> 111.3, pp. 252–262. ISSN: 0168-3659. DOI: https://doi.org/10.1016/j.jconrel.2005.11.018. URL: https://www.sciencedirect.com/science/article/pii/S0168365905006899.
- Nicholson, C and S Hrabětová (Nov. 2017). "Brain extracellular epace: the final frontier of neuroscience". In: Biophys J 113, pp. 1–10.
- Olufsen, Mette S et al. (2000). "Numerical simulation and experimental validation of blood flow in arteries with structured-tree outflow conditions". In: Annals of biomedical engineering 28, pp. 1281–1299.
- Penn, R. D. and A. Linninger (2009). "The physics of hydrocephalus". In: <u>Pediatr. Neurosurg.</u> 45.3, pp. 161–174.
- Plog, B. A. and M. Nedergaard (2018). "The glymphatic system in central nervous system health and disease: past, present, and future". In: <u>Annu Rev Pathol-Mech</u> 13, pp. 379–394.

Pollard, David D (1973). "Equations for stress and displacement fields around pressurized elliptical holes in elastic solids". In: <u>Journal of the International Association for Mathematical 6</u>5, pp. 11–25.

- Raghunandan, A. et al. (2018). "Bulk flow of cerebrospinal fluid observed in periarterial spaces is not an artifact of injection". In: eLife 10, e65958.
- Ray, L. A. and J. J. Heys (2019). "Fluid flow and mass transport in brain tissue". In: Fluids 4.4, p. 196.
- Romanò, Francesco et al. (2020). "Peristaltic flow in the glymphatic system". In: Scientific Reports 10.1, pp. 1–17.
- Roylance, David (2001). "Pressure vessels". In: <u>Department of Materials Science and Engineering, Massac Savin, G No, AS Kosmodamianskii, and AN Guz (1967).</u> "Stress concentrations near holes". In: Soviet Applied Mechanics 3.10, pp. 16–26.
- Schreder, H. E. et al. (2022). "A hydraulic resistance model for interstitial fluid flow in the brain". In: <u>Journal of The Royal Society Interface</u> 19.186, p. 20210812. DOI: 10.1098/rsif.2021.0812. eprint: https://royalsocietypublishing.org/doi/pdf/10.1098/rsif.2021.0812. URL: https://royalsocietypublishing.org/doi/abs/10.1098/rsif.2021.0812.
- Scroggs, M. W., I. A. Baratta, et al. (2022). "Basix: a runtime finite element basis evaluation library". In: <u>Journal of Open Source Software</u> 7.73, p. 3982. DOI: 10.21105/joss.03982.
- Scroggs, M. W., J. S. Dokken, et al. (2022). "Construction of arbitrary order finite element degree-of-freedom maps on polygonal and polyhedral cell meshes". In: <u>ACM Transactions on Mathematical Software</u> 48.2, 18:1–18:23. DOI: 10.1145/3524456.
- Smith, Joshua H. and Joseph A.C. Humphrey (2007). "Interstitial transport and transvascular fluid exchange during infusion into brain and tumor tissue". In: Microvascular Research 73.1, pp. 58–73. ISSN: 0026-2862. DOI: https://doi.org/10.1016/j.mvr.2006.07.001. URL: https://www.sciencedirect.com/science/article/pii/S0026286206000896.
- Thomas, J. H. (Apr. 2019a). "Fluid dynamics of cerebrospinal fluid flow in perivascular spaces". In: Journal of the Royal Society Interface 16.1, pp. 52–57.
- (2019b). "Theoretical analysis of wake/sleep changes in brain solute transport suggest a flow of interstitial fluid". In: Fluids Barriers CNS 19.30.
- Tithof, J. et al. (2019). "Hydraulic resistance of periarterial spaces in the brain". In: Fluids Barriers CNS 16.19.
- Tithof, Jeffrey et al. (2022). "A network model of glymphatic flow under different experimentally-motivated parametric scenarios". In: iScience 25.5, p. 104258.

Troyetsky, D. E. et al. (2021). "Dispersion as a waste-clearance mechanism in flow through penetrating perivascular spaces in the brain". In: Sci. Rep. 11, p. 4595.

- Van Dyke, Peter (1965). "Stresses about a circular hole in a cylindrical shell". In: AIAA Journal 3.9, pp. 1733–1742.
- Veluw, S. J. van et al. (2020). "Vasomotion as a driving force for paravascular clearance in the awake mouse brain". In: Neuron 105.3, pp. 549–561.
- Vinje, V. et al. (2020). "Intracranial pressure elevation alters CSF clearance pathways". In: Fluids Barriers CNS 17.1, pp. 1–19.
- Wang, M. X. et al. (2021). "Varying perivascular astroglial endfoot dimensions along the vascular tree maintain perivascular-interstitial flux through the cortical mantle". In: Glia 69, pp. 715–728. DOI: 10.1002/glia.23923.
- Wang, P. and W. L. Olbricht (Apr. 2011). "Fluid mechanics in the perivascular space". In: J Theor Biol 274.1, pp. 52–57.
- Weller, Henry G et al. (1998). "A tensorial approach to computational continuum mechanics using object-oriented techniques". In: <u>Computers in physics</u> 12.6, pp. 620–631.
- White, F. M. (2006). Viscous Fluid Flow 3rd ed. 3rd. New York: McGraw-Hill.
- Wichmann, Thea Overgaard, Helle Hasager Damkier, and Michael Pedersen (2022). "A brief overview of the cerebrospinal fluid system and its implications for brain and spinal cord diseases". In: Frontiers in human neuroscience 15, p. 737217.
- Williams, Stephanie D et al. (2023). "Neural activity induced by sensory stimulation can drive large-scale cerebrospinal fluid flow during wakefulness in humans". In: PLoS biology 21.3, e3002035.
- Xie, L. et al. (2013). "Sleep drives metabolite clearance from the adult brain". In: Science 342.6156, pp. 373–377.
- Yao, Jinxia et al. (2019). "Cerebral circulation time derived from fMRI signals in large blood vessels". In: Journal of Magnetic Resonance Imaging 50.5, pp. 1504–1513.
- Ye, Dezhuang et al. (2023). "Mechanically manipulating glymphatic transport by ultrasound combined with microbubbles". In: <u>Proceedings of the National Academy of Sciences</u> 120.21, e2212933120.
- Zhu, Yuran et al. (2023). "Transport pathways and kinetics of cerebrospinal fluid tracers in mouse brain observed by dynamic contrast-enhanced MRI". In: Scientific Reports 13.1, p. 13882.
- Zislin, Victor and Moshe Rosenfeld (2018). "Impedance pumping and resonance in a multi-vessel system". In: Bioengineering 5.3, p. 63.

A. Mathematical details of the perivascular pumping models

The section includes mathematical details of the perivascular pumping models in Chapter 4. It has been published in Gan, Holstein-Rønsbo, et al. 2023

The lubrication-theory model

The PVS domain

The PVS is an open space, and the flow there, assumed to be axisymmetric, obeys the Navier-Stokes equations and continuity equation in cylindrical coordinates (r,z):

$$\frac{\partial u}{\partial t} + u \frac{\partial u}{\partial r} + w \frac{\partial u}{\partial z} = -\frac{1}{\rho} \frac{\partial p}{\partial r} + \frac{\mu}{\rho} \left(\frac{1}{r} \frac{\partial u}{\partial r} + \frac{\partial^2 u}{\partial r^2} + \frac{\partial^2 u}{\partial z^2} \right), \tag{A.1}$$

$$\frac{\partial w}{\partial t} + u \frac{\partial w}{\partial r} + w \frac{\partial w}{\partial z} = -\frac{1}{\rho} \frac{\partial p}{\partial z} + \frac{\mu}{\rho} \left(\frac{1}{r} \frac{\partial w}{\partial r} + \frac{\partial^2 w}{\partial r^2} + \frac{\partial^2 w}{\partial z^2} \right), \tag{A.2}$$

$$\frac{1}{r}\frac{\partial(ru)}{\partial r} + \frac{\partial w}{\partial z} = 0, (A.3)$$

where $\mathbf{u} = (u, w)$ is the velocity field in cylindrical coordinates, p is the pressure, t is time, ρ is the density of the fluid, and μ is the dynamic viscosity. These equations are subject to the following boundary conditions:

$$z = 0$$
: $q_{\text{pvs}} = q_{\text{pial}}, \ q_{\text{pial}} = k_{\text{pial}}(p_{\text{pial}} - p), \ p_{\text{pial}} = 0,$ (A.4)

$$z = l$$
: $q_{pvs} = q_{cap}$, $q_{cap} = k_{cap}(p - p_{cap})$, $p_{cap} = 0$, (A.5)

$$r = r_1 + h$$
: $\mathbf{u} \cdot \mathbf{n} = 0$, $\mathbf{u} \cdot \mathbf{t} = 0$, (A.6)

$$r = r_1 + b + d$$
: $\mathbf{u} \cdot \mathbf{n} = \frac{\partial d}{\partial t} + k_{\text{endft}}(p - p_{\text{ecs}}), \ \mathbf{u} \cdot \mathbf{t} = 0,$ (A.7)

where

$$d = (r_1 + b)\frac{p - p_{\text{ecs}}}{E_{\text{endft}}} \tag{A.8}$$

is the deformation of the PVS outer wall (measured from $d_0 = r_1 + b$). Here, r_1 is the radius of the artery at rest, b is the width of the PVS, l is the length of the penetrating artery, h is the amplitude of artery pulsation, $E_{\rm endft}$ is the Young's modulus of the PVS outer boundary, $q_{\rm pvs}$ is the flow rate at the end of the penetrating artery PVS, $q_{\rm pial}$ is the flow rate in the pial PVS, $q_{\rm cap}$ is the flow rate in the precapillary PVS, $k_{\rm pial}$ and $k_{\rm cap}$ are the conductivities of the pial and precapillary inlet and outlet, and finally, $p_{\rm pial}$ and $p_{\rm cap}$ are the pressure in the pial and precapillary PVS (set to zero). The unit vectors normal and tangential to the artery wall are $\mathbf{n} = (0,1)$ and $\mathbf{t} = (1,0)$, respectively. We have used the lubrication approximation Romano et al. 2020.

At the upstream pial PVS and the downstream precapillary PVS, we set a hydraulic resistance boundary condition to model the inflow and outflow (equations (A.4), (A.5)), assuming a conserved flow rate across each interface. At the artery wall, we set non-slip and non-permeable boundary conditions (equation (A.6)). The outer boundary of the PVS, formed by the astrocyte endfeet, is modeled as a thin, deformable, elastic layer of permeable but non-slip tissue (equation (A.7)). A linear elastic law is used to relate the deformation of this boundary to the pressure difference across it (Romanò et al. 2020).

The artery motion of cardiac pulsation is modeled by equation (4.2). The artery motion of functional hyperemia is modeled by equation (4.3), where h_0 is the amplitude and f is the frequency. This waveform ensures that h and dh/dt are continuous (see figure 4.1e).

At the valve-like PVS outer boundary, formed by astrocyte endfeet, the permeability $k_{\rm endft}$ is modeled by equation (4.1). During artery dilation, the increased pressure in the PVS opens the valve, allowing fluid to enter the ECS (figure 4.1b). During artery constriction, the valve closes and CSF motion is confined to the PVS (figure 4.1c).

To put the equations in nondimensional form, we use the scalings

$$r = bR$$
, $z = lZ$, $t = \frac{T}{f}$, $u = bfU$, $w = lfW$, $p = \frac{\mu f}{\varepsilon^2} P$, (A.9)

where each uppercase symbol signifies a dimensionless version of the correspond-

ing lowercase symbol. Applying the lubrication theory, we obtain the following equations:

$$\frac{\partial P_0}{\partial T} + A_0 \frac{\partial^2 P_0}{\partial Z^2} + A_1 \frac{\partial P_0}{\partial Z} + A_2 P_0 = \left[\frac{E(R_1 + H)}{R_1 + 1 + D_0} \right] \frac{\partial H}{\partial T} + A_2 P_{\text{ECS}} + \frac{\partial P_{\text{ECS}}}{\partial T},$$
(A.10)

$$W_0 = \frac{R^2}{4} \frac{\partial P_0}{\partial Z} + C_1 \ln(R) + C_2, \tag{A.11}$$

$$U_0 = \frac{C_3}{R} - \frac{R^3}{16} \frac{\partial^2 P_0}{\partial Z^2} - \frac{R}{4} \left[2 \ln(R) - 1 \right] \frac{\partial C_1}{\partial Z} - \frac{R}{2} \frac{\partial C_2}{\partial Z}, \tag{A.12}$$

where P_0 , W_0 , and U_0 are the leading order terms of P, W, and U, respectively. A_0 , A_1 , A_2 , C_1 , C_2 , and C_3 are known functions of Z and T. These equations are solved numerically using the Chebyshev spectral method (Romanò et al. 2020).

Integrating the axial velocity (equation A.11) over the cross-section of the annulus, we obtain an expression for the volume flow rate:

$$Q_{0}(Z,T) = \int_{0}^{2\pi} \int_{R_{1}+H}^{1+R_{1}+D} W_{0}R dR d\theta$$

$$= 2\pi \left[\frac{R^{4}}{16} \frac{\partial P_{0}}{\partial Z} + C_{1} \left(\frac{R^{2} \ln(R)}{2} - \frac{R^{2}}{4}\right) + \frac{C_{2}R^{2}}{2}\right]_{R=R_{1}+H}^{R=1+R_{1}+D} (A.13)$$

We model a hydraulic resistance at the PVS of the pial boundary, with a conserved flow rate across the interface:

$$Z = 0$$
: $Q_0(0,T) = Q_{\text{pial}}, \ Q_{\text{pial}} = K_{\text{pial}}(0 - P_0(0,T)).$ (A.14)

In the same way, we model a hydraulic resistance at the PVS of the capillary site:

$$Z = 1$$
: $Q_0(1,T) = Q_{cap}$, $Q_{cap} = K_{cap}(P_0(1,T) - 0)$. (A.15)

At the artery site, we have

$$R = R_1 + H : \mathbf{U} \cdot \mathbf{n} = \frac{\partial H}{\partial T}, \mathbf{U} \cdot \mathbf{t} = 0,$$
 (A.16)

where H is the amplitude of artery pulsation. At the PVS outer boundary we have

$$R = R_1 + 1 + D$$
: $\mathbf{U} \cdot \mathbf{n} = \frac{\partial D}{\partial T} + K_{\text{endft}} (P_0(Z, T) - P_{\text{ECS}}), \quad \mathbf{U} \cdot \mathbf{t} = 0,$ (A.17)

where

$$D = \frac{P_0(Z, T) - P_{ECS}}{F},$$
 (A.18)

135

is the (dimensionless) displacement of the PVS outer boundary, $K_{\text{endft}} = k_{\text{endft}} \mu(b\epsilon^2)^{-1}$, and $E = E_{\text{endft}} \epsilon^2 (\mu f(R_1 + 1))^{-1}$.

The ECS domain

The ECS is modeled as an incompressible porous medium, with incompressible flow governed by Darcy's law. The governing equations are

$$\mathbf{u}_{\text{ecs}}^* = -\frac{k_{\text{ecs}}}{\mu} \nabla p_{\text{ecs}}, \quad \mathbf{u}_{\text{ecs}}^* = \mathbf{u}_{\text{ecs}} - \frac{\partial \mathbf{d}_{\text{ecs}}}{\partial t}, \tag{A.19}$$

$$\nabla \cdot (\phi \mathbf{u}_{\text{ecs}} + (1 - \phi) \frac{\partial \mathbf{d}_{ecs}}{\partial t}) = 0, \quad \nabla \cdot \mathbf{d}_{\text{ecs}} = 0,$$
 (A.20)

where $\mathbf{u}_{\text{ecs}} = (u_{\text{ecs}}, w_{\text{ecs}})$ is the velocity of the fluid phase in the ECS, ϕ is the porosity, \mathbf{d}_{ecs} is the deformation of the solid phase in the ECS, $\mathbf{u}_{\text{ecs}}^*$ is the velocity field relative to the solid phase velocity, and p is the pressure inside the ECS. The dynamic viscosity μ of the CSF and the permeability k_{ecs} of the ECS are both assumed to be uniform. Applying all four of the above equations, we have

$$\nabla^2 p_{\rm ecs} = 0. \tag{A.21}$$

Across the PVS outer boundary, CSF enters or leaves the ECS from the PVS, and the velocity must be continuous there:

$$r = r_1 + b : u_{\text{ecs}}^* = u^*,$$
 (A.22)

where $u^* = k_{\text{endft}}(p - p_{\text{ecs}})$ is the velocity across the PVS endfoot wall measured relative to the deformation velocity of the endfoot wall.

For the boundary at the outer radius of the ECS, corresponding to efflux at the nearest venule, we assume free surfaces and require

$$r = r_1 + b + b_{\text{ecs}} : p = 0.$$
 (A.23)

For the boundaries at the two ends, we assume zero axial pressure gradient:

$$z = 0, z = 1: \frac{\partial p_{\text{ecs}}}{\partial z} = 0.$$
 (A.24)

U	axial CSF velocity	$U = \frac{u}{bf}$
W	radial CSF velocity	$W = \frac{f_W}{\varepsilon b}$ $R = \frac{r}{b}$
R	radial coordinate	$R = \frac{r}{b}$
Z	axial coordinate	$Z = \varepsilon \frac{z}{b}$
T	time	T = ft
R_{ECS}	axial coordinate for the ECS	$R_{\mathrm{ECS}} = \frac{r}{b_{\mathrm{ecs}}}$
P	pressure in the PVS	$P = \frac{p\varepsilon^2}{\mu f}$ $Re = \frac{\varepsilon \rho f b^2}{\mu}$ $Q = \frac{q}{b^2 l f} = \varepsilon \frac{q}{b^3 f}$
Re	Reynolds number	$Re = rac{arepsilon ho f b^2}{\mu}$
Q	axial flow rate	$Q = \frac{q}{b^2 l f} = \varepsilon \frac{q}{b^3 f}$
R_1	artery diameter	$R_1 = \frac{r_1}{b}$
D	displacement of the PVS outer boundary	$D = \frac{d}{b}$
$A_{ m PVS}$	PVS cross-section area	$R_1 = \frac{r_1}{b}$ $R_2 = \frac{l}{b}$ $A_{PVS} = \frac{a_{pvs}}{b^2}$ $\varepsilon = \frac{b}{l}$ $H = \frac{h}{b}$
$oldsymbol{arepsilon}$	aspect ratio of the PVS	$arepsilon = rac{b}{l}$
H	artery dilation amplitude	$H = \frac{h}{b}$
E	elasticity of the PVS outer boundary	$E = \frac{E_{\text{endft}} \varepsilon^2}{\mu f(R_1 + 1)}$
K_{endft}	permeability of the PVS outer boundary	$K_{\mathrm{endft}} = \frac{\mu k_{\mathrm{endft}}}{b \varepsilon^2}$
K_{pial}	conductivity of the pial pvs inlet	$K_{\text{endft}} = \frac{\mu k_{\text{endft}}}{b\varepsilon^2}$ $K_{\text{pial}} = \frac{k_{\text{pial}}}{b^2 \frac{b}{\varepsilon} f} \cdot \frac{\mu f}{\varepsilon^2}$
$K_{\rm cap}$	conductivity of the capillary pvs outlet	$K_{\rm cap} = \frac{k_{\rm cap}}{b^2 \frac{b}{\varepsilon} f} \cdot \frac{\mu f}{\varepsilon^2}$
$K_{\rm recs}$	permeability of the ECS	$K_{ m recs} = rac{k_{ m ecs}}{b_{ m ecs}^2 arepsilon^2}$
$K_{\rm zecs}$	permeability of the ECS	$K_{\mathrm{zecs}} = \frac{k_{\mathrm{ecs}}}{l^2 \varepsilon^2}$
$P_{\rm ecs}$	pressure in the ECS	$P_{ m ecs} = rac{p_{ m ecs} arepsilon^2}{\mu f}$
$U_{ m ecs}$	radial velocity in the ECS	$U_{\mathrm{ecs}} = \frac{u_{\mathrm{ecs}}}{b_{\mathrm{ecs}}f}$
$W_{\rm ecs}$	radial velocity in the ECS	$W_{\rm ecs} = \frac{w_{\rm ecs}}{lf}$
$U_{ m ecs}$	radial velocity in the ECS	$U_{\mathrm{ecs}} = \frac{u_{\mathrm{ecs}}}{b_{\mathrm{ecs}}f}$
U^*	radial velocity relative to the endfoot wall motion	$K_{\text{zecs}} = \frac{k_{\text{ecs}}}{l^2 \varepsilon^2}$ $K_{\text{zecs}} = \frac{k_{\text{ecs}}}{l^2 \varepsilon^2}$ $P_{\text{ecs}} = \frac{p_{\text{ecs}} \varepsilon^2}{\mu f}$ $U_{\text{ecs}} = \frac{u_{\text{ecs}}}{b_{\text{ecs}} f}$ $W_{\text{ecs}} = \frac{w_{\text{ecs}}}{l f}$ $U_{\text{ecs}} = \frac{u_{\text{ecs}}}{b_{\text{ecs}} f}$ $U^* = \frac{u - \frac{\partial d}{\partial t}}{b f}$
$W_{ m ecs}^*$	radial velocity in the ECS relative to the solid phase motion	J
$U_{ m ecs}^*$	radial velocity in the ECS relative to the solid phase motion	

Since the deformation of the endfeet is only in the r direction and the venule site is a free surface, if we also assume negligible displacement in the z direction,

we obtain the analytical solution

$$\mathbf{d}_{\text{ecs}}(r, z, t) = [d(z, t)(\frac{r_1 + b}{r}), 0]. \tag{A.25}$$

To put the equations in dimensionless form, we use the scalings

$$r_{\rm ecs} = b_{\rm ecs} R_{\rm ecs}, \ u_{\rm ecs}^* = b_{\rm ecs} f U_{\rm ecs}^*, \ w_{\rm ecs}^* = l f W_{\rm ecs}^*, \ p_{\rm ecs} = \frac{\mu f}{\varepsilon^2} P_{\rm ecs},$$
 (A.26)

The equations in dimensionless form are then

$$U_{\rm ecs}^* = -K_{\rm recs} \frac{\partial P_{\rm ecs}}{\partial R_{\rm ecs}},\tag{A.27}$$

$$W_{\rm ecs}^* = -K_{\rm zecs} \frac{\partial P_{\rm ecs}}{\partial Z},\tag{A.28}$$

$$K_{\text{recs}}\left(\frac{1}{R}\frac{\partial P_{\text{ecs}}}{\partial R} + \frac{\partial^2 P_{\text{ecs}}}{\partial R_{\text{ecs}}^2}\right) + \frac{b_{\text{ecs}}}{l_0}K_{\text{zecs}}\frac{\partial^2 P_{\text{ecs}}}{\partial Z^2} = 0,$$
(A.29)

where $K_{recs} = k_{ecs}(b_{ecs}^2 \varepsilon^2)^{-1}$ and $K_{zecs} = k_{ecs}(l_0^2 \varepsilon^2)^{-1}$, and the boundary conditions in dimensionless form are

$$R_{\text{ecs}} = \frac{r_1 + b}{b_{\text{ecs}}} : \ U_{\text{ecs}}^* = \frac{b}{b_{\text{ecs}}} U^*,$$
 (A.30)

$$R_{\rm ecs} = \frac{r_1 + b + b_{\rm ecs}}{b_{\rm ecs}}$$
: $P_{\rm ecs} = 0$, (A.31)

$$Z = 0$$
 and $Z = 1$: $\frac{\partial P_{\text{ecs}}}{\partial Z} = 0$. (A.32)

The flow in the ECS domain is computed using a custom-developed Poisson equation solver.

The lumped-parameter model

Lumped parameters

We further simplify our model in terms of lumped parameters. All coefficients in equation 4.6 can be identified from the coefficients in the fluid dynamical equation A.10, neglecting some higher-order infinitesimal terms. Here, we present

another way to derive the coefficients through direct analysis of the pressure-flowrate lumped-parameter model (equation 4.6).

Fluid motion induced by the prescribed arterial pulsation is modeled as a flow rate source (analogous to the current source in figure 4.4a) with a volume flow rate equal to the rate of change of the artery volume, described by equation 4.4.

There are three pathways by which fluid can enter or exit the penetrating PVS, as sketched in figure 4.4a. Fluid can be exchanged with the pial PVS or the extracellular space, via the endfoot wall. Due to high resistance, flow through the capillary PVS is negligible. Each pathway has a hydraulic resistance, and ultimately connects to a place where the pressure(analogous to voltage) is zero. By calculation, the resistance of the pial pathway is $R_{pial} = k_{pial}^{-1} = 1.06 \times 10^{16} \text{ kg m}^{-4} \text{ s}^{-1}$.

Though the resistance of the endfoot wall and that of the extracellular space depend on the surface area change of the endfoot wall (due to the deformation), they are small terms and we neglect them here for simplicity. Therefore, the resistance of the endfoot wall is inversely proportional to its area and its area-normalized permeability k_{endft} , which is pressure-dependent:

$$R_{\text{endft}} = \frac{1}{2\pi l(r_1 + b)k_{\text{endft}}} = \begin{cases} 4.0 \times 10^{16} \text{ kg m}^{-4} \text{ s}^{-1} & p > p_{\text{ecs}} \\ 8.0 \times 10^{16} \text{ kg m}^{-4} \text{ s}^{-1} & p \le p_{\text{ecs}}, \end{cases}$$
(A.33)

for $k_1/k_0 = 2$. We only consider the resistance of the extracellular space $R_{\rm ecs}$ in the radial direction, which is

$$R_{\text{ecs}} = \frac{\mu}{2\pi l k_{\text{ecs}}} \ln \frac{r_1 + b + b_{\text{ecs}}}{r_1 + b} = 2.56 \times 10^{15} \text{ kg m}^{-4} \text{ s}^{-1}$$
 (A.34)

for $k_{\text{ecs}} = 10^{-16} \text{ m}^2$. The logarithmic term in equation A.34 is derived from equation A.21 in the annular ECS domain Schreder et al. 2022; Holter et al. 2017.

The deformation of the endfoot wall can be modeled as the capacitance in the circuit, described by equation 4.5, with a value $C_{\rm endft} = (2.51 \times 10^{-12} \times E_{\rm endft}^{-1}) \, {\rm m}^3 s \, {\rm kg}^{-1}$, inversely proportional to $E_{\rm endft}$.

Time dependent solution of the lumped-parameter model in the absence of the valve

In complex domian equation 4.4 can be written as:

$$\tilde{q}_{\rm art} \approx 2\pi r_1 l h_{\rm cp} 2\pi f e^{2\pi i f t},$$
 (A.35)

In the absence of the valve, equation 4.6 can be rewritten as:

$$2\pi r_1 lh_{\rm cp} 2\pi f e^{2\pi i f t + \frac{t}{R_{\rm eff}C_{\rm endft}}} = C_{\rm endft} \frac{\partial (p e^{\frac{t}{R_{\rm eff}C_{\rm endft}}})}{\partial t}, \tag{A.36}$$

where $R_{\text{eff}}^{-1} = (R_{\text{endft}} + R_{\text{ecs}})^{-1} + R_{\text{pial}}^{-1}$. Integrating equation A.36 over time, we have:

$$\frac{2\pi r_1 lh_{\rm cp} 2\pi f}{2\pi f i + \frac{1}{R_{\rm eff} C_{\rm endft}}} e^{2\pi i f t + \frac{t}{R_{\rm eff} C_{\rm endft}}} = C_{\rm endft} p e^{\frac{t}{R_{\rm eff} C_{\rm endft}}}. \tag{A.37}$$

Therefore, we have the analytical solution for the pressure:

$$p = \frac{4\pi^2 r_1 l h_{\rm cp} f}{C_{\rm endft} (2\pi f i + \frac{1}{R_{\rm eff} C_{\rm endft}})} e^{2\pi i f t} = \frac{4\pi^2 r_1 l \bar{h}_{\rm cp} f e^{2\pi i (f t - \frac{\arctan(2\pi f R_{\rm eff} C_{\rm endft})}{2\pi})}}{C_{\rm endft} \sqrt{4\pi^2 f^2 + (\frac{1}{R_{\rm eff} C_{\rm endft}})^2}}, \quad (A.38)$$

From equation A.38 we can derive equation 4.7, given that $p = -R_{\text{pial}}q_{\text{pial}}$.

B. Impedance pumping models

The section includes mathematical details of the impedance pumping models in Chapter 5. It has been published in Holstein-Rønsbo et al. 2023

Flows driven by arterial diameter changes were modeled via IB2D, an open-source, 2D immersed boundary method code for fluid simulation (Battista, Baird, and Miller 2015; Battista, Strickland, and Miller 2017). Approximating arterial diameter changes and flow to be axially symmetric, we modeled an axial plane of the artery and PVS. In a 5×5 nondimensional computational domain with periodic boundary conditions, we modeled each tissue (upper and lower artery wall, upper and lower PVS boundary) as a single layer of solid nodes spanning $1 \le x \le 4$, where x is the axial coordinate and x=0 at the left end of the domain. In dimensionless units, the diameter of the artery was 2 and the diameter of the PVS was 3.1, such that the ratio of their cross-sectional areas was 1:1.4 as measured in vivo (Mestre, J. Tithof, et al. 2018). We defined the artery walls as deformable tissues with spring stiffness $k = 5 \times 10^5$ and beam stiffness $k_b = 1 \times 10^7$. The upper and bottom artery walls were linked with spring stiffness $k_{s1} = k_s/100$ to account for their connection in three dimensions. The left and right ends of the artery walls were fixed in place, as were the entire PVS outer boundaries.

The grid size of the CSF fluid was 64×64 , and that of the solid tissues was 128×1 . The time step of the simulation was $dt = 5 \times 10^{-4}$. We drove arterial diameter changes by applying a uniform force over the region $1.39 \le x \le 2.17$, which varied over time.

$$F = \begin{cases} 2k_{s1}\Delta D \sin^2 \frac{2\pi}{4(t_2 - t_1)} (t - t_1), t_1 \le t < t_2 \\ 2k_{s1}\Delta D, t_2 \le t < t_3 \\ 2k_{s1}\Delta D (1 - \sin^2 \frac{2\pi}{4(t_4 - t_3)} (t - t_3)), t_3 \le t < t_4 \end{cases}$$
(B.1)

Otherwise, F=0. Here t is time, $\Delta D = 0.05$ for dilation and -0.05 for constriction, $t_1 = 0.025$, $t_2 = 0.03125$, $t_3 = 0.04375$ and $t_4 = 0.05$. The motion of

the artery walls and the CSF were calculated based on the applied force, the elastic forces of tissues and the interactive forces between tissues and fluids. The normalized force F/k_{s1} is plotted in red in figure 5.5d,j.

We calculated the 2D volume flow rate through a cross-section of the PVS via numerical integration as $Q=\int_{\Gamma}U(r)\,\mathrm{d} r$, where U is the axial velocity, Γ is the cross-section and r is the radial coordinate. We calculated the normalized net mass flux of CSF as $\int_{\tau}Q\,\mathrm{d} t$. We also simulated tracers in the PVS, which move exactly as fluid elements, to visualize the Lagrangian movement of the CSF.